Dissertation

submitted to the

Combined Faculties for the Natural Sciences and for Mathematics

of the Ruperto-Carola University of Heidelberg, Germany

for the degree of

Doctor of Natural Sciences

presented by

Diplom-Phys.: Hnatic Slavomir

born in: Sankt Petersburg, Russia

Oral examination: 2 May 2007

Very High Energy Radiation From Binary System PSR B1259-63/SS 2883

Referees:	Prof. Dr.	Stefan Wagner
	Prof. Dr.	Matthias Bartelmann

Abstract

The inverse Compton (IC) scattering of ultrarelativistic electrons accelerated at the pulsar wind termination shock is believed to be responsible for TeV gamma-ray signal reported from the binary system PSR B1259-63/SS2883. While this process can explain the energy spectrum of the observed TeV emission, the gamma-ray fluxes detected by HESS at different epochs do not agree with the published theoretical predictions of the TeV lightcurve. In this work, evolution of the energy spectra of relativistic electrons under different assumptions about the acceleration and energy-loss rates of electrons, is studied. Consequently, it is demonstrated that the observed TeV lightcurve can be explained (i) by adiabatic losses which dominate over the entire trajectory of the pulsar with a significant increase towards the periastron, or (ii) by sub-TeV cutoffs in the energy spectra of electrons due to the enhanced rate of Compton losses close to the periastron. The calculated spectral and temporal characteristics of the TeV radiation provide conclusive tests to distinguish between these two working hypotheses.

The Compton deceleration of the electron-positron pulsar wind contributes to the decrease of the nonthermal power released in the accelerated electrons after the wind termination, and thus to the reduction of the IC and synchrotron components of radiation near the periastron. Although this effect alone cannot explain the observed TeV and X-ray lightcurves, the Comptonization of the cold ultrarelativistic wind leads to the formation of gamma-radiation with a line-type energy spectrum. While the HESS data already constrain the Lorentz factor of the wind, $\Gamma \leq 10^6$, future observations of this object with GLAST should allow a deep probe of the wind Lorentz factor in the range between 10^4 and 10^6.

Kurzfassung

Es wird angenommen, dass die inverse Compton Streuung von ultra-relativistischen Elektronen, die durch den Pulsar Wind Termination Shock beschleunigt werden, verantwortlich ist für das TEV Gamma-Strahlungs Signal, dass von dem binären System PSR B1259-63/SS2883 berichtet wurde. Obwohl dieser Prozess das Energiespektrum der beobachteten TeV Emission erklärt, stimmen die von HESS in anderen Zeiträumen gemessenen Gamma-Strahlen-Flüsse nicht mit den veröffentlichten, theoretisch berechneten, Vorhersagen für die TeV Lichtkurve überein. In dieser Arbeit werden die Veränderungen untersucht, welche die Energie-Spektren der relativistischen Elektronen, bei verschiedenen Annahmen zu der Beschleunigung und dem Energie-Verlust der Elektronen, durchlaufen. Mithin wird gezeigt, dass die beobachtete TeV Lichtkurve erklärt werden kann, (i) durch auf der gesamten Umlaufbahn des Pulsars dominierende adiabatische Verluste, mit einem signifikanten Anstieg nahe des Periastron, oder (ii) durch sub-TeV Cutoffs im Energie-Spektrum der Elektronen, verursacht durch verstärkte Compton-Verluste nahe am Periastron. Die berechneten spektralen und zeitlichen Charakteristiken der TeV Strahlung liefern überzeugende Tests, um zwischen diesen beiden Arbeitshypothesen zu unterscheiden.

Die Compton-Abbremsung des pulsaren Elektron-Positron Windes trägt zu der Abnahme der, von den beschleunigten Elektronen, nach der Wind Termination, abgegebenen, nicht-thermischen Leistung bei, und damit auch zu der Abnahme der IC und Synchrotron Komponenten der Strahlung nahe am Periastron. Obwohl dieser Effekt allein nicht die beobachteten TeV und Röntgen Lichtkurven erklären kann, führt die Comptonisierung des kalten ultra-relativistischen Windes zu einer Bildung von Gamma-Strahlung mit einem linien-artigen Energie-Spektrum. Während die HESS Daten den Lorentz-Faktor des Windes auf $\Gamma \leq 10^6$ beschränken, sollten zukünftige Beobachtungen dieses Objekts mit GLAST genauere Überpruefungen des Lorentz-Faktors, im Bereich zwischen 10^4 und 10^6, erlauben.

Contents

Chapter 1

Introduction

A large fraction of stars in our Galaxy exist in the form of binary systems, i.e. systems consisting of two stars orbiting around their center of mass. The sub-class of binaries, which contain a pulsar and a normal optical star, is called binary pulsars. About a hundred of such objects are found in our Galaxy.

Binary pulsar PSR B1259-63 was initially discovered in the radio survey of Galactic plane in 1992 (Johnston et al., 1992). PSR B1259-63/SS 2883 is a unique system with a pulsar orbiting in a highly eccentric orbit around a massive and very bright Be star SS 2883. In 2004 this system became the first detected galactic source of variable TeV emission (Aharonian et al., 2005).

The particles generating the very high energy (VHE) emission are believed to come from the pulsar magnetosphere. Generally, due to observed decrease in their rotation velocity, the lost energy of pulsars is believed to result in formation of an ultrarelativistic cold electron-positron[1] wind. This wind in principle can produce VHE photons via its interaction with the external medium, which in the case of PSR B1259-63 comes from the companion star SS 2883, characterized by an anisotropic mass outflow centered in its equatorial plane. The interaction of the pulsar wind and stellar outflow results in a standing shock, which is believed to thermalize pulsar electrons and accellerate them to TeV energies.

In such a scenario several mechanisms can be responsible for the production of VHE emission, such as hadronic interactions and bremsstrahlung in the stellar wind, or Inverse Compton (IC) scattering of pulsar electrons with the soft photon field of a Be star.

Although, due to lack of data from companion SS 2883, the hadronic models are not excluded (Kawachi et al., 2004), IC scattering appears to be the most plausible γ-ray production mechanism. Kirk et al. (1999) were able to explain absolute fluxes and energy spectra in the framework of the IC model, however the observed TeV lightcurve is significantly different from early predictions.

In the proposed model, the formed standing shock divides the interaction region into two zones with significantly different electron distributions, which produce VHE photons via interaction with starlight. While the assumption about the electron spectrum in the pre-shock region is rather trivial, the case of the formed post-shock spectrum is more complicated. In the latter, the shape of the electron spectrum differs for the different mechanisms dominant in its formation. Generally, electron energy losses (related to radiation processes, adiabatic cooling and particle escape) affect the shape of the formed spectrum, and the maximum energy of the electrons results from a competition between the acceleration and energy loss mechanisms. Since the magnetic field, photon density, adiabatic cooling rate and other parameters of the binary vary along the orbit, in principle, when coupled with reasonable

---

[1] in the following by "pulsar electrons" or "electrons" we will mean positrons as well.

physical assumptions, this variation is key to explaining the detected variable emission.
The main aim of this work is, for the first time, to analyze *all* the aforementioned effects in detail and consequently propose possible physical processes able to explain the detected TeV lightcurve.

We will start with a brief introduction into the subject of pulsars and Be-stars relevant for this work, namely the structure of their winds. At the end of this chapter, we will summarize observations of PSR B1259-63/SS 2883 as well as the results obtained by other authors following different models.

1.1 Binary pulsars

Pulsars

are rapidly spinning *neutron* stars whose environments produce conal beams of radiation which are detected on Earth in the form of periodic pulsation.
Neutron stars are formed in type *Ib* or *II* supernova explosions[2] when massive stars ($M \geq 10 M_\odot$) run out of their nuclear fuel. When the iron core of the star exceeds its Chandrasekhar mass ($\sim 1.5 M_\odot$), the core undergoes gravitational collapse in seconds. A Neutron star is then formed from the core and the outer layers of the star are completely disrupted and followed by release of gravitational and kinetic energy. Only 1% of the energy can be seen as a brilliant burst, the supernova. Due to large shrinkage of the star radius the formed star starts to spin rapidly (angular momentum conservation).
Such a rotating magnetized star produces a so-called magnetosphere shown in Fig.1.1.

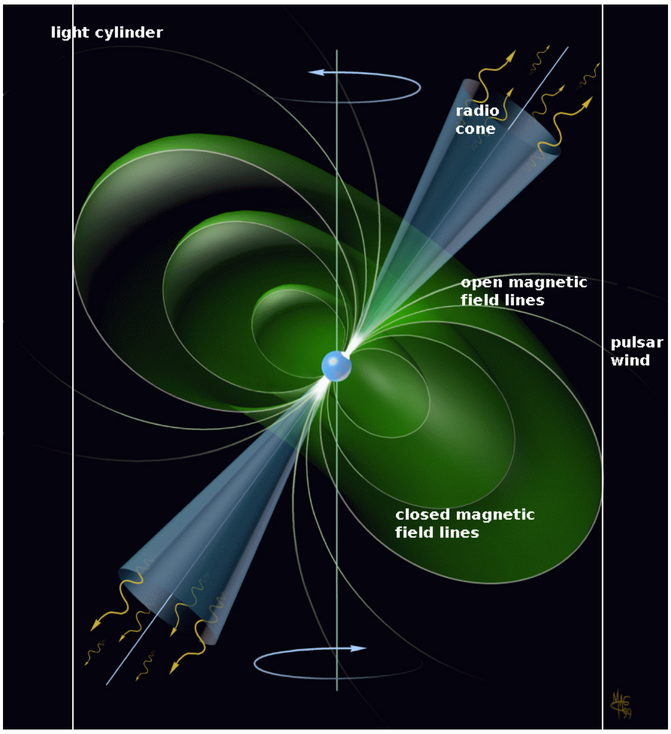

FIGURE 1.1: Pulsar magnetosphere. © Mark A. Garlick/space-art.co.uk.

---

[2] Type *I* supernovae show no detectable hydrogen in its spectra and additionally type *Ib* show evidence of helium present, type *II* supernovae show standard level of abundance in ejected material including hydrogen.

The rotating magnetic field induces a strong electric field which accelerates charged particles from the region close to the star into the ionized magnetosphere. The conductivity is high along magnetic field lines and very low perpendicular to the field lines, since the perpendicular component of the particle momentum is irradiated quickly through synchrotron radiation due to the presence of the strong magnetic field. This forces charged particles to corotate with the pulsar. At a radial distance $r_{\mathrm{c}} = c/\Omega$ a particle would travel at the speed of light, therefore corotation must break within the "light cylinder" (Fig.1.1). After crossing the light cylinder, the particles flow outwards and form the so-called pulsar wind.

In this work we will follow the results of the theoretical analysis of the Crab Nebula pulsar by Rees & Gunn (1974) and Kennel & Coroniti (1984a). According to their model the pulsars create a electron-positron pair plasma along the open current-carrying magnetic field lines connecting the polar caps of a magnetized neutron star to its exterior magnetosphere. Where in the magnetosphere and how many pairs are created is not clear. Far behind the light cylinder the created plasma forms ultrarelativistic wind with a Lorentz factor $\Gamma \sim 10^4 - 10^6$ where more than 99% of the pulsar spin-down power is converted into the kinetic energy of the wind. The interaction of the formed wind with the surrounding medium leads to the formation of a relativistic standing shock.
The structure of the pulsar wind and its electromagnetic field is still an unsolved problem in plasma physics. The asymptotic spatial dependance of the magnetic field at large distances is known from Bogovalov (1999), who obtained a self-consistent MHD (magnetohydrodynamic) solution for the case of the wind generated by a oblique rotator. The value of the light cylinder radius of PSR B1259-63 is $r_{\mathrm{lc}} = 6.25 \cdot 10^{11}$ cm and we will see in chapter 3 that the shock is formed at larger distances[3] - consequently we will use conclusions from (Bogovalov, 1999) in our treatment.

In the aforementioned paper, the pulsar was approximated to have a split monopole magnetic field (Fig.1.2) misaligned with the rotation axis. The structure of the obtained field lines is shown in Fig.1.3 implying the collimated outflow along the rotation axis. The obtained asymptotic solution implies radial outflow of plasma and magnetic field dependancies[4]

$$\vec{B}_p \sim \frac{1}{r^2},$$
$$B_\phi = -\left(\frac{r\Omega\sin\theta}{c}\right)|\vec{B}_p| \sim \frac{\sin\theta}{r} \qquad (1.1)$$

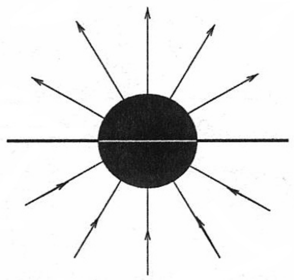

FIGURE 1.2: Split monopole field.

where $\vec{B}_p$ is the magnetic field in the poloidal plane and B_ϕ is the toroidal component. Therefore at sufficiently large distances, except near the rotation axis, the magnetic field is dominated by its toroidal component.

---

[3] This question was adressed in work of Tavani & Arons (1997) who found that for parameters characterizing PSR B1259-63/SS 2883 it is very unlikely for shock to be formed at distances closer than r_{lc}

[4] The formula holds for the relativistic wind outflow. For nonrelativistic outflows c has to be replaced by speed of the wind.

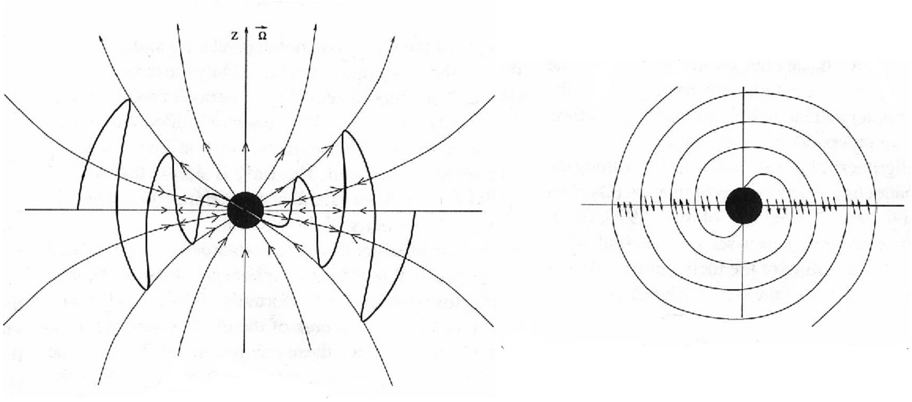

FIGURE 1.3: Left panel shows the structure of field lines and the current sheet (thick wave-like line) in the poloidal plane. Right panel shows structure of field lines in the equatorial plane. The arrows show the direction of the magnetic field lines. The direction of the field changes on current sheet. The figure is taken from (Bogovalov, 1999).

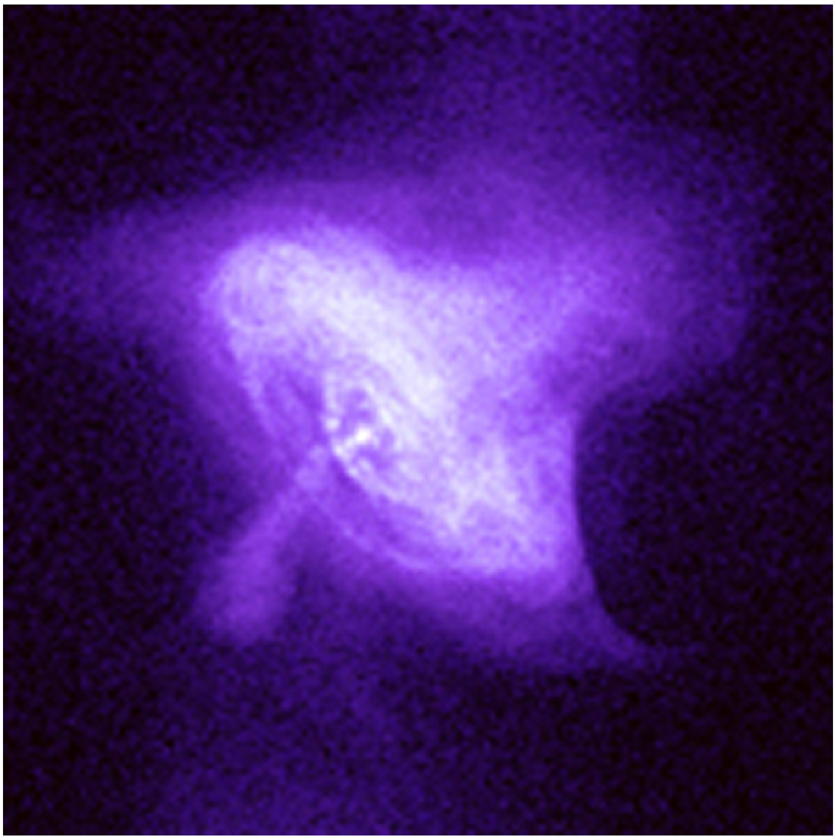

FIGURE 1.4: Crab Nebula in X-ray band. Image taken by Chandra observatory.

This introduction into the subject of pulsars provides a sufficient basis for this work. The interested reader can find a review of pulsar physics, for example, in the classical paper of Michel (1982).

1.2 Be stars

Be stars

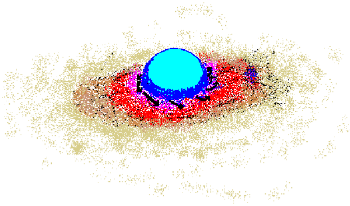

are non-supergiant B-type stars with typical parameters:

- temperature range $10^4 - 3 \cdot 10^4\,\mathrm{K}$
- mass scale $\sim 10\,M_\odot$
- radius scale $\sim 10\,R_\odot$

Their spectrum is characterized by one or more Balmer ($n = 2$ transitions) lines produced in circumstellar material around the equator. This material is believed to be ejected from the star due to its rapid rotation and the extent of the disc is inferred from observations to be at least 20 stellar radii.

The structure of the disc is deduced from observations in the ultraviolet and infrared regions of the electromagnetic spectrum.

In the **IR region** radiation excess is observed, which is interpreted as being due to the presence of large amount of circumstellar material (free-free emissivity goes as the square of the material density). The model used to interpret this excess consists of the high-density disc in the equatorial plane of the star with the opening angle $2\theta'$ and the density distribution

$$\rho_{\mathrm{eq}}(R) = \rho_{0,\mathrm{eq}} \left(\frac{R}{R_*}\right)^{-n}, \tag{1.2}$$

where $\rho_{0,\mathrm{eq}}$ is the density at the star surface, and R_* is the star radius. The derived densities $\rho_{0,\mathrm{eq}}$ are of the order of $10^{-10} - 10^{-12}\,\mathrm{g\,cm^{-3}}$ (Waters, 1986; Waters et al., 1988).
A continuity equation gives for the mass outflow through the surface of a star

$$\dot{M}_{\mathrm{IR}} = \rho_{0,\mathrm{eq}} v_{0,\mathrm{eq}} 4\pi R_*^2 \sin\theta'. \tag{1.3}$$

This outflow is conserved, therefore from $\dot{M}_{\mathrm{IR}} = \rho_{\mathrm{eq}} v_{\mathrm{eq}} 4\pi R^2 \sin\theta'$ we obtain the outflow velocity at distance R

$$v_{\mathrm{eq}}(R) = v_{0,\mathrm{eq}} \left(\frac{R}{R_*}\right)^{n-2}, \tag{1.4}$$

where v_0 is believed to be $\sim 10\,\mathrm{km\,s^{-1}}$. Consequently, the dynamic outflow pressure at a distance R from the surface of the star is

$$P_{\mathrm{eq}}(R) = \rho_{\mathrm{eq}}(R) v_{\mathrm{eq}}(R)^2 = \rho_{0,eq} v_{0,\mathrm{eq}}^2 \left(\frac{R}{R_*}\right)^{n-4}. \tag{1.5}$$

The pressure must decrease with the distance, therefore we obtain a condition on the exponent $n < 4$. The outflow exponent derived from observed data varies in the range $2.1 \le n \le 3.5$ (Waters et al., 1988).

In the **UV region** P Cygni[5] line profiles are observed indicating mass loss of the wind due to the spherically symmetric expanding stellar envelope (Snow, 1981). The empirical velocity profile of the expansion derived from observations has the power-law form

$$v_{\mathrm{pol}}(R) = v_{0,\mathrm{pol}} + (v_\infty - v_{0,\mathrm{pol}}) \left(1 - \frac{R_*}{R}\right)^{\beta}, \tag{1.6}$$

---

[5] P Cygni profiles form from the expanding stellar material. As a consequence of Doppler effect the radiation from the material moving towards the observer gets shifted to higher frequencies and radiation from rest of the material gets shifted to lower frequencies. This results in assymetric emission-absorption profile.

with the expansion velocity $v_{\rm pol}(R)$ increasing monotonically outward and asymptotically approaching the terminal velocity v_∞ at large distances (Castor & Lamers, 1979). The velocity law with initial velocity $v_0 \simeq 0.01\,v_\infty$ and exponent $\beta \simeq 1$ is in agreement with observations of UV line profiles as found in Snow (1981). The values of the terminal velocity in polar regions are found from the UV line edges to be between 800 and 3440 $\rm km\,s^{-1}$ (Snow, 1981; Lamers et al., 1982). One has to keep in mind that these values are minimal due to observational limits - the low column density of the stellar envelope in regions far away from the star.

The corresponding dynamic outflow pressure of the polar wind is

$$P_{\rm pol}(R) = \rho_{\rm pol}(R) v_{\rm pol}(R)^2 \simeq \frac{\dot{M}_{\rm UV}}{4\pi R^2} v_{\rm pol}(R) = \frac{\dot{M}_{\rm UV}}{4\pi R^2} v_\infty \left(1 - 0.99\frac{R_*}{R}\right) \tag{1.7}$$

using $v_\infty = 100\,v_{0,\rm pol}$, and exponent $\beta = 1$. For the regions sufficiently far away from the star, the pressure can be approximated simply as

$$P_{\rm pol}(R) \simeq \frac{\dot{M}_{\rm UV}}{4\pi R^2} v_\infty \quad , \quad \frac{R}{R_*} > 10. \tag{1.8}$$

The UV mass loss rates are found to be between[6] $10^{-8} - 10^{-10} (M_\odot/{\rm yr})$ (Waters et al., 1988).

1.3 Binary pulsar PSR B1259-63/SS 2883: observational results

PSR B1259-63 was discovered in a large-scale high frequency survey of the Galactic plane (Johnston et al., 1992) orbiting around a massive, main sequence, Be star.

The pulsar moves in a strongly eccentric orbit with a period $\sim 3.4\,$yr.

The distance to the pulsar can be estimated from its dispersion measure[7] and a model of Galactic electron density. The model of Lyne et al. (1985) implies a distance of 2.3 kpc, and a more recent model by Taylor & Cordes (1993) gives a distance of 4.6 kpc. It is likely that the pulsar distance is overestimated due to the presence of spiral arm at a distance 1.5 kpc along the line of sight to the pulsar.

Since the optical measurements of the companion SS 2883 imply a distance of 600 pc to 1.6 kpc (Johnston et al., 1994), summarizing we will assume that the binary system is located at distance $\sim 1.5\,$kpc.

The pulsar has a short spin period of $\sim 48\,$ms and a period derivative of $2.28 \cdot 10^{-15}$ implying a characteristic age of 300 kyr from its spin-down by magnetic dipole radiation. The spindown luminosity is defined as the rotational energy loss of the pulsar

$$L_{\rm p} = \frac{dE_{\rm rot}}{dt} = -I\Omega\dot{\Omega} \tag{1.10}$$

with $I = 0.4\,M_{\rm p}R_{\rm p}$ the moment of inertia of the pulsar and Ω its angular frequency, giving the value $\dot{E}_{\rm rot} \simeq 8 \times 10^{35}\,{\rm erg\,s^{-1}}$.

---

[6] Mass loss rates are known to be variable over a long timescale. In our case Tavani & Arons (1997) showed that for SS 2883 the mass loss rate does not vary significantly within a single pulsar orbit.

[7] The dispersion measure is defined as $\mathcal{D} = \int_0^D n\,dl$ (integration is performed over line of sight) and is related to the

$$\frac{dt_{\rm p}}{d\omega} = -\frac{4\pi e^2}{c m_{\rm e} \omega^3}\mathcal{D} \tag{1.9}$$

with $t_{\rm p}(\omega)$ being the arrival time of the pulse with frequency ω. The distance from the system may be estimated from the galactic density profile n. .

Table 1: **Parameters of PSR B1259-63/SS 2883 (Kirk et al., 1999)**

Parameter	Value	Reference
Pulsar		
Period, P	47.76 ms	Johnston et al. (1992)
Period derivative, $\dot{P}$	2.276×10^{-15}	Johnston et al. (1994)
Spindown luminosity, L_{p}	$8 \times 10^{35}\,\mathrm{erg\,s^{-1}}$	Johnston et al. (1996)
Be star		
Effective temperature, T_{eff}	$2.28 \times 10^{4}\,\mathrm{K}$	Underhill & Doazan (1982)
Radius, R_*	$6R_\odot = 4.2 \times 10^{11}\,\mathrm{cm}$	Underhill & Doazan (1982)
Luminosity, L_*	$8.8 \times 10^{3} L_\odot = 3.3 \times 10^{37}\,\mathrm{erg\,s^{-1}}$	Underhill & Doazan (1982)
Mass, M_*	$10M_\odot = 2 \times 10^{34}\,\mathrm{g}$	Underhill & Doazan (1982)
System		
Orbital period, P_{b}	1236.77 days	Johnston et al. (1994)
Longitude of periastron, ω	138.68°	Johnston et al. (1994)
Inclination, i	35°	Johnston et al. (1996)
Eccentricity, e	0.87	Johnston et al. (1996)
Periastron distance, d_{per}	$9.6 \times 10^{12}\,\mathrm{cm}$	
Distance to the system, D	$\sim 1.5\,\mathrm{kpc}$	Johnston et al. (1994)

The companion star SS 2883 is of spectral type B2e (Westerlund & Garnier, 1989) and thus has a mass of $\simeq 10\,M_\odot$ and a radius of $\simeq 6\,R_\odot$.
The mass function links the masses of two components of the binary system with the observed parameters and is given by

$$f = \frac{(M_* \sin i)^3}{(M_{\mathrm{p}} + M_*)^2} = \frac{4\pi^2}{G} \frac{(a \sin i)^3}{P_{\mathrm{b}}^2}, \tag{1.11}$$

where M_{p}, M_* are the masses of the pulsar and star, respectively, i is the orbital inclination (see section 3.1), P_{b} is the orbital period and G is the gravitational constant. The value of the mass function obtained from observations is $1.53\,M_\odot$ (Johnston et al., 1994), which assuming a pulsar mass of $1.4\,M_\odot$ and a mass of star $10\,M_\odot$ gives[8] $i = 35°$.

Table 1 provides a summary of the observed parameters of binary taken from Kirk et al. (1999).

The passage of the pulsar crossing the disc was determined from the disappearance of the pulsed radio emission. Observations of various periastron passages found pulsar undetectable in the radio band from -20 to $+16$ days near periastron (Connors et al., 2002) - 2000 periastron passage, and recently from -20 to $+16$ days near periastron - 2004 periastron passage. Bogomazov (2005) analyzed pulsed radio data and obtained similar results - namely he found the position of the disc to be centered at -23 and $+13$ days around periastron. However, as long as the physics of the interaction of the pulsar winds with the stellar disk is not firmly established, alternative models are not excluded. For example, Chernyakova et al. (2006)

---

[8] The mass function can be also written in form $f = M_{\mathrm{p}} \sin^3 i/(1+q)^2$ with $q = M_{\mathrm{p}}/M_*$. Since q is small and mass of the pulsar is fairly well established, the derived value of i provides reasonable estimate.

noticed that the maxima of lightcurves of *nonpulsed* radio, X-ray and TeV gamma-ray are quite close to each other (see Fig.1.6), and proposed that the increase of the nonthermal energy release happens when the pulsar crosses the disk. If so, the gamma-ray emission could be a result of hadronic interactions (Kawachi et al., 2004; Chernyakova et al., 2006). This hypothesis implies, however, a different location of the disk compared to the one derived from the eclipse of the pulsed radio emission, and therefore requires an independent confirmation based on stronger evidence of correlation of radio, X-ray and TeV fluxes, as well as detailed study of the reasons of such correlation.

Keeping these results in mind we assume that the disc is centered at -19 and $+15$ days near periastron (a schematic drawing of the binary is shown in Fig.1.5).

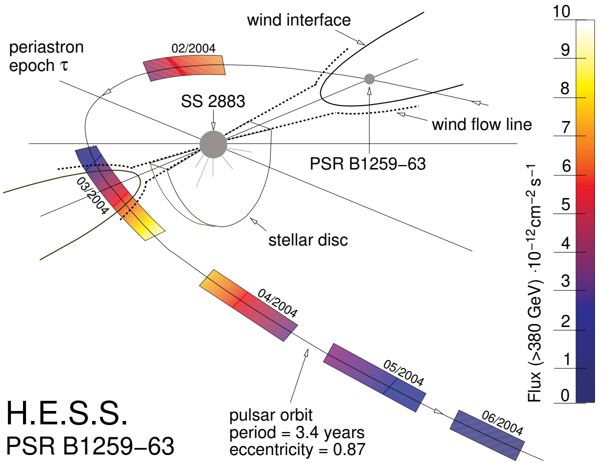

FIGURE 1.5: Binary system PSR B1259/SS 2883. The figure is taken from Aharonian et al. (2005).

Observations in the X-ray band performed by ASCA (1994), Beppo-SAX (1997) and XMM-Newton (2004) are summarized in Chernyakova et al. (2006). Their comparison with TeV and radio data is shown in Fig.1.6.

Tavani & Arons (1997) analyzed X-ray data and put some constraints on the possible mechanisms responsible for the emission. Namely, they excluded the accretion process (conversion of gravitational energy into radiation), the propeller effect (gas is gravitationally trapped before the light cylinder where it interacts with pulsar magnetosphere - magnetosphere rotates too fast to allow the accretion of the gas onto the pulsar) and bremsstrahlung emission caused by heated gas of the Be star outflow. Also, they explained X-ray data variability quite satisfactorily using a model of synchrotron radiation from pulsar wind electrons. Later, XMM-Newton observations in 2004 had shown quite a hard photon spectral index $\Gamma < 1.5$ for -40 to -20 days before periastron, implying spectra of electrons with power-law index $\alpha < 2$ and consequently the electron energy losses power law index smaller than one (4.5). Chernyakova et al. (2006) proposed that such a photon index can arise when there is a bremsstrahlung contribution from the shock-accelerated *stellar* wind electrons (usually proposed as a source of radio emission), however such an assumption results in the overestimation of pulsar spindown luminosity by two orders of magnitude. We will see in chapter 4.3 that the IC electron energy losses power law index in Klein-Nishina regime is ~ 0.3, thus in principle, the fluxes with photon spectral index < 1.5 can result from electron spectra formed in the scenario of dominant inverse-Compton (IC) losses mechanism.

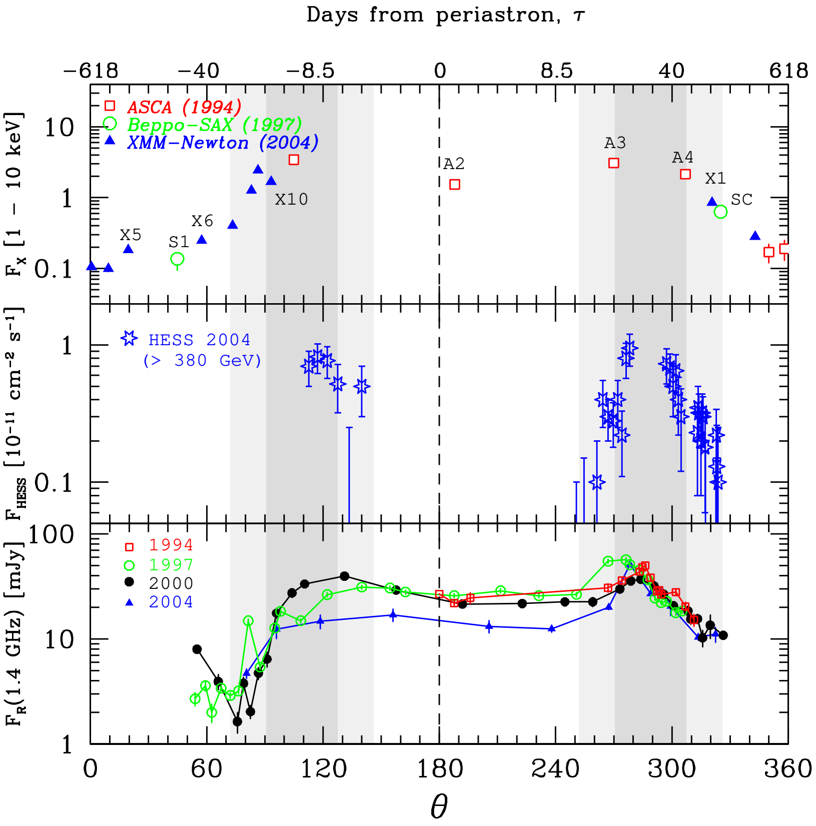

FIGURE 1.6: A comparison between the X-ray (top panel), TeV (middle panel) and radio (bottom panel) lightcurves of PSR B1259-63/SS 2883 taken from (Chernyakova et al., 2006). Grey parts represent the location of the disc as proposed by Chernyakova et al. (2006).

The gamma ray signal from PSR B1259-63 was detected by H.E.S.S. shortly before and up to 100 days after its 2004 periastron passage (Aharonian et al., 2005).
The measured, averaged (over the whole observation period), differential energy spectrum is shown in Fig.1.7. A power-law fit

$$F(E) = dN/dE = F_0 \left(\frac{E}{\text{TeV}}\right)^{-\Gamma} \tag{1.12}$$

of this spectrum gives a photon index $\Gamma = 2.7 \pm 0.2$ with $F_0 = (1.3 \pm 0.1) \times 10^{-12}$ cm^{-2}s^{-1}TeV^{-1}. The shapes and levels of spectra were explained quite well in Kirk et al. (1999), where authors considered the radiative losses, adiabatic losses of electrons respectively as the dominant mechanisms in the formation of the electron spectra.

The emission was found to be variable with maxima near the location of the disc. Unfortunately, due to the full moon and bad weather conditions, data during periastron are missing. Nevertheless, the TeV lightcurve shows a tendency of the emission decrease towards periastron, as also concluded by the H.E.S.S. collaboration in (Aharonian et al., 2005).

The detected lightcurve is presented in Fig.1.8 together with different proposed explanations:

- the solid line representing a misaligned disk model suggested by Kawachi et al. (2004) where the authors assumed electron bremsstrahlung and proton-proton emission processes to be dominant during the passage of the disc

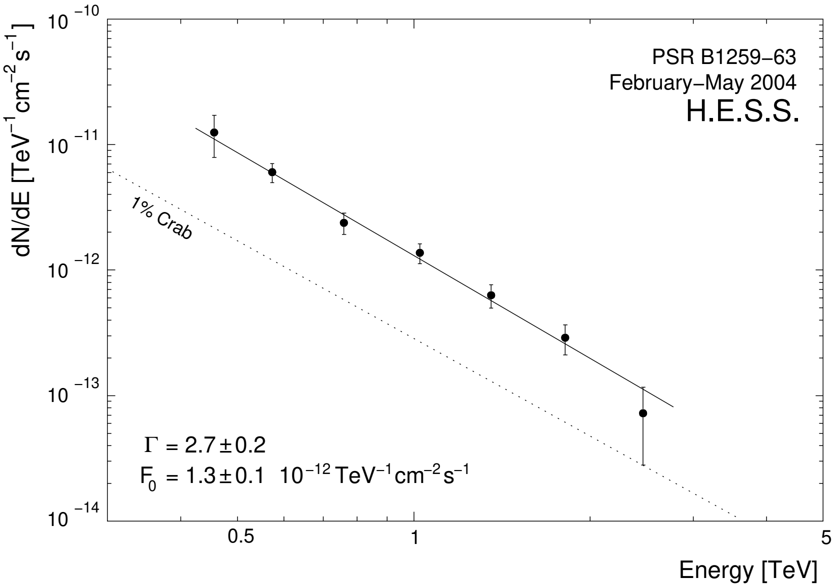

FIGURE 1.7: The differential energy spectrum dN/dE of γ-rays from PSR B1259-63/SS 2883 using HESS 2004 data from the periods with significant detection of the pulsar (February-May). The solid line shows the power-law fit to the spectrum. The figure is taken from Aharonian et al. (2005)

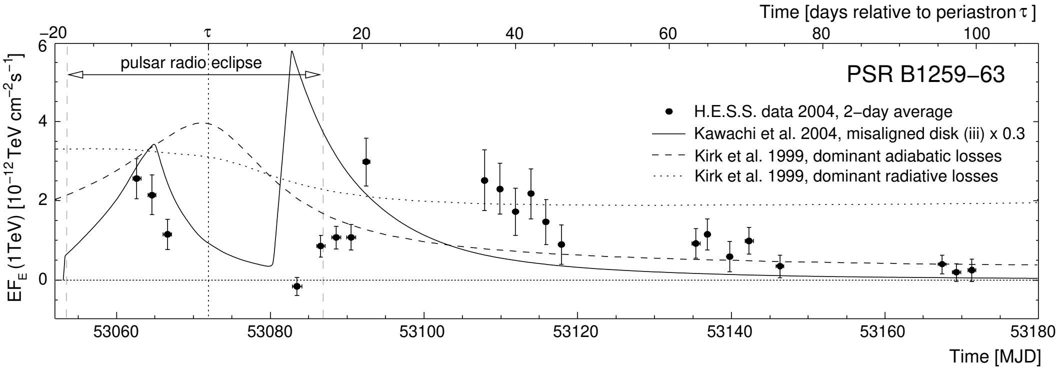

FIGURE 1.8: The γ-ray lightcurve detected by HESS in 2004 and proposed models. The figure is taken from Aharonian et al. (2005)

- the dashed line a model suggested by Kirk et al. (1999) with a dominant mechanism of adiabatic losses in the formation of the electron spectrum

- the dotted line a model from the same author with a dominant mechanism of radiative losses.

The apparent feature of the model scenarios is the assymetry of the predicted lightcurves around periastron. In shown models of Kirk et al. (1999) (Fig.1.8) assymetry arises from the angular dependance of the scattering cross-section. The target photons from the Be star form an almost mono-directional beam, and the scattering angle under which photons reach an observer is a function of the phase of the binary. In the model of Kawachi et al. (2004) the assymetry results from the hadronic interactions during the passage of the pulsar through the dense disc of the star.

An explanation of the 1 TeV lightcurve is the main goal of this work. We will thoroughly analyze the IC model and introduce new physical mechanisms which, as will be shown later, will be able to explain variability of TeV emission, and predict the lightcurves for other energy bands.

Chapter 2

Radiation processes

Knowledge of the features of radiation mechanisms forms an essential part in a determination of the underlying physical processes in the universe from observational data..

In this chapter we will review the most important processes related to the production of VHE γ-rays.

We will start with a detailed analysis of the Inverse Compton process and a brief overview of photon-photon absorption - the two processes essential in the production of the γ-ray emission in radiation dominated environments. Then we proceed with the synchrotron radiation and bremsstrahlung processes, in which magnetic fields and nuclei are present, respectively. After that, a short overview of the most important process of the generation of VHE emission by hadronic interactions, π^0-decay, will be presented.

The chapter will end with a summary of the electron energy losses formulae, essential for the correct calculations of the formed electron spectra.

2.1 Inverse Compton scattering

In Compton scattering, the photon gives energy to the electron, whereas in the Inverse Compton process, the high energy electron gives its energy to the soft photon (Fig.2.1).

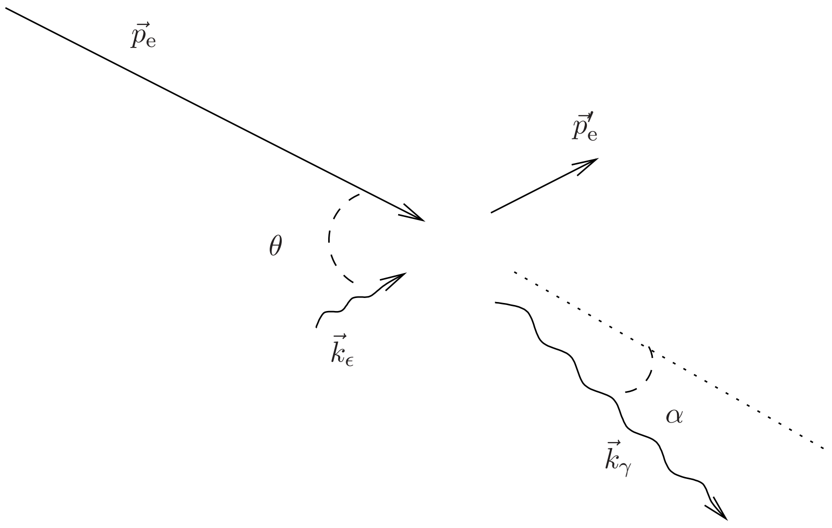

FIGURE 2.1: Inverse Compton scattering. α is the angle between total incoming momentum vector $\vec{p}_e + \vec{k}_\epsilon$ and outgoing photon momentum vector $\vec{k}_\gamma$.

To quantitatively analyze Inverse Compton scattering, for simplicity let us consider the monoenergetic beam of electrons with energy E_{e}, colliding with the monoenergetic beam of photons with energy ϵ. Since $p_{\mathrm{e}} = (E_{\mathrm{e}}/c, \vec{p}_{\mathrm{e}})$, $k_\epsilon = (\epsilon/c, \vec{k}_\epsilon)$ and $m_\epsilon = 0$ from (A.8) we have

$$\frac{c\sqrt{(p_{1i}p_2^i)^2 - (m_1 m_2 c^2)^2}}{\frac{E_1 E_2}{c^2}} = \frac{c(E_{\mathrm{e}}\epsilon - c|\vec{p}_{\mathrm{e}}|\epsilon\cos\theta)}{E_{\mathrm{e}}\epsilon} = c(1-\beta\cos\theta), \tag{2.1}$$

with $\beta = v/c$, v - the electron velocity , θ - the angle between the incoming photon and electron momentum vectors. For isotropic scattering, averaging of (2.1) gives c.
The double differential cross-section of the inverse Compton process for the scattering of the electron with energy γ and photon with energy ω under angle θ producing outgoing gamma-ray photon with energy E_γ is (Bogovalov & Aharonian, 2000)

$$\begin{aligned}\frac{d\sigma}{dE_\gamma d\Omega(\theta)}(\gamma,\omega,E_\gamma,\theta) &= \frac{\pi r_{\mathrm{e}}^2}{(pk)^2}\frac{\omega_{\mathrm{c}}}{\Gamma V_{\mathrm{c}}}\left\{\frac{1}{(pk)^2} - \frac{2I}{(pk)\gamma_{\mathrm{c}}\omega_{\mathrm{c}}} + \frac{I^3(1-U\delta\xi)}{(\gamma_{\mathrm{c}}\omega_{\mathrm{c}})^2}\right. \\ &\quad \left. 2\left[\frac{1}{(pk)} - \frac{I}{\gamma_{\mathrm{c}}\omega_{\mathrm{c}}}\right] + \left[\frac{(pk)I}{\gamma_{\mathrm{c}}\omega_{\mathrm{c}}} + \frac{\gamma_{\mathrm{c}}\omega_{\mathrm{c}}(1-U\delta\xi)}{(pk)}\right]\right\},\end{aligned} \tag{2.2}$$

where

$$\begin{aligned}(pk) &= \gamma\omega(1-\beta\cos\theta) & V_{\mathrm{c}} &= \frac{\sqrt{\omega^2 + (\gamma\beta)^2 + 2\gamma\beta\omega\cos\theta}}{(\gamma+\omega)} \\ \Gamma &= \frac{\gamma+\omega}{\sqrt{1+2(pk)}} & \omega_{\mathrm{c}} &= \frac{(pk)}{\sqrt{1+2(pk)}} \\ \gamma_{\mathrm{c}} &= \frac{1+(pk)}{\sqrt{1+2(pk)}} & U &= \frac{(pk)}{1+(pk)} \\ \delta &= \frac{E_\gamma}{V_{\mathrm{c}}\Gamma\omega_{\mathrm{c}}} & \xi &= \frac{1}{UV_{\mathrm{c}}}\left(\frac{\gamma}{\Gamma\gamma_{\mathrm{c}}-1}\right) \\ I &= [1-U^2-2U(1-U)\xi\delta + U^2(\delta-\xi)^2]^{-1/2}. & &\end{aligned}$$

The cross-section for the isotropic scattering is obtained by averaging over θ

$$\frac{d\sigma_{\mathrm{is}}}{dE_\gamma d\Omega} = \frac{1}{4\pi}\int_0^\pi \frac{d\sigma}{dE_\gamma d\Omega}(1-\beta\cos\theta)d\Omega \tag{2.3}$$

giving

$$\begin{aligned}\frac{d\sigma_{\mathrm{is}}}{dE_\gamma d\Omega}(\gamma,\omega,E_\gamma) &= \pi r_{\mathrm{e}}^2\frac{E_\gamma}{\gamma^3\omega^2(\gamma-E_\gamma)}\left[-\ln\left(4\frac{(\gamma-E_\gamma)\omega\gamma}{E_\gamma}\right) - \right. \\ &\quad \left. -\frac{1}{4}\frac{(E_\gamma + 4E_\gamma\omega\gamma - 4\omega\gamma^2)(E_\gamma^2\omega + E_\gamma - 2\gamma\omega E_\gamma + 2\omega\gamma^2)}{E_\gamma\gamma\omega(\gamma-E_\gamma)}\right]\end{aligned} \tag{2.4}$$

where in (2.2,2.3,2.4) all energies are in units of $m_{\mathrm{e}}c^2$.

Area definition of the both cross-sections must be calculated from the energy-momentum conservation laws. 4-momentum conservation is

$$p_{\mathrm{e}} + p_\epsilon - p_\gamma = p_{\mathrm{e}}' \tag{2.5}$$

its square giving

$$\begin{aligned} p_\mathrm{e} p_\epsilon &= (p_\mathrm{e} + p_\epsilon) p_\gamma, \\ \epsilon(E_\mathrm{e} - c|\vec{p}_\mathrm{e}|\cos\theta) &= E_\gamma(E_\mathrm{e} + \epsilon - c|\vec{p}_\mathrm{e} + \vec{k}_\epsilon|\cos\alpha), \end{aligned}$$

with α being the angle between the direction of the outgoing photon momentum vector and total incoming momentum vector $(\vec{p}_\mathrm{e} + \vec{k}_\epsilon)$. For the minimal outgoing photon energy we have $\cos\alpha = -1$

$$E_{\gamma,\mathrm{min}} = \frac{\epsilon(E_\mathrm{e} - c|\vec{p}_\mathrm{e}|\cos\theta)}{(E_\mathrm{e} + \epsilon + c|\vec{p}_\mathrm{e} + \vec{k}_\epsilon|)} \tag{2.6}$$

and for the maximum energy $\cos\alpha = 1$

$$E_{\gamma,\mathrm{max}} = \frac{\epsilon(E_\mathrm{e} - c|\vec{p}_\mathrm{e}|\cos\theta)}{(E_\mathrm{e} + \epsilon - c|\vec{p}_\mathrm{e} + \vec{k}_\epsilon|)}. \tag{2.7}$$

Aditionally, for isotropic scattering the condition for minimum energy of an outgoing photon is $\cos\theta = 1$ resulting in

$$E^\mathrm{is}_{\gamma,\mathrm{min}} = \frac{\epsilon(E_\mathrm{e} - c|\vec{p}_\mathrm{e}|)}{E_\mathrm{e} + c|\vec{p}_\mathrm{e}|} \tag{2.8}$$

and for maximum energy of outgoing photon $\cos\theta = -1$ resulting in

$$E^\mathrm{is}_{\gamma,\mathrm{max}} = \frac{\epsilon(E_\mathrm{e} + c|\vec{p}_\mathrm{e}|)}{E_\mathrm{e} - c|\vec{p}_\mathrm{e}|}. \tag{2.9}$$

In general, the formula for the cross-section for IC scattering, shown in Fig.2.1, depends not only on the incoming angle θ represented by the corresponding solid angle $d\Omega_\mathrm{in}(\theta)$, but also on the outgoing angle α (represented by the corresponding solid angle $d\Omega_\mathrm{out}(\alpha)$) between the total incoming momentum vector $\vec{p}_\mathrm{e} + \vec{k}_\epsilon$ and the momentum vector of the outgoing photon $\vec{k}_\gamma$. For electron lorentz factors $\gamma \gg 1$ and for soft incoming photons $|\vec{p}_\mathrm{e}| \gg |\vec{k}_\epsilon|$ we obtain

$$\cos\alpha \approx 1 - \frac{\epsilon}{E_\gamma}(1 - \cos\theta). \tag{2.10}$$

Since $\cos\alpha$ differs from 1 by a factor of ϵ/E_γ, which is extremely small, the outgoing photons are irradiated in the direction of the incoming electron. Therefore, under these conditions the integration of the cross-sections over outgoing solid angle $d\Omega_\mathrm{out}(\alpha)$ resulting in the formulae (2.2,2.4) is justified.

Before calculating the scattering rate of two colliding beams, let us recall basic characteristics of Inverse Compton scattering. The oridnary Compton scattering is usually described in the rest frame of the electron, where for the energy of a scattered photon

$$\epsilon'_1 = \frac{\epsilon'}{1 + \frac{\epsilon'}{mc^2}(1 - \cos\theta'_1)} \tag{2.11}$$

holds. There are two regimes of the scattering with distinct features:

- **Thomson regime** - $\epsilon' \ll mc^2$
  In the laboratory frame the condition for scattering in the Thomson regime is

$$b = 4\frac{E_\mathrm{e}\epsilon}{(mc^2)^2} \ll 1. \tag{2.12}$$

Using the transformation relations for a photon $\epsilon_1 = \gamma\epsilon'_1(1-\beta\cos\theta'_1)$ and $\epsilon' = \gamma\epsilon(1-\beta\cos\theta)$ we have for the maximum energy of a photon in lab frame

$$\epsilon'_{1,\max} \approx 2\gamma\epsilon'_{1,\max} \approx 4\gamma^2\epsilon. \tag{2.13}$$

Although in the Thomson regime the maximum energy of outgoing photon can be very large $\sim 4\gamma^2\epsilon$, it is still small compared to energy of an electron, therefore the electron loses its energy approximately continuously.

- **Klein-Nishina regime** - $\epsilon' \gg mc^2$
  In the laboratory frame the condition for Klein-Nishina scattering is

  $$b = 4\frac{E_e\epsilon}{(mc^2)^2} \gg 1. \tag{2.14}$$

  The scattered photon carries away a large fraction of the electron energy, therefore the electron does not lose its energy continuously. The condition for the continuous losses approximation is $\dot{\gamma}/\gamma \ll Nc\sigma$ with N being the density of the scatterers (i.e. the cooling time of the electron is larger than the time between scatterings). The applicability of using the continuous losses approximation for our work is discussed later in section 4.1.

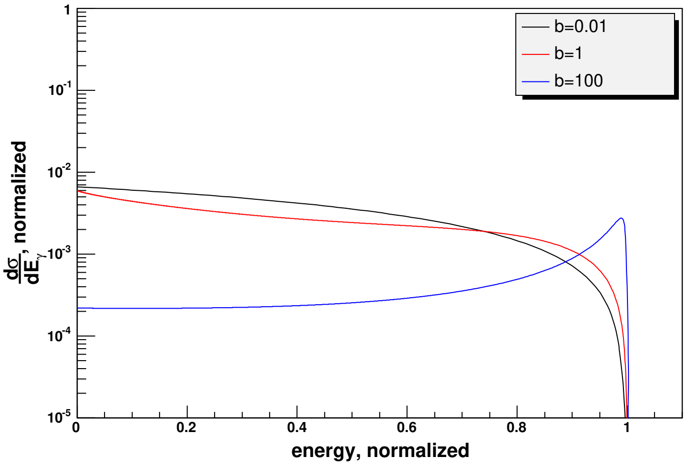

FIGURE 2.2: Isotropic inverse Compton scattering of two monoenergetic beams in the different regimes. The black line represents the scattering in Thomson regime ($b = 0.01$), red line the transition from Thomson to Klein-Nishina regime ($b = 1$) and blue line the scattering in Klein-Nishina regime ($b = 100$).

Returning to our problem, using δ-distributions for the incoming photon and electron beams, the scattering rate for an anisotropic case can be obtained combining (A.8), (2.1) and (2.2)

$$\frac{dN}{dtdE_\gamma}(E_\gamma,\theta) \propto (1-\beta\cos\theta)\frac{d\sigma}{dE_\gamma d\Omega(\theta)}(\gamma,\omega,E_\gamma,\theta), \tag{2.15}$$

similarly for the isotropic scattering

$$\frac{dN}{dtdE_\gamma}(E_\gamma) \propto \frac{d\sigma_{is}}{dE_\gamma d\Omega}(\gamma,\omega,E_\gamma), \tag{2.16}$$

where in both cases the proportionality constants are equal.
In Fig.2.2 the normalized spectra of isotropic inverse Compton scattering of two monoenergetic beams are shown. One sees that in Thomson regime $b \ll 1$ most of the scatterings

occur at low energies and in Klein-Nishina regime $b \gg 1$ most scatterings occur at high energies - energy of the outgoing photons is comparable to energy of the incoming high-energy electrons. Note that in figure 2.4 the cross-section is normalized, therefore one cannot see its decrease in Klein-Nishina regime, which can be seen by comparing Fig.2.3 with Fig.2.4.

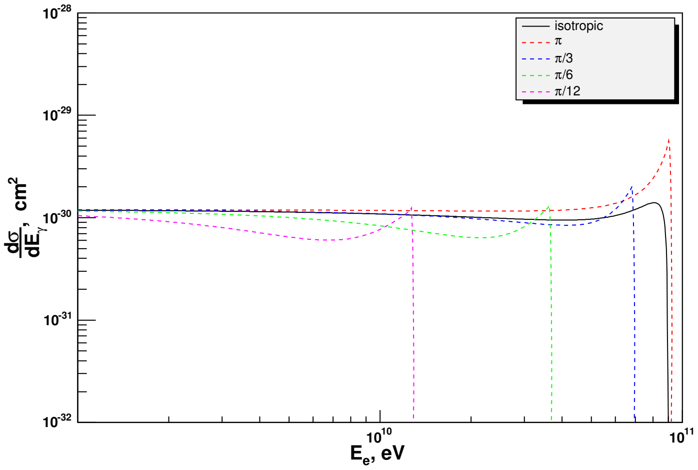

FIGURE 2.3: A comparison of isotropic and anisotropic inverse Compton scattering for $b \approx 10$.

The anisotropy effect is demonstrated in Fig.2.3 where we see that even for high values of the parameter b the anisotropy can significantly influence the resulting spectrum by shifting it to lower energies, i.e. the Klein-Nishina effect under small scattering angles is significantly reduced.

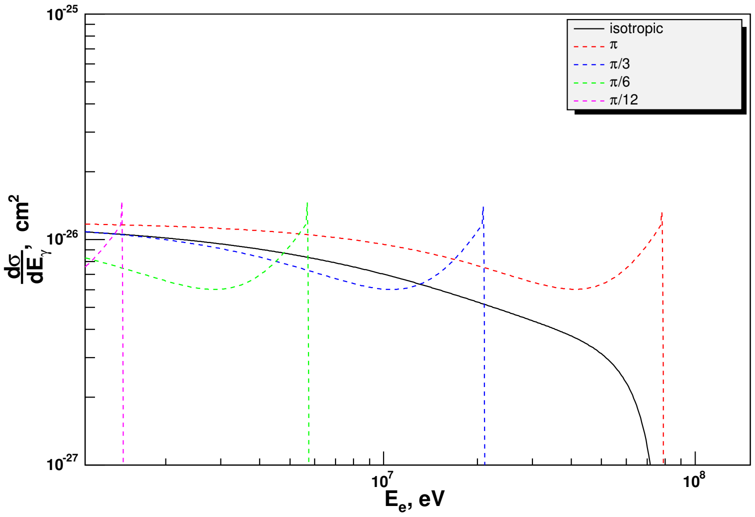

FIGURE 2.4: A comparison of isotropic and anisotropic inverse compton scattering for $b \approx 0.1$.

Finally, in the investigated binary PSR 1259-63/SS 2883, the effective temperature of the companion star is $T = 2.28 \cdot 10^4\,\mathrm{K}$ with the photon density peaking at energy $\sim 5\,\mathrm{eV}$, which for the later assumed accelerated electron spectrum in the range $1\,\mathrm{GeV} - 10\,\mathrm{TeV}$ gives the range of the parameter $b \approx 0.1 - 1000$, i.e. it includes the transition from Thomson into deep

Klein-Nishina regime, therefore for the broadband spectrum calculation the exact inverse Compton cross-section *must* be used to include both (Thomson and Klein-Nishina) effects. Moreover, as demonstrated in Fig.2.3 for the certain scattering angles even at high electron energies[1] the scattering can proceed in Thomson regime, therefore spectrum calculation using an approximation of the Klein-Nishina cross-section under such a circumstances leads to incorrect results as recently shown in (Khangulyan & Aharonian, 2005).

2.2 Photon-photon pair production

Another process determining the basic features of the interactions of electrons and γ-rays in the radiation dominated environments is photon-photon pair production (also called photon-photon absorption) - the inverse process to pair annihilation.
Due to electron and positron having non-zero mass, this process has a kinematic threshold

$$E_\gamma \epsilon (1-\cos\theta) \geq 2 \tag{2.17}$$

where E_γ, ϵ are the energies of photons (in $m_\mathrm{e}c^2$ units) colliding at an angle θ in the laboratory frame.
The parameter characterizing the absorption for the γ-ray moving through a photon gas with a spectral distribution $n_\mathrm{ph}(\epsilon, r)$ in a source of size R is the optical depth defined as

$$\tau(E_\gamma) = \int\limits_0^R dr \int\limits_{2/E_\gamma(1-\cos\theta)}^{\infty} d\epsilon\, n(\epsilon, r)\sigma(E_\gamma, \epsilon, \theta)(1-\cos\theta). \tag{2.18}$$

The detected flux can be obtained by multipliplying the primary flux by a factor $e^{-\tau}$.
The cross section of pair production is well known (see e.g. Berestetskii et al. 1974)

$$\sigma(\beta) = \frac{\pi r_e^2}{2}(1-\beta^2)\left[(3-\beta^4)\ln\frac{1+\beta}{1-\beta} - 2\beta(2-\beta^2)\right], \tag{2.19}$$

where β is the speed of the created electrons in CM (center of momentum) frame in c units. To express this cross-section in the variables $E_\gamma, \epsilon, \theta$ we use the invariant $k_\gamma k_\epsilon$. Since the energies of photons and created electrons in CM frame are equal, this invariant is $2\epsilon^2 = 2/(1-\beta^2)$. In the laboratory frame we have $k_\gamma k_\epsilon = E_\gamma \epsilon (1-\cos\theta)$. Therefore we obtain

$$\beta = \sqrt{1 - \frac{2}{E_\gamma \epsilon (1-\cos\theta)}}. \tag{2.20}$$

The cross-section is an invariant by definition and hence in the laboratory system $\sigma = \sigma(\beta) = \sigma(E_\gamma, \epsilon, \theta)$.
If the gamma-ray is moving through an isotropic photon gas, then from (2.17) we have $E_\gamma \epsilon \geq 1$ and consequently for the optical depth

$$\tau(E_\gamma) = \int\limits_0^R dr \int\limits_{1/E_\gamma}^{\infty} d\epsilon\, \bar{\sigma}(E_\gamma, \epsilon) n(\epsilon, r), \tag{2.21}$$

---

[1] for example for angle 15° and electron energy 100 GeV (Fig.2.3).

where the angle-averaged cross section can be approximated with an accuracy better than 3% (Aharonian, 2004) by

$$\begin{aligned}\bar{\sigma}(E_\gamma,\epsilon) &= \frac{3\sigma_\mathrm{T}}{2s_0^2}\left[\left(s_0+\frac{\ln s_0}{2}-\frac{1}{6}+\frac{1}{2s_0}\right)\ln\left(\sqrt{s_0}+\sqrt{s_0-1}\right)\right.\\ &\left. -\left(s_0+\frac{4}{9}-\frac{1}{9s_0}\right)\sqrt{1-\frac{1}{s_0}}\right], \qquad (2.22)\end{aligned}$$

where σ_T is the Thomson cross-section and $s_0 = E_\gamma \epsilon$.

For the case of PSR B1259-63/SS 2883, the calculation of the optical depth is presented in the chapter 4. The absorption effect appears to be non significant (Kirk et al., 1999), however one must keep in mind that generally for X-ray binaries with luminous companion stars photon-photon absorption may have a strong impact in the formation of a gamma-ray emission (Moskalenko & Karakula, 1994; Dermer & Boettcher, 2005; Dubus, 2006).

2.3 Synchrotron radiation

Synchrotron radiation occurs when a charged particle moves in a magnetic field (Fig.2.5). Such radiation is similar to bremsstrahlung, where in the present case the "braking" agent is the magnetic field distorting the trajectory of the charged particle.

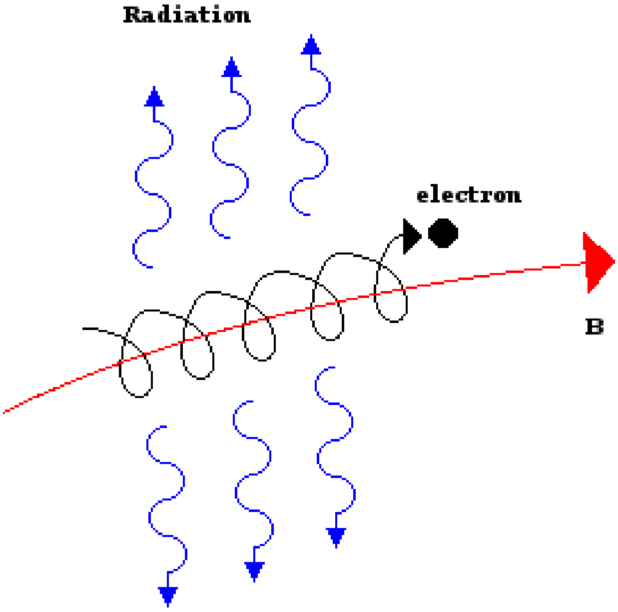

FIGURE 2.5: Synchrotron radiation.

Total[2] (integrated over the emission angle) intensity of the outgoing radiation is given by (Landau & Lifshitz, 1975)

$$\frac{dI}{d\omega} = \frac{\sqrt{3}}{2\pi}\frac{e^3 B_\perp}{mc^2} F\left(\frac{\omega}{\omega_\mathrm{c}}\right) \qquad (2.23)$$

---

[2] One of the characteristic features of the emision of relativistic electrons is that emission is concentrated almost exclusively in a direction of particle's instantaneous velocity. In the case when particle radiates in the chaotic magnetic field, the outgoing radiation is isotropic.

therefore for the number of photons irradiated into dE we have

$$\frac{dN}{dtdE} = \frac{\sqrt{3}}{2\pi}\frac{e^3}{\hbar mc^2}\frac{B_\perp}{E}F\left(\frac{\omega}{\omega_\mathrm{c}}\right), \tag{2.24}$$

with $B_\perp = B\sin\chi$ (χ is the angle between particle momentum and magnetic field vectors), m - the mass of the particle and ω_c is given by

$$\omega_\mathrm{c} = \frac{3}{2}\omega_\mathrm{L}\left(\frac{E_\mathrm{e}}{mc^2}\right)^2 = \frac{3eB_\perp}{2mc}\left(\frac{E_\mathrm{e}}{mc^2}\right)^2 \to \frac{\omega}{\omega_\mathrm{c}} = \frac{E}{\gamma^2}\frac{2m^2c^3}{3\hbar eB_\perp} \simeq 0.2945\cdot 10^{14}\frac{E}{\gamma^2}B_{\perp,\mathrm{G}}^{-1} \tag{2.25}$$

where $E_\gamma = Emc^2$ is outgoing energy of the photon and $\omega_\mathrm{L} = eB/mc$ is the Larmor frequency of the particle.
The function F is given by

$$F(\xi) = \xi\int_\xi^\infty K_{5/3}(\xi)d\xi, \tag{2.26}$$

where K is the MacDonald function.
From the plot of F (Fig.2.6) we can see that the maximum of synchrotron emission occurs at a frequency $\omega_\mathrm{max} = 0.29\,\omega_\mathrm{c}$, i.e. corresponding electron energy is

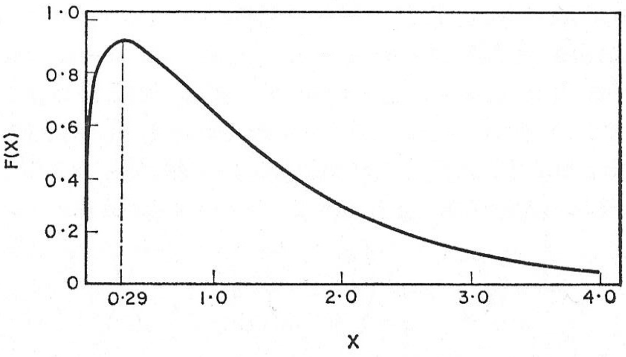

FIGURE 2.6: Plot of the function F from (2.26).

$$E_{\gamma,\mathrm{max}} = 1.925\cdot 10^4 B_{\perp,\mathrm{G}}E_{\mathrm{e,TeV}}^2\,\mathrm{eV}. \tag{2.27}$$

A useful formula for numerical calculations can be obtained using the approximate expression for F

$$F(\xi) \approx 1.86\cdot\xi^{1/3}e^{-\xi} \quad 0.1 \le \xi \le 10 \tag{2.28}$$

which for the irradiated spectrum of a single electron gives

$$\frac{dN}{dtdE} = 6.57\cdot 10^4 B_{\perp,\mathrm{G}}\frac{1}{E}\xi^{1/3}e^{-\xi}\,\mathrm{s}^{-1}. \tag{2.29}$$

Finally, total energy losses of the electron moving in magnetic field are (Blumenthal & Gould, 1970)

$$\frac{d\gamma}{dt} = -\frac{4}{9}r_\mathrm{e}^2\frac{B_\perp^2\gamma^2}{mc}. \tag{2.30}$$

Synchrotron radiation of protons

Although generally synchrotron radiation of protons is considered as an ineffective radiation process, under certain conditions its cooling time can be shorter than the timescale characterizing its acceleration and confinement in an acceleration region. The mathematical formalism of proton synchrotron radiation is identical to the formalism of electron synchrotron radiation.

This means that Larmor frequency $\omega_L = eB_\perp/mc$ must be rescaled (i.e. is smaller) by the factor $m_\mathrm{p}/m_\mathrm{e} \approx 1836$. The characteric energy of the emission is thereby $(m_\mathrm{p}/m_\mathrm{e})^3 \simeq 6 \cdot 10^9$ times smaller than characteristic energy for electron of the same energy

$$E_{\gamma,\mathrm{c}} = \hbar\omega_\mathrm{c} = \sqrt{\frac{3}{2}}\frac{\hbar e B_\perp E_\mathrm{p}^2}{m_\mathrm{p}^3 c^5} \simeq 87\, B_{\perp,\mathrm{G}} E_{\mathrm{p},20}^2\,\mathrm{GeV}, \tag{2.31}$$

where the magnetic field is in Gauss and the energy of protons in 10^{20} eV. Consequently for the same energy of electrons and protons $E_\mathrm{e} = E_\mathrm{p}$ from (2.30) follows that the energy loss rate is $(m_\mathrm{p}/m_\mathrm{e})^4 \simeq 10^{13}$ times smaller than for electrons.

2.4 Bremsstrahlung of relativistic electrons

Bremsstrahlung (free-free emission) radiation is produced when a charged particle, such as an electron, is deflected by another charged particle, such as a nucleus or electron.

For the production of VHE photons only bremsstrahlung involving the ultrarelativistic particles is important, since their kinetic energy must be higher than that of the produced photon. For relativistic protons and nuclei, the intensity of bremsstrahlung on nuclei is more than 10^6 times smaller than for electrons of same energy, therefore we restrict ourselves to bremsstrahlung of electrons.

The scattering of a relativistic electron with Lorentz factor $\gamma \gg 1$ on a nucleus with charge Ze resulting in a production of a photon with energy E_γ (in $m_\mathrm{e}c^2$ units) is characterized by the cross-section (see e.g. Berestetskii et al. 1974)

$$\frac{d\sigma}{dE_\gamma}(E_\gamma,\gamma) = \frac{4Z^2e^2r_\mathrm{e}^2}{\hbar c}\frac{1}{\gamma}\left\{\left[1+\left(1-\frac{E_\gamma}{\gamma}\right)^2\right]\Phi_1 + \left(1-\frac{E_\gamma}{\gamma}\right)\Phi_2\right\} \tag{2.32}$$

with form factors

$$\Phi_1 = \ln\left(2\gamma\frac{\gamma-E_\gamma}{E_\gamma}\right) - \frac{1}{2} \quad , \quad \Phi_2 = -\frac{2}{3}\Phi_1. \tag{2.33}$$

When scattering of electrons occurs on atoms, the electrons in atomic shells are screening the charge of the nucleus and consequently the cross-section of the process changes. Consider the electron with fixed energy travelling near an atom. The screening effect increases with an increase of effective distance r_0 at which the electron passes near the atom. The energy of the radiated photon E_γ increases with decreasing r_0. For big values of E_γ, the cross-section of the process and the shielding effect are small. Therefore the shielding effect is important in low-energy part of the spectrum where the effective distance r_0 is sufficiently big, which leads to a decrease of the irradiated intensity. In the case of complete screening, the bremsstrahling cross-section has simple form

$$\frac{d\sigma}{dE_\gamma}(E_\gamma,\gamma) = \frac{M}{t_\mathrm{rad}E_\gamma} \tag{2.34}$$

where t_{rad} is the radiation length[3] in a gas of atoms with mass M. For small values of r_0 the scattering on electrons in atomic shells must be taken into account. Since in the ultrarelativistic case the cross-section of electron-electron scattering differs from electron-nucleus scattering only by a factor of Z^2, the presence of Z electrons corresponds to the replacement $Z^2 \to Z(Z+1)$ in Eq.2.32.

In each scattering event the electron loses a major fraction of its energy, i.e. bremsstrahlung is a catastrophic process. This means that the energy E_γ of the emitted photon is of the order of electron energy $E_\gamma \sim \gamma$, therefore electron bremsstrahlung is one of the most effective processes of production of VHE γ-ray emission.

Detailed reviews of bremsstrahlung cross-section properties and spectra can be found e.g. in Blumenthal & Gould 1970, Akhiezer & Berestetskii 1965, Aharonian 2004.

2.5 π^0-decay gamma-rays

In the interactions of cosmic ray nuclei with an interstellar medium, π^0-mesons (pions) are formed. This is basically related to $p-p, p-\alpha, \alpha-p$ reactions (p - proton, α - helium nucleus) - consequently this process provides information about the hadronic component of cosmic rays.

A pion is decaying into two γ photons in a time of the order of 10^{-16} s (π^0-meson lifetime). In the rest frame of a pion, both photons have energy $m_\pi c^2/2 \approx 70\,\mathrm{MeV}$ and are travelling in opposite directions. In the laboratory frame this energy is

$$E_\gamma = \frac{m_\pi c^2}{2}\left(\frac{1+\frac{v}{c}\cos\theta}{\sqrt{1-\frac{v^2}{c^2}}}\right) \tag{2.35}$$

with θ being the angle between momentum vectors of photon k'_γ and pion p_π. Since the decay is isotropic in the pion's rest frame, the distribution of laboratory energies is flat with its limits determined by $\cos\theta = \pm 1$

$$\frac{m_\pi c^2}{2}\sqrt{\frac{1-v/c}{1+v/c}} \le E_\gamma \le \frac{m_\pi c^2}{2}\sqrt{\frac{1+v/c}{1-v/c}}. \tag{2.36}$$

By taking the logarithm of this expression we see that the distribution of decayed photons is symmetric around 70 MeV when plotted vs $\ln E_\gamma$.

Each nuclear reaction can produce multiple pions, however for large energies of interacting particles only one pion is taking the major part of the kinetic energy of the proton of order 20%. Spectra calculations of the process $pp \to \pi^0 \to \gamma\gamma$ are done using cross-section data from accelerators. Although precise calculations of γ-ray spectra are quite difficult (see e.g. Mori (1997)), the emissivity of γ-rays for arbitrary broad energy distribution of protons can be derived within a simple formalism (Aharonian, 2004).

γ-ray emissivity $q_\gamma(E_\gamma) = dN_\gamma/dt\,dE_\gamma$ can be directly obtained from the emissivity of pions by (see e.g. two body decay problem in Landau & Lifshitz 1975)

$$q_\gamma(E_\gamma) = 2\int\limits_{E_{\min}}^{\infty} \frac{q_\pi(E_\pi)}{\sqrt{E_\pi^2 - m_\pi^2 c^4}} dE_\pi, \tag{2.37}$$

---

[3] The radiation length (in g/cm^2) is the average distance over which the ultrarelativistic electron loses all but $1/e$ of its energy and is determined theoretically or from experimental data. For example for hydrogen $t_{\mathrm{H}} = 69.4$.

with the minimum energy obtained from energy conservation law

$$E_{\min} = E_\gamma + \frac{m_\pi^2 c^4}{4E_\gamma}. \tag{2.38}$$

The emissivity of secondary pions q_π can be calculated using cross-sections $\sigma(E_i, E_\mathrm{p})$ obtained from accelerators (see e.g. Gaisser 1990). The emissivity of π^0-mesons calculated using the δ-function approximation for the cross-section $\sigma(E_\pi, E_\mathrm{p})$ then is

$$\begin{aligned} q_\pi(E_\pi) &= c\,n_\mathrm{H} \int \delta\left(E_\pi - \kappa_\pi E_\mathrm{kin}\right) \sigma_\mathrm{pp}(E_\mathrm{p}) n_\mathrm{p}(E_\mathrm{p}) dE_\mathrm{p} \\ &= \frac{c\,n_\mathrm{H}}{\kappa_\pi} \sigma_\mathrm{pp}\left(m_\mathrm{p}c^2 + \frac{E_\pi}{\kappa_\pi}\right) n_\mathrm{p}\left(m_\mathrm{p}c^2 + \frac{E_\pi}{\kappa_\pi}\right) \end{aligned} \tag{2.39}$$

where $\sigma_\mathrm{pp}(E_\mathrm{p})$ is the total cross section of inelastic *pp* collisions, κ_π is the mean fraction of the kinetic energy $E_\mathrm{kin} = E_\mathrm{p} - m_\mathrm{p}c^2$ of the proton transferred to the secondary π^0-meson per collision, $n_\mathrm{p}(E_\mathrm{p})$ is the energy distribution of the protons and n_H is the density of H-atoms. The relatively good accuracy of this simple approach is shown in Aharonian & Atoyan (2000).

2.6 Energy losses of electrons

Knowledge of energy losses of electrons is essential in a determination of the formed spectrum (chapter 4). Since in this work we propose VHE component of radiation originating from electrons, let us present a short overview of relevant electron energy losses and the corresponding formulae.

1. **Synchrotron losses** (magnetic bremsstrahlung) - electron spiraling in magnetic field loses its energy at a rate

$$\frac{d\gamma}{dt} = -\frac{4}{9} r_\mathrm{e}^2 \frac{B_\perp^2 \gamma^2}{mc} = 1.29 \cdot 10^{-9} B_{\perp,\mathrm{G}}^2 \gamma^2\,\mathrm{s}^{-1} \tag{2.40}$$

where $r_\mathrm{e} = e^2/mc^2 = 2.82.10^{-13}$cm is the classical electron radius and B is the magnetic field component perpendicular to the electron's velocity.

2. **Inverse Compton losses** - electron travelling in external isotropic photon field with the density $n(\epsilon)$ loses its energy at a rate

$$mc^2 \frac{d\gamma}{dt} = \int (E_\gamma - \epsilon) \frac{dN}{dt dE_\gamma} dE_\gamma = c \int (E_\gamma - \epsilon) \frac{d\sigma_\mathrm{is}}{dE_\gamma} n(\epsilon) d\epsilon dE_\gamma, \tag{2.41}$$

where $d\sigma_\mathrm{is}/dE_\gamma$ is the isotropic IC cross-section integrated over scattering angle.
In the Thomson and Klein-Nishina regimes the energy losses are given by well known expressions (see e.g. Blumenthal & Gould 1970):

$$\begin{aligned} mc^2 \frac{d\gamma}{dt} &= -\frac{4}{3} \sigma_\mathrm{T} c w_\mathrm{ph} \gamma^2 && \text{Thomson} \quad (2.42) \\ mc^2 \frac{d\gamma}{dt} &= -\frac{3}{8} \sigma_\mathrm{T} m^2 c^5 \int d\epsilon\, \frac{n(\epsilon)}{\epsilon} \left(\ln \frac{4\epsilon\gamma}{mc^2} - \frac{11}{6}\right) && \text{K. – N.} \quad (2.43) \end{aligned}$$

with w_ph being the desity of a photon field.

3. **Bremsstrahlung** - ultrarelativistic electron interacting with a nucleus with atomic number Z radiates its energy at a rate (Berestetskii et al., 1974)

$$\frac{d\gamma}{dt} = -4n_{\rm Z}Z^2\alpha r_{\rm e}^2 c\gamma\left(\ln\frac{2\gamma}{mc^2}-\frac{1}{3}\right) = -0.7\cdot 10^{-16}Z^2\gamma n_{\rm Z,cm^{-3}}\left(\ln 2\gamma-\frac{1}{3}\right)\ {\rm s}^{-1} \quad (2.44)$$

where $n_{\rm Z}$ is the concentration of scatterers with atomic number Z.
In the case of complete screening

$$\frac{d\gamma}{dt} = -4n_{\rm Z}Z^2\alpha r_e^2 c\gamma\ln\left(\frac{1}{\alpha Z^{1/3}}\right) = -0.7\cdot 10^{-16}Z^2\gamma n_{\rm Z,cm^{-3}}\ln\frac{137}{Z^{1/3}}\ {\rm s}^{-1}, \quad (2.45)$$

When taking into account the interaction with Z electrons in the atomic shell, Z^2 in (2.44) must be replaced by $Z(Z+1)$.

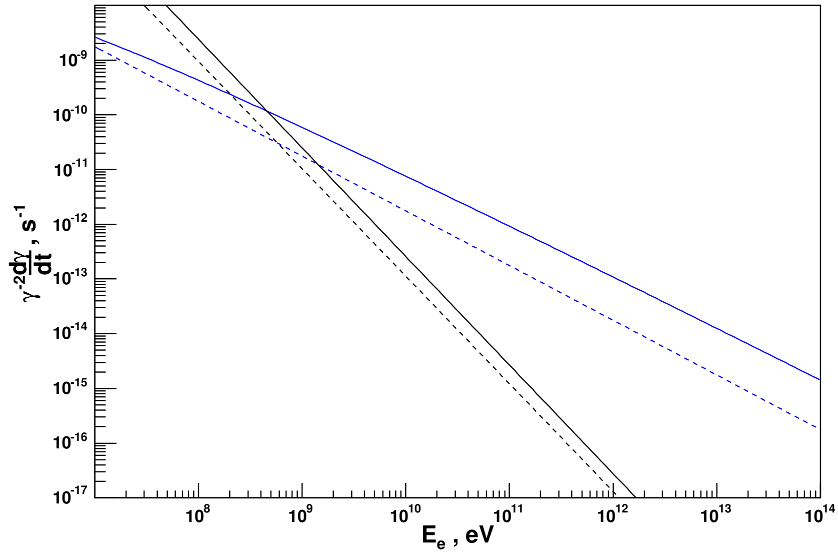

FIGURE 2.7: Comparison of the ionization and bremsstrahlung energy losses. Blue dashed line represents bremsstrahlung on shielded atoms and blue solid line on non-shielded atoms. Black dashed line represents the ionization losses in a non-ionized gas and black solid line in a fully ionized gas. The density of hydrogen atoms is chosen to be $10^8\,{\rm cm}^{-3}$.

4. **Ionization losses**. Ionization occurs when an electron interacting with an atom gives enough energy to excite the atom or free the atomic electron from its shell. The energy loss of electron in the ultrarelativistic case is given by the formula (Ginzburg & Syrovatskii, 1964)

$$\frac{d\gamma}{dt} = -\frac{2\pi e^4 n_{\rm H}}{m^2c^3}\left(\ln\frac{\gamma^3m^2c^4}{I^2}-2\right) \approx -1.495\cdot 10^{-14}n_{\rm H,cm^{-3}}\left(\ln\gamma+19\right){\rm s}^{-1}, \quad (2.46)$$

with $n_{\rm H}$ being the concentration of hydrogen atoms and $I \sim 15\,{\rm eV}$ the effective ionization energy of the hydrogen atom.
When a medium is placed into a photon field with sufficient integral number density above the ionization potential of the atoms of the medium, the gas becomes fully ionized. In a fully ionized gas the ionization losses in the ultrarelativistic case are given

by the formula (Ginzburg & Syrovatskii, 1964)

$$\frac{d\gamma}{dt} = -\frac{2\pi e^4 n_{\mathrm{H}}}{m^2 c^3}\left(\ln\frac{m^3 c^4 \gamma}{4e^2 n_{\mathrm{H}} \hbar^2} - \frac{3}{4}\right) \approx -1.495\cdot 10^{-14} n_{\mathrm{H,cm^{-3}}}\left(\ln\frac{\gamma}{n_{\mathrm{H}}} + 74.7\right)\,\mathrm{s}^{-1}. \tag{2.47}$$

Chapter 3

Geometry of PSR B1259-63/SS 2883

The geometry of the binary PSR B1259-63/SS 2883 plays an important role in the determination of the various dynamic parameters of the system.
The pulsar is moving around the massive Be-star in a Keplerian orbit and its distance from the star can be calculated from the system's eccentricity, orbital period and periastron distance. Combined with the parameters characterizing a pulsar and stellar winds it can be used to determine the distance to the shock (shock radius), i.e. the region where pulsar electrons are accelerated and isotropised on a shockwave. The shock radius gives us the information about the orbital dependance of the soft photon Be star field and the compressed magnetic field in the interaction region - two parameters characterizing the IC and synchrotron processes present in the formation of the electron and consequently irradiated spectra.
The position of the binary on the sky is given by orbital parameters of the system and is necessary to extract the information about the anisotropy ofthe IC scattered gamma rays detected on Earth.

At the beginning of this chapter, the dynamics of pulsar Keplerian motion around the Be star along with the IC scattering angle are calculated. Afterwards, we proceed with the calculation of shock radius for the various scenarios of pulsar and stellar wind interaction and geometry. While the determination of the resulting soft photon field is trivial[1], the orbital dependance of the magnetic field needs more detailed analysis, which is presented after. At the end, relevant points from shock acceleration theory are presented needed to justify the shape of the accelerated electron spectrum, which is used later in our calculations.

3.1 The orbit

The pulsar's motion around the star[2] is described by Kepler's equation derived from Kepler's laws

$$E - e \sin E = \frac{2\pi t}{T}, \tag{3.1}$$

where T is the orbital period and e is the eccentricity of an ellipse. Let us consider the geometry shown in Fig.3.1. By drawing the line perpendicular to the y-axis which goes

---

[1] Namely, blackbody distribution with temperature T is diluted by a factor $(R_*/2R_\mathrm{s})^2$ with R_s the distance Be star to shock.

[2] Mass of the star is one order of magnitude bigger than pulsar mass, therefore we consider approximation of static star.

throughthe pulsar position and intersects it with a circle of radius a originating at the point O we obtain the point T. The angle between the line OT and the y-axis is called the eccentric anomaly $E(t)$.

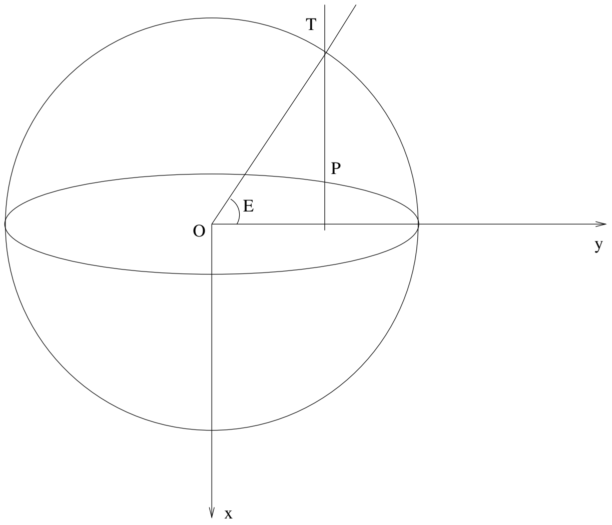

FIGURE 3.1: Eccentric anomaly.

In our geometry the pulsar coordinates are

$$P = (-b \sin E, a \cos E). \tag{3.2}$$

where a, b are the semimajor and semiminor ellipse axes, respectively.
Hence, the distance r between the pulsar and the star located at the focus of the ellipse $(0, c, 0)$ is[3]

$$r^2 = b^2 \sin^2 E + (c - a \cos E)^2. \tag{3.3}$$

In Fig.3.2 the distance pulsar-star is shown for different positions of the pulsar on the orbit. Because of the large value of the eccentricity ($e = 0.87$), the difference between distance at the periastron ($d_{\rm per} = 9.6 \cdot 10^{12}$ cm) and distance at apastron ($d_{\rm ap} = 1.4 \cdot 10^{14}$ cm) is quite large ($\approx$ 15-fold).

Knowledge of the orbital dependance of the star-pulsar separation allows us to proceed to the calculation of the angle characterizing the anisotropy of IC scattering. In the proposed model, the pulsar electrons isotropised on a shockwave scatter narrow beam of target photons from a Be-star. In the previous chapter it was shown that only the electrons moving towards the observer are contributing to IC scattering at high energies (2.10). Therefore, assuming that the scattering takes place in the close vicinity of the pulsar (this assumption will be justified in the next section), the scattering angle θ is given by $\theta = \pi - \psi$, where ψ is the angle star-pulsar-observer (see Fig.3.3).

To calculate the angle ψ we need quantities characterizing the position of the orbiting plane on the sky. These are the so-called orbital parameters and are defined as

- **Inclination angle** i - the angle between the plane of the orbit (xy-plane in Fig.3.4) and the plane perpendicular to the line of sight.

---

[3] Parameters a, b, c are obtained from eccentricity e and periastron distance $d_{\rm per}$ using standard relations for the ellipse.

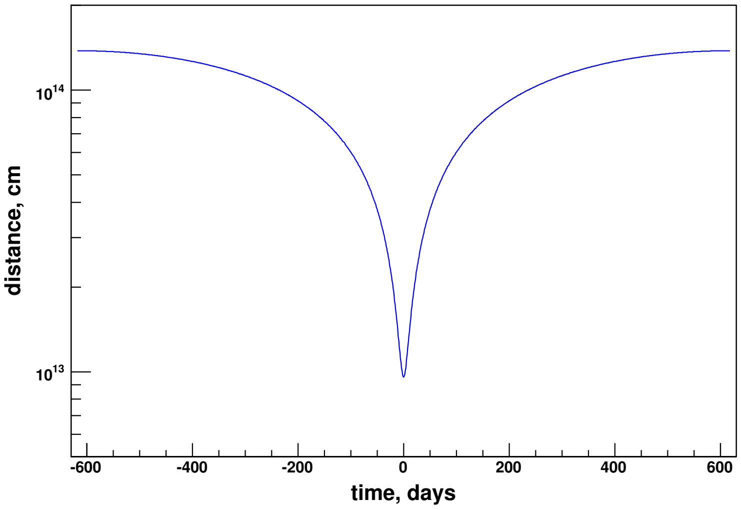

FIGURE 3.2: Distance pulsar-star for various days on pulsar orbit.

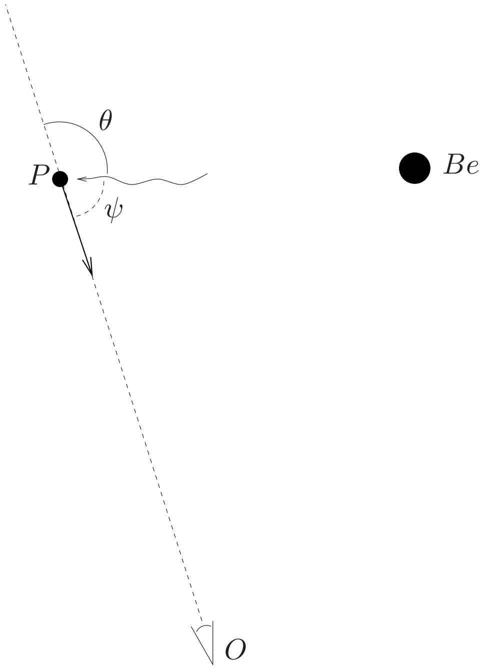

FIGURE 3.3: Scattering angle geometry of the IC process for the PSR 1259-63/SS 2883 binary system.

- **Longitude of periastron** ω - the angle between the position of periastron and the intersection line of this two planes.

Choosing the coordinate system which corresponds to the pulsar-star distance calculation (Fig.3.4) with the major axis of the elliptical orbit lying on the y-axis, our goal is to find the normal vector $\vec{n}$ of the plane Q. This can be achieved by a rotation of the xy-plane (characterized by the normal unit vector $\vec{n}_{xy} = (0, 0, -1)$) first around the x-axis by the angle i in the negative direction and afterwards by rotation of the resulting plane around the z-axis by the angle $(\omega - \pi/2)$ in the negative direction. Denoting the distance star-observer

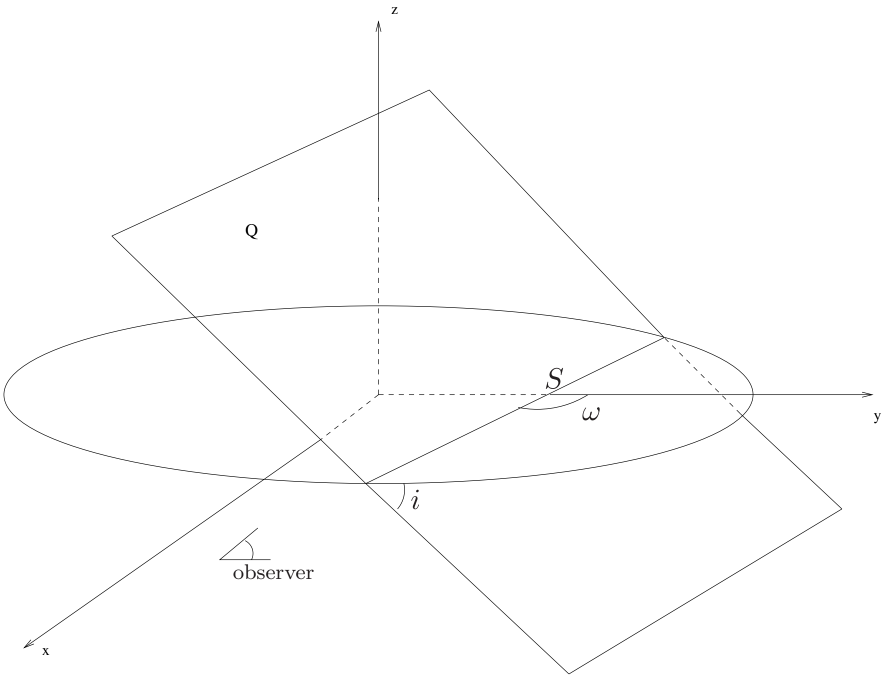

Figure 3.4: Orbital parameters.

by D, this gives for the observer's coordinates

$$\begin{aligned} x &= D\cos\omega\sin i \\ y &= c - D\sin\omega\sin i \\ z &= -D\cos i \quad . \end{aligned} \tag{3.4}$$

Hence denoting the pulsar-observer separation by s, the angle ψ is obtained from the cosine theorem

$$\begin{aligned} \cos\psi &= \frac{r^2+s^2-D^2}{2rs} = \\ &= \frac{r^2 + D\sin i(a\cos E\sin\omega + b\sin E\cos\omega - c\sin\omega)}{r\sqrt{D^2+2D\sin i(a\cos E\sin\omega + b\sin E\cos\omega - c\sin\omega)+r^2}}, \end{aligned} \tag{3.5}$$

and using $r \ll D$ we have

$$\cos\psi \approx \frac{\sin i(a\cos E\sin\omega + b\sin E\cos\omega - c\sin\omega)}{r}. \tag{3.6}$$

From the last equation we see that the anisotropy of scattering does not depend on a distance from a source D as long as $r \ll D$ holds. The calculated dependance of the scattering angle is shown in Fig.3.5. It has a maximum at 6 days before periastron and after that quickly drops by a factor of 2. Note that for the same spectra of electrons and soft photon fields, the shape of the outgoing IC radiation for different angles will be similar to the one in Fig.3.5. This is naturally related to the fact that the probability of scattering increases with an increase of the scattering angle (with a maximum for head-on collision $\theta = \pi$).

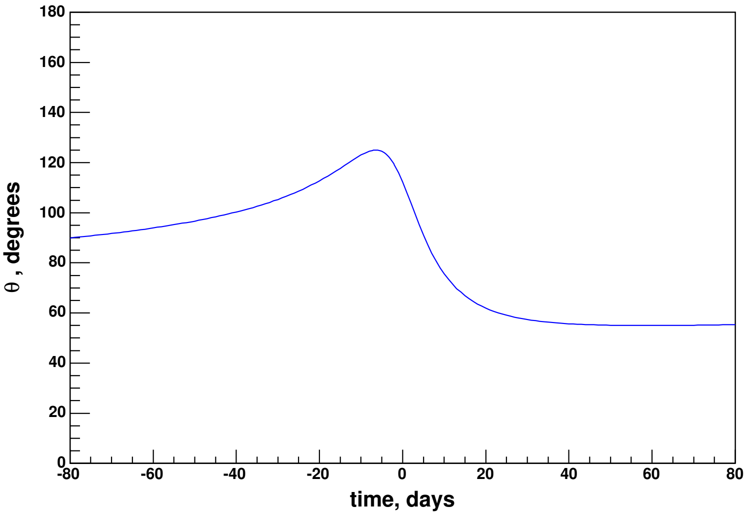

FIGURE 3.5: Scattering angle dependance on epoch ±80 days around periastron.

3.2 Calculation of the termination shock radius

The distance of the pulsar from a shock resulting from the interaction of a pulsar wind with stellar outflow divides the interaction of the pulsar wind with soft photon field into two significantly different parts. Namely, in a pre-termination region the pulsar wind is cold (i.e. has a narrow energy distribution), and consequently its interaction with soft photons will result in a narrow band energy spectrum of VHE photons. On the other hand, in a post-shock region, the formed spectrum of the electrons interacting with star photons is isotropic. Moreover, the orbital dependance of the shock radius is necessary in determination of orbital variation of the magnetic and photon fields present in radiation processes. In this section we will calculate the orbital shock radius dependance following similar logic as in a paper of Tavani & Arons (1997).

The location of the shock region is given by Rankine-Hugoniot jump conditions

$$p_{\mathrm{p}} + \rho_{\mathrm{p}} v_{\mathrm{p}}^2 = p_{\mathrm{Be}} + \rho_{\mathrm{Be}} v_{\mathrm{Be}}^2, \tag{3.7}$$

with p the thermal and $P = \rho v^2$ dynamic wind pressures. v denotes the component of the wind's velocity at a shock position normal to the plane of the shock. Since the Be star outflow is highly supersonic (measured temperatures of the Be-star winds are of the order 10^4K (Waters et al., 1988) corresponding to the sound speeds of order $10\,\mathrm{km\,s^{-1}}$), its thermal pressure can be neglected. According to the standard PWN (Pulsar Wind Nebulae) model (Kennel & Coroniti, 1984a), more than 99% of pulsar spindown luminosity is converted into kinetic energy of cold isotropic ultrarelativistic wind (L_{kin}), which implies zero thermal pressure and dynamic wind pressure $\rho_{\mathrm{p}} v_{\mathrm{p}}^2 = L_{\mathrm{kin}}/4\pi r_{\mathrm{s}}^2 \approx L/4\pi r_{\mathrm{s}}^2$.

Summarizing, the condition of pressure balance for the case of the aligned planes of pulsar orbit and Be star disc gives

$$\frac{L}{4\pi c r_{\mathrm{s}}^2} = P_{\mathrm{eq}}(R_{\mathrm{s}}) + P_{\mathrm{pol}}(R_{\mathrm{s}}), \tag{3.8}$$

with $P_{\mathrm{eq}}(R_{\mathrm{s}})$ from Eq.(1.5), $P_{\mathrm{pol}}(R_{\mathrm{s}})$ from Eq.(1.8) and

$$r(\phi) + R_{\mathrm{s}}(\phi) = d(\phi), \tag{3.9}$$

where ϕ is the true anomaly.
The radial velocity of the wind is distorted by pulsar orbital motion, and its velocity is

$$v_{\mathrm{p,r}} = v_{\mathrm{K}} \frac{e \sin\phi}{\sqrt{1-e^2}} \tag{3.10}$$

$$v_{\mathrm{p},\phi} = v_{\mathrm{K}} \frac{1 + e\cos\phi}{\sqrt{1-e^2}}, \tag{3.11}$$

$$v_{\mathrm{K}} = \sqrt{G\frac{M_{\mathrm{p}} + M_{\mathrm{Be}}}{a}} \simeq 4.53 \cdot 10^6\,\mathrm{cm\,s^{-1}}, \tag{3.12}$$

with the Keplerian velocity v_{K} and ellipse major axis a. For our eccentricity value of $e = 0.87$ the pulsar radial velocity is

$$v_{\mathrm{p,r}} = \sin\phi \cdot 7.99 \cdot 10^6\,\mathrm{cm\,s^{-1}}. \tag{3.13}$$

This value is small compared to the estimated value of the star equatorial wind $v_{\mathrm{eq}} \sim 300\,\mathrm{km\,s^{-1}}$ and negligible compared to the estimated terminal velocities of the polar wind $v_\infty \sim 10^3\,\mathrm{km\,s^{-1}}$, therefore this effect can be neglected.

Observations of the investigated binary (see section 1.3) indicate substantial inclination between the Be star plane and the orbit, therefore our case needs the modeling of the equatorial wind with inclination angle dependency. For the aligned model in a spherical coordinate system we had (Fig.3.6)

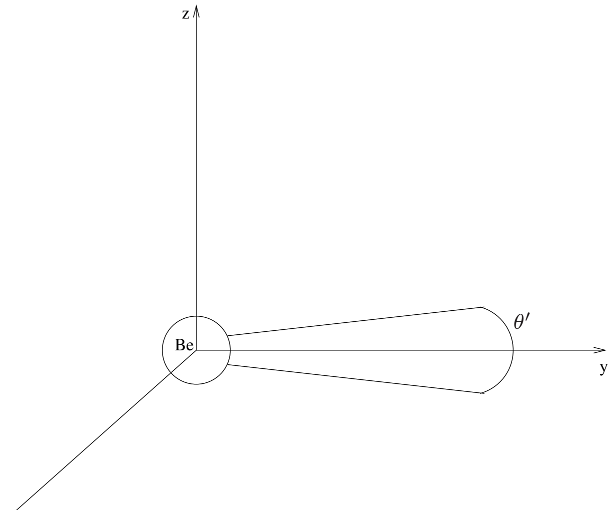

FIGURE 3.6: Modeling of Be-star wind for the aligned disc model

$$P_{\mathrm{eq}} = \rho_{0,\mathrm{eq}} v_{0,\mathrm{eq}}^2 \left(\frac{R}{R_*}\right)^{n-4} f(\theta) \tag{3.14}$$

with $f(\theta)$ characterizing the width of the disc

$$f(\theta) = 1 \quad , \quad \theta \in \left(\frac{\pi}{2} - \theta'; \frac{\pi}{2} + \theta'\right), \tag{3.15}$$

and θ' is the disc half-opening angle.

For the misaligned model the equatorial disc profile angle dependance is fitted with the gaussian (Fig.3.7)

$$f_{-,+}(\theta) = A\exp\left[-\frac{1}{2}\left(\frac{\theta-\theta_{-,+}}{\theta'}\right)^2\right]. \tag{3.16}$$

with $-,+$ being the values of the angle θ for -19, $+15$ days around the periastron (i.e. the centers of the disc inferred from the observations), respectively, where th true anomaly θ is related to the eccentric anomaly E by

$$\cos\theta = \frac{\cos E - e}{1 - e\cos E}. \tag{3.17}$$

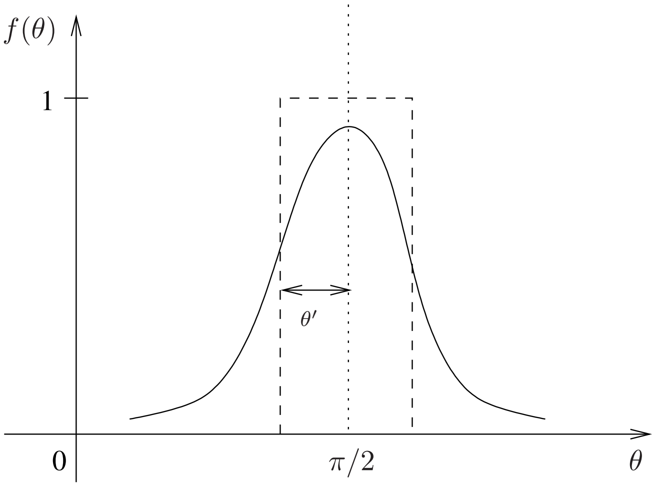

FIGURE 3.7: Fitting of the Be-star equatorial wind component with the gaussian.

The constant of proportionality A can be found from

$$A\int_0^{\pi}\exp\left[-\frac{1}{2}\left(\frac{\theta-\pi/2}{\theta'}\right)^2\right]\sin\theta d\theta = \int_{\frac{\pi}{2}-\theta'}^{\frac{\pi}{2}+\theta'}\sin\theta d\theta, \tag{3.18}$$

and using the fact that the disc half-opening angle is small $\simeq 7.5^\circ$ ($3\theta' \simeq 22.5^\circ \ll 90^\circ$) yields

$$A = \sqrt{\frac{2}{\pi}}\frac{\sin\theta'}{\theta'}e^{\theta'^2/2}, \tag{3.19}$$

giving $A \doteq 0.8$.

The formula (3.16) is valid for the case when the angle between the orbital plane and the plane of the disc is $\pi/2$ (Fig.3.8). If we introduce an arbitrary inclination angle ψ, the width of the gaussian in Eq.(3.16) has to be replaced by

$$\theta' \to \theta'/\sin\psi. \tag{3.20}$$

In Fig.3.9 the ratio shock radius / distance pulsar-star is shown for different angles between the orbital and disc planes. We see from Fig.3.10 that for the adopted parameters of Be-star wind this ratio can vary significantly. However, to date there are no observations which determined the mass loss rates of SS 2883. From the mass loss rates obtained for different Be stars we see that the most probable value of this ratio is ~ 0.8.

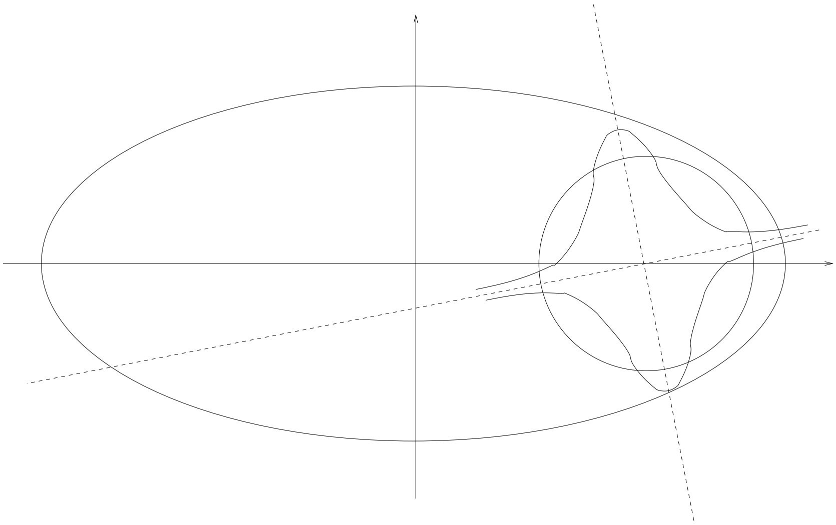

FIGURE 3.8: Be-star equatorial wind field in the pulsar plane for a fixed value of distance from the star.

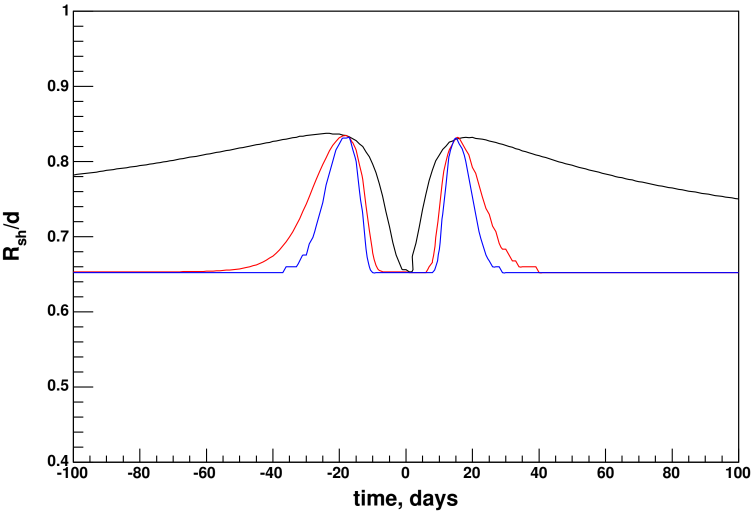

FIGURE 3.9: Ratio of the shock distance to distance between pulsar and a star for various inclinations of the equatorial disk plane. Black line represents an inclination of 15 degrees, red line - 45 degrees, blue line - 90 degrees. The outflow parameters of the disk were taken as: $\rho_{0,\mathrm{eq}} = 2.5 \cdot 10^{-11}\,\mathrm{g\,cm^{-3}}$, $v_{0,\mathrm{eq}} = 10^6\,\mathrm{cm\,s^{-1}}$, $\dot{M}_{\mathrm{UV}} = 5 \cdot 10^{-9} M_{\odot}/yr$, $v_{\infty} = 3 \cdot 10^8\,\mathrm{cm\,s^{-1}}$

Since the variety of observations favor the values of stellar wind implying the shock distance close to the pulsar, we will consider the case when[4] $r_{\mathrm{s}} \ll d$ and $r_{\mathrm{s}} > r_{\mathrm{LC}}$[5].

---

[4] One must keep in mind that the case of the shock taking place in the vicinity of the Be star is *not* excluded.

[5] For the possible parameters of the outflows of PSR B1259-63/SS 2883 this condition is satisfied as shown in Tavani & Arons (1997)

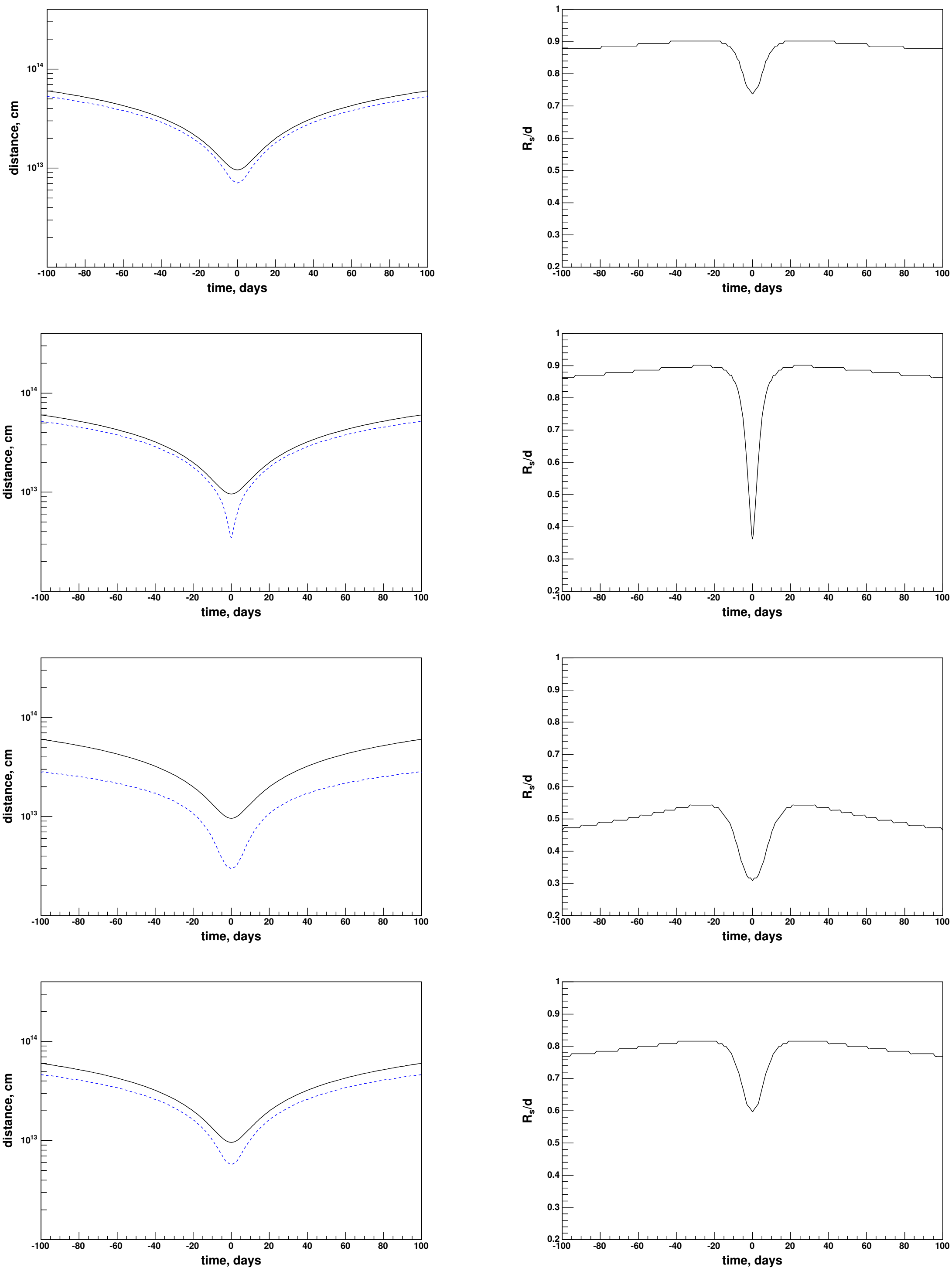

FIGURE 3.10: Shock radius dependance on the orbital time for the angle 15° between the Be-star disc and pulsar orbital planes. Left-side plots show the comparison of shock radius (dashed line) with the distance pulsar-Be (solid line). Right-side plots show the dependance of ratio R_s/d on the orbital position. The plots are arranged for different parameters of equatorial and polar wind components as follows: 1st row - $EQ_\mathrm{max}, POL_\mathrm{max}$, 2nd row - $EQ_\mathrm{max}, POL_\mathrm{min}$, 3rd row - $EQ_\mathrm{min}, POL_\mathrm{min}$, 4th row - $EQ_\mathrm{typ}, POL_\mathrm{typ}$.

The values of maximal and minimal wind parameters were chosen as: EQ_max - $\rho_0 = 10^{-10}\,\mathrm{g\,cm^{-3}}$, EQ_min - $\rho_0 = 10^{-11.6}\,\mathrm{g\,cm^{-3}}$, POL_max - $\dot{M}_\mathrm{UV} = 10^{-8}\,M_\odot/\mathrm{yr}$, $v_\infty = 3500\,\mathrm{km\,s^{-1}}$, POL_min - $\dot{M}_\mathrm{UV} = 10^{-9}\,M_\odot/\mathrm{yr}$, $v_\infty = 1000\,\mathrm{km\,s^{-1}}$, and the values of typical wind parameters are EQ_typ - $\rho_0 10^{-10.6}\,\mathrm{g\,cm^{-3}}$, POL_typ - $\dot{M}_\mathrm{UV} = 7{\cdot}10^{-9}\,M_\odot/\mathrm{yr}$, $v_\infty = 2000\,\mathrm{km\,s^{-1}}$.

3.3 Geometry of the pulsar wind cavity.

The basic pulsar wind cavity geometry, i.e. which wind dominates near the line connecting the pulsar and a star, depends on the form of the pressure law characterizing both winds. In analogy with the previous section, let us assume a general power-law distribution of the dynamic wind pressures characterizing pulsar and star winds,

$$P_{\rm p} = \left(\frac{A^2}{r^2}\right)^w \quad , \quad P_{\rm Be} = \left(\frac{B^2}{R^2}\right)^z , \tag{3.21}$$

with positive coefficients A, B, w, z, r - the radial distance from the pulsar and R - the radial distance from the star. The shock radius is given by the equation

$$P_{\rm p}(r_{\rm s}) = \left(\frac{A^2}{r_{\rm s}^2}\right)^w = \left(\frac{B^2}{R_{\rm s}^2}\right)^w = P_{\rm Be}(R_{\rm s}) \quad , \quad R_{\rm s} + r_{\rm s} = d. \tag{3.22}$$

Consider the point T shifted by an infinitesimal distance y perpendicular to the line between the pulsar and a star (see figure below). We will investigate the magnitude of the dynamic pressures acting on a surface given by y to determine which wind is dominant. The corresponding pressures at the point T are

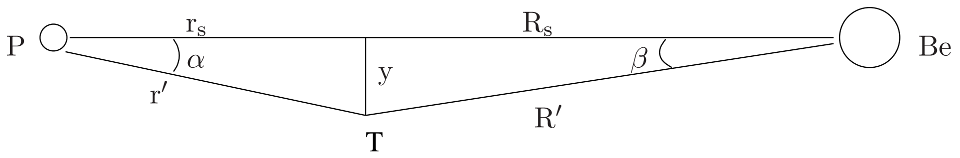

$$P_{\rm p}(T) = \left(\frac{A^2}{r'^2}\right)^w \cos^2\alpha = \left(\frac{A^2}{r'^2}\right)^w \frac{r_{\rm s}^2}{r'^2} = P_{\rm p}(r_{\rm s})\left(1 + \frac{y^2}{r_{\rm s}^2}\right)^{-w-1} \tag{3.23}$$

$$P_{\rm Be}(T) = \left(\frac{B^2}{R'^2}\right)^z \cos^2\beta = \left(\frac{B^2}{R'^2}\right)^z \frac{R_{\rm s}^2}{R'^2} = P_{\rm Be}(R_{\rm s})\left(1 + \frac{y^2}{R_{\rm s}^2}\right)^{-z-1} \tag{3.24}$$

and consequently their ratio is

$$\frac{P_{\rm p}(T)}{P_{\rm Be}(T)} = \frac{\left(1 + \frac{y^2}{R_{\rm s}^2}\right)^{z+1}}{\left(1 + \frac{y^2}{r_{\rm s}^2}\right)^{w+1}}. \tag{3.25}$$

Let us investigate the case when the wind from the Be-star is dominant, i.e. the pressure ratio (3.25) is smaller than 1. Expanding this expression up to first order in

$$\frac{y}{R_{\rm s}} \ll 1 \quad , \quad \frac{y}{r_{\rm s}} \ll 1 \tag{3.26}$$

gives

$$\frac{P_{\rm p}(T)}{P_{\rm Be}(T)} \approx \frac{1 + (z+1)\frac{y^2}{R_{\rm s}^2}}{1 + (w+1)\frac{y^2}{r_{\rm s}^2}} < 1 \tag{3.27}$$

and this yields

$$R_{\rm s} > \frac{d}{1 + \sqrt{\frac{w+1}{z+1}}}. \tag{3.28}$$

Correspondingly for the case when the pulsar wind is dominant

$$R_\mathrm{s} < \frac{d}{1+\sqrt{\frac{w+1}{z+1}}}. \tag{3.29}$$

Let us investigate two cases relevant for the investigated binary:

1. The region where the Be-star wind is characterized by its polar component. In this case we have $w = z = 1$ and the equations (3.28),(3.29) result in $R_\mathrm{s} > d/2$ (fig. 3.11) and $R_\mathrm{s} < d/2$ (fig. 3.12) respectively.

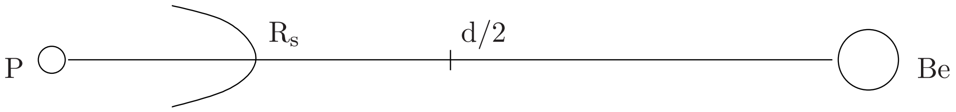

FIGURE 3.11: Schematic drawing of the shock front for the case of a dominant Be-star wind.

2. The region where the Be-star wind is characterized by its equatorial wind outflow component. This region is characterized by wind exponents $w = 1$ and $z = 1/2$ which gives $R_\mathrm{s} > d/(1+2\sqrt{1/3})$ and $R_\mathrm{s} < d/(1+2\sqrt{1/3}) \approx 0.46\,d$, respectively.

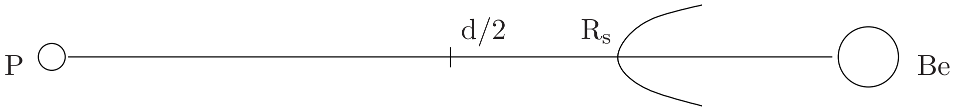

FIGURE 3.12: Schematic drawing of the shock front for the case of a dominant pulsar wind.

3.4 Magnetic field at the shock

As mentioned before, we use the model of Kennel & Coroniti (1984a) according to which pulsars lose their rotational energy in the form of relativistic MHD winds, which carry energy in form of kinetic energy of the plasma and the energy of the electromagnetic field. Total spindown luminosity of the pulsar can be divided into the electromagnetic and kinetic parts

$$L = L_\mathrm{em} + L_\mathrm{k} = L_\mathrm{em}\left(1+\frac{1}{\sigma}\right), \tag{3.30}$$

with σ being the ratio of electromagnetic and kinetic energies. For the radial outflow from the pulsar we have

$$L_\mathrm{em} = 4\pi r_\mathrm{s}^2 c\, U_\mathrm{em}, \tag{3.31}$$

therefore

$$\frac{L}{4\pi r_\mathrm{s}^2 c} = U_\mathrm{em}\left(1+\frac{1}{\sigma}\right). \tag{3.32}$$

In order to calculate the electromagnetic field density U_em we transform into the local rest (primed) system of the pulsar and for simplicity we assume that in this system the magnetic field is oriented in direction of the z-axis. The Lorentz transformation formulae then give

$$B = B_\mathrm{z} = \gamma B'_\mathrm{z} \quad , \quad E = E_\mathrm{y} = \gamma\beta B'_\mathrm{z} = \beta B_\mathrm{z}, \tag{3.33}$$

and for the electromagnetic energy density we obtain

$$U_{\rm em} = \frac{B_{\rm z}^2 + E_{\rm y}^2}{8\pi} \approx \frac{B^2}{4\pi}, \tag{3.34}$$

since $\beta \approx 1$[6]. Finally we arrive at the formula for the magnitude of the electromagnetic field

$$B^2 = \frac{L}{r_{\rm s}^2 c} \frac{\sigma}{\sigma + 1}. \tag{3.35}$$

Using the value of $r_s = 0.1\,d_{\rm per}$ ($d_{\rm per}$ - periastron distance) and $\sigma = 0.003$[7] the upstream magnetic field is $B_{\rm per} \sim 0.3\,{\rm G}$ (At the shock discontinuity the magnetic field in downstream region is $B_{\rm d} \simeq 3\,B$ (Kennel & Coroniti, 1984a)).[8]
We are interested in orbital dependance of magnetic field on the pulsar-star separation, which can be calculated from the so-called "frozen-in" condition. MHD equation of motion (Landau & Lifshitz, 1959) for ideal plasma is

$$\frac{d}{dt}\left(\frac{\vec{B}}{\rho}\right) = \left(\frac{\vec{B}}{\rho}\vec{\nabla}\right)\vec{v}. \tag{3.36}$$

Let us consider the liquid line - the line which moves with its particles of plasma. Denote by $\vec{\delta l}$ the length element of this line. We will determine how it changes with time. If $\vec{v}$ is the velocity on the one side of the element $\vec{\delta l}$, then the velocity on the second side of the same element is $\vec{v} + (\vec{\delta l}\vec{\nabla})\vec{v}$. Therefore during the time dt the change of length element $\vec{\delta l}$ is

$$\frac{d}{dt}\vec{\delta l} = (\vec{\delta l}\vec{\nabla})\vec{v}. \tag{3.37}$$

We see that the time developments of vectors $\vec{B}/\rho$ and $\vec{\delta l}$ are given by the same equation. From this follows that if at the initial moment these two vectors are parallel, then they will remain parallel in future and their lengths will change proportionally. In other words, if two infitesimally close particles of plasma are on one field-line, then they remain on same field-line and the quantity B/ρ changes proportionally to change of distance between these two particles.

As mentioned in (1.1) the magnetic field formed by pulsar is at large distances dominated by its polar component $\vec{B} = B\vec{e}_\phi$. Using the fact that the polar length element $\vec{\delta l} = \delta l \vec{e}_\phi$ scales linearly with respect to a radial distance from the pulsar we have

$$\frac{B}{\rho} \propto \delta l \propto r$$

This gives

$$\frac{B}{\rho r} = {\rm const.} \tag{3.38}$$

Now, using the dependance of the pulsar's density[9] $\rho \propto r^{-2}$ we finally arrive at the condition

$$rB = {\rm const.} \tag{3.39}$$

In the investigated binary we encounter the following two cases:

---

[6] Note that all quantities are taken at the position of the shock.

[7] At the moment there is no theory explaining the conversion of plasma kinetic energy into the energy of electromagnetic field, therefore the value of σ cannot be calculated theoretically. $\sigma = 0.003$ is the "best-fit" solution satisfying the parameters of Crab Nebula pulsar (Kennel & Coroniti, 1984b).

[8] It is also important to mention that radiation can be produced far away from shock (as it takes place for X-ray band in Crab Nebula) where the magnetic field increases proportionally to distance, since the plasma density is constant in postshock region.

[9] Holds for the case of radial outflow with constant velocity.

1. For the whole orbit except for the passage of the pulsar crossing the disc, the Be-star outflow wind is dominated by its polar component (1.8) and its velocity is terminal v_∞, i.e. constant. Therefore comparing the wind pressures we get

   $$r_\mathrm{s} \propto R_\mathrm{s} = d\left(1 - \frac{r_\mathrm{s}}{d}\right) \tag{3.40}$$

   and for the shock in close vicinity to the pulsar ($r_\mathrm{s} \ll d$)

   $$r_\mathrm{s} \propto d \quad \rightarrow \quad dB = \mathrm{const.} \tag{3.41}$$

   Denoting by B_per the magnetic field at shock at a periastron we have

   $$B = B_\mathrm{per}\frac{d_\mathrm{per}}{d} \approx \frac{B_\mathrm{per,G}}{d_\mathrm{13,cm}}\,\mathrm{G} \tag{3.42}$$

   with $B_\mathrm{per,G}$ the magnetic field at the periastron in Gauss and $d_\mathrm{13,cm}$ the pulsar-star separation in 10^{13} cm.

2. For the passages when the pulsar is crossing the disc, the Be-star outflow wind is dominated by its equatorial component (1.5). Comparison of the wind pressures gives

   $$r_\mathrm{s} \propto R_\mathrm{s}^{\frac{4-n}{2}} = d^{\frac{4-n}{2}}\left(1 - \frac{r_\mathrm{s}}{d}\right)^{\frac{4-n}{2}} \tag{3.43}$$

   and similarly for $r_\mathrm{s} \ll d$ we get

   $$d^{\frac{4-n}{2}}B = \mathrm{const} \tag{3.44}$$

   and

   $$B = B_\mathrm{per}\left(\frac{d_\mathrm{per}}{d}\right)^{\frac{4-n}{2}}. \tag{3.45}$$

   For a typical value of the outflow exponent $n = 3$

   $$B = B_\mathrm{per}\sqrt{\frac{d_\mathrm{per}}{d}} \approx \frac{B_\mathrm{per,G}}{d_\mathrm{13,cm}^{1/2}}\,\mathrm{G}, \tag{3.46}$$

   i.e. this region is characterized by a variation of the magnetic field slower than in (3.42).

3.5 Diffusive shock acceleration of electrons

In the binary system PSR B1259-63 the proposed mechanism of acceleration of electrons to multi-TeV energies is acceleration on a shockwave.
One of the essential things we will need for the calculation of the formed electron spectrum behind the shockwave is the shape of the injection (accelerated spectrum of electrons).

In Fig.3.13 the mechanism of acceleration on the standing shock is schematically shown. The particles of the cold pulsar wind on the pulsar site (upstream region I in Fig.3.13) are moving towards the shock with Lorentz factor Γ. In the rest system of the pulsar wind, the electric field is zero, therefore the induced electric field in the laboratory frame is $c\vec{E} = -\vec{V} \times \vec{B}$ where $\vec{B}$ is the magnetic field in the upstream region (i.e. pulsar's regular magnetic field).

When an electron crosses the shock it starts to move in an irregular magnetic field in the downstream region (region II in Fig.3.13) and eventually if it crosses back into the upstream

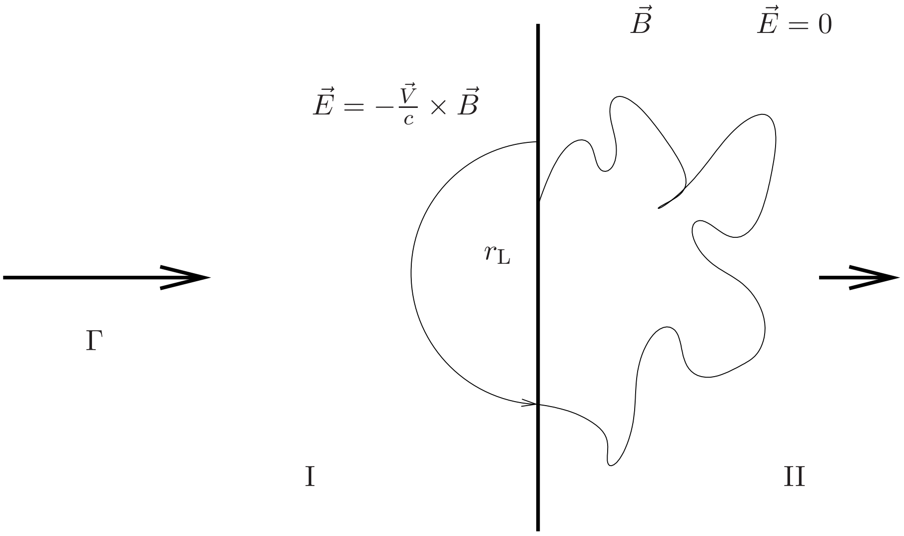

FIGURE 3.13: Acceleration at standing shock.

region, where it is accelerated by a nonzero electric field, it travels along a circular trajectory with the characteristic size of the electron's Larmor radius r_L.
The particles gain energy per each crossing, however only a fraction of them succeeds being accelerated to high energies due to a nonzero escape probability from the acceleration region. The accelerated spectrum of electrons is generally assumed to have power-law form[10]

$$q(\gamma)d\gamma \propto \gamma^{-\alpha}d\gamma. \tag{3.47}$$

The case of the acceleration on nonrelativistic shocks is analytically analyzed and the slope is known to have value $\alpha = 2$. There is still no satisfactory theory for the case of ultrarelativistic shocks. What seems clear from numerical simulations is that the power-law exponent is close to that of the nonrelativistic case[11] with a strongly anisotropic distribution.
Since the theoretical value of the coefficient α for relativistic shocks is not known and neither is the structure of anisotropicity we will assume the accelerated spectrum in form of power-law

$$q(\gamma, t) = A\gamma^{-2}e^{-\gamma/\gamma_{\max}}. \tag{3.48}$$

Kirk et al. (1999) estimated the value of the maximum electron energy $E_{\mathrm{e,max}}$ from upper limits of X-ray observations using (2.27) to be of the order $\sim$ 10TeV. Except for the section 4.3 we will use this value in our calculations. It is clear that due to the thermalization of the cold pulsar wind on the shockwave, the value of the low energy cutoff must be smaller than the energy of nonthermalized electrons in the pulsar wind. The Lorentz factor of the pulsar wind is not well constrained[12] ($\Gamma_0 \sim 10^4 - 10^6$), and we will use the value of low energy cutoff[13] of 1 GeV .
The coefficient A in general varies during pulsar orbit and so does the maximum energy of acceleration $\gamma_{\max} = E_{\mathrm{e,max}}/mc^2$, which is given by a balance of acceleration and cooling times of the electrons. The questions related to the orbital dependance of these two parameters

---

[10] Here I merely quote results from shock acceleration theory, since detailed mathematical analysis of this problem is not a subject of this work.

[11] Bednarz & Ostrowski (1998) - $\alpha \approx 2.2$, Achterberg et al. (2001) - $\alpha \approx 2.23$.

[12] For PSR B1259-63 it is $\leq 10^6$ - see section 4.4

[13] Note that this assumption does not have any effect on VHE emission (i.e. the incoming electron must have higher energy than produced VHE photon).

will be discussed later.
Knowledge of the features of radiation mechanisms and geometrical parameters of the system investigated in this and previous chapters allows us to move onto the calculations of the VHE emission.

Chapter 4

Gamma and X-rays from binary PSR B1259-63/SS 2883

This chapter will present calculations of VHE emission from the investigated binary pulsar in framework of IC scattering model.

The features of radiation processes and geometry of the system were already analyzed, therefore in order to calculate the energy spectra of radiation we must first determine the spectra of formed electrons. The latter vary for various assumptions concerning possible physical processes taking place in system.

At the beginning we will calculate the radiation from spectra of electrons formed behind the shockwave. First, we will analyze a simple calorimetric model, in which *all* energy lost by electron during its motion in the post-shock region is converted to the radiation. We will see that this basic model cannot explain variability of the observed TeV emission. As a way out, we propose two physical models able to explain the experimental data. One of them assumes formation of electron spectra due to dominant mechanisms of "invisible"[1] electron losses varying on orbit, the other assumes variable electron maximum energy resulting from the balance of electron acceleration and cooling times.

Aditionally, we will calculate the energy spectra of radiation from the cold ultrarelativistic pulsar wind expanding in the pre-shock region. We will see that while the effect of compton decceleration cannot explain variability of the emission, the formed energy spectra of radiation have line-type shape, which puts some constraints on initial Lorentz factor of pulsar wind.

4.1 Basic model

Spectrum of electrons.

When accelerated and isotropised on the shockwave, the electrons simultaneously lose their energy via the processes of radiation, expansion and escape. The corresponding spectrum formation equation is (Ginzburg & Syrovatskii, 1964)

$$\frac{\partial n_{\mathrm{e}}}{\partial t} + \frac{\partial(\dot{\gamma} n_{\mathrm{e}})}{\partial \gamma} = q(\gamma, t) - \frac{n_{\mathrm{e}}}{T_{\mathrm{esc}}} \tag{4.1}$$

---

[1] escape and adiabatic expansion of electrons

with $n_e(\gamma, t)$ - number of electrons per energy (in units of $m_e c^2$) interval, $\dot{\gamma}$ - electron energy losses, $T_{\rm esc}$ - electron escape time and $q(\gamma, t)$ - accelerated spectrum of electrons.

Eq.(4.1) is written under an assumption of continuous IC losses and validity of such an approach was shown in (Khangulyan & Aharonian, 2005). From Fig.4.1 one sees that the effect of the fractional electron energy losses becomes significant for the energies above 2 TeV. However, since the calculations in Fig.4.1 were performed under an assumption of zero synchrotron losses and in our case the latter dominate in energy range above ~ 1 TeV, the use of continuous losses approach is justified.

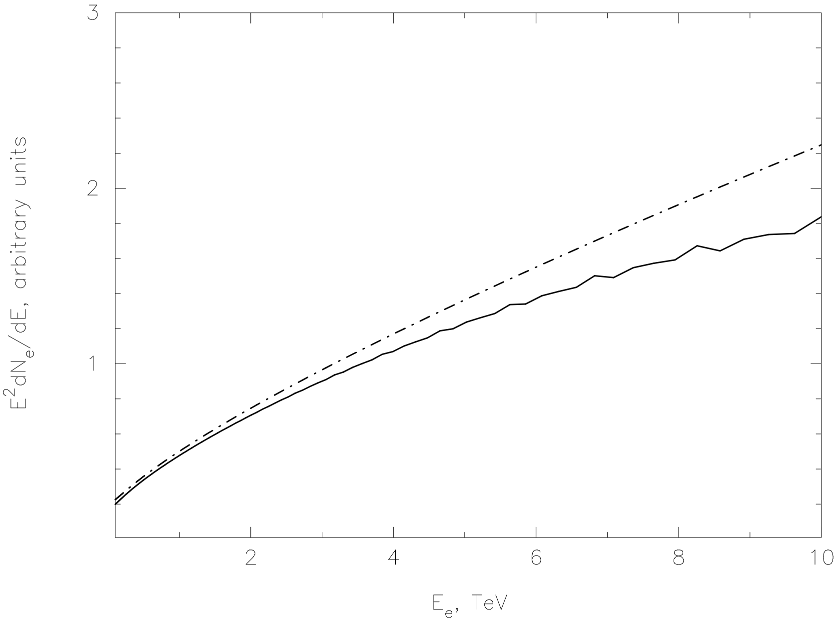

FIGURE 4.1: The steady state electron distribution function obtained within continuous loss approximation (dashed line) and from the exact solution of the Boltzmann equation (solid line). The temperature of blackbody radiation is assumed to be $T = 2.3 \cdot 10^4$K and the injection spectrum of electrons is assumed to be $q(\gamma) \propto \gamma^{-2}$. The plot is taken from (Khangulyan & Aharonian, 2005).

The solution of (4.1) is (B.22)

$$n_e(\gamma, t) = \frac{1}{|\dot{\gamma}|} \int\limits_{\gamma}^{\gamma_{\rm eff}} q(\gamma', t - \tau(\gamma, \gamma')) e^{-\tau(\gamma,\gamma')/T_{\rm esc}} d\gamma' \tag{4.2}$$

with cooling time of electrons from γ' to γ

$$\tau(\gamma, \gamma') = \int\limits_{\gamma}^{\gamma'} \frac{d\gamma''}{|\dot{\gamma}''|} \tag{4.3}$$

and the effective energy $\gamma_{\rm eff}$ given by

$$t = \int\limits_{\gamma}^{\gamma_{\rm eff}} \frac{d\gamma'}{|\dot{\gamma}'|}. \tag{4.4}$$

For the adiabatic change of the injection (acceleration rate) $q(\gamma', t-\tau(\gamma,\gamma'))$ can be replaced with $q(\gamma')$.

Let us consider the simpliest model with no escape and dominant radiative losses. In this case all energy lost by the electrons is converted into radiation and (4.20) is (B.15)

$$n_{\mathrm{e}}(\gamma, t) = \frac{1}{|\dot{\gamma}|} \int\limits_{\gamma}^{\gamma_{\mathrm{eff}}} q(\gamma') d\gamma'. \tag{4.5}$$

The accelerated spectrum was taken from Eq.(3.48), where normalization A can be obtained from pulsar spindown luminosity[2]

$$f \frac{L}{m_{\mathrm{e}} c^2} = \int\limits_{\gamma_{\mathrm{min}}}^{\gamma_{\mathrm{max}}} \gamma q(\gamma) d\gamma \quad \rightarrow \quad A = f \frac{L}{m_{\mathrm{e}} c^2 \ln \frac{\gamma_{\mathrm{max}}}{\gamma_{\mathrm{min}}}} \tag{4.6}$$

where f is the fraction of spindown luminosity converted into the ultrarelativistic electrons present in interaction. Unless mentioned otherwise f was taken to be $f = 0.1$ and $E_{\mathrm{e,min}} = 1\,\mathrm{GeV}$, $E_{\mathrm{e,max}} = 10\,\mathrm{TeV}$.

Radiative and ionization energy losses of electrons in the periastron are shown in Fig.4.2. The density of scatterers for the ionization and bremsstrahlung losses can be estimated by taking the observed value of the column density of the hydrogen atoms, and dividing it by the characteristic size of the region.

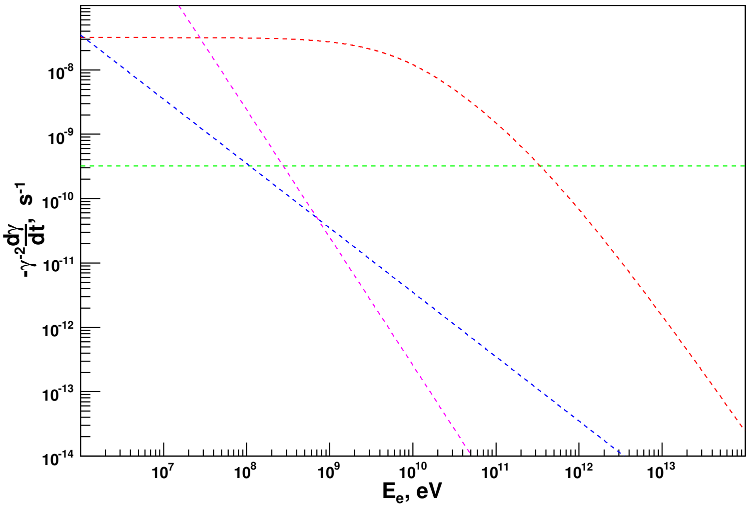

FIGURE 4.2: Radiative and ionization losses of electrons for the energy range 1 GeV – 100 TeV at periastron. The lines represent different energy loss processes as follows: red - inverse compton, green - synchrotron, violet - ionization, blue - bremsstrahlung. The magnetic field is B=0.5G, the density of atoms in ionization and bremsstrahlung processes $n = 10^8\,\mathrm{cm}^{-3}$.

Taking $N_{\mathrm{H}} \sim 6.10^{21}\,\mathrm{cm}^{-2}$ from (Tavani & Arons, 1997) and dividing it with the periastron separation we obtain

$$n_{\mathrm{H,max}} \sim \frac{N_{\mathrm{H}}}{d_{\mathrm{per}}} \sim 10^8\,\mathrm{cm}^{-3} \tag{4.7}$$

---

[2] for simplicity in derivation of A the exponential cutoff in Eq.(3.48) was replaced by sharp cutoff at γ_{max}

To estimate, which formula (for non-ionized or fully ionized gas) of ionization losses to use, we need to estimate the photon number density of blackbody star above the effective ionization energy of hydrogen. This is

$$n_{\rm tot}(\epsilon > I) = \int\limits_I^\infty n(\epsilon) d\epsilon \quad , \quad n(\epsilon) \simeq \left(\frac{R_*}{2d_{\rm per}}\right)^2 n_{\rm ph}(\epsilon) \quad , \quad n_{\rm ph}(\epsilon) = \frac{1}{\pi^2 \hbar^3 c^3} \frac{\epsilon^2}{e^{\epsilon/kT} - 1} \tag{4.8}$$

the maximum of SS 2883 blackbody spectrum is at $\epsilon_{\rm max} = 2.822\, kT = 5.5\,{\rm eV}$, and since $I \simeq 15\,{\rm eV}$ this integral can be evaluated analytically

$$n_{\rm ph}(\epsilon > I) \approx \left(\frac{R_*}{2d_{\rm per}}\right)^2 \frac{1}{\pi^2 \hbar^3 c^3} \int\limits_I^\infty \epsilon^2 e^{-\epsilon/kT} d\epsilon \simeq 2.10^{11} {\rm cm}^{-3} \tag{4.9}$$

which significantly exceeds the hydrogen density inferred from the observations, therefore we consider the gas to be fully ionized - formula (2.47).
From Fig.4.2 one can see that synchrotron and inverse compton losses dominate over whole assumed acceleration spectrum range, therefore only these two will be taken into account in the following. In order for the bremsstrahlung and ionization losses to be comparable with inverse compton or synchrotron losses, the density of hydrogen atoms must be 3 orders of magnitude higher than estimated in Eq.(4.7).

Due to the orbital magnetic field dependance $B \sim d^{-1}$ (frozen-in condition, see section 3.4) and Be-star soft photon spectrum dependance $n(\epsilon) \sim d^{-2}$ where d is pulsar-star separation distance, the radiative losses vary on the orbital position $t_{\rm orb}$ as (Fig.4.3)

$$\dot{\gamma}_{\rm rad}(t_{\rm orb}) = \left(\frac{d_{\rm per}}{d(t_{\rm orb})}\right)^2 \dot{\gamma}_{\rm rad,per}, \tag{4.10}$$

where index *per* refers to values in periastron.

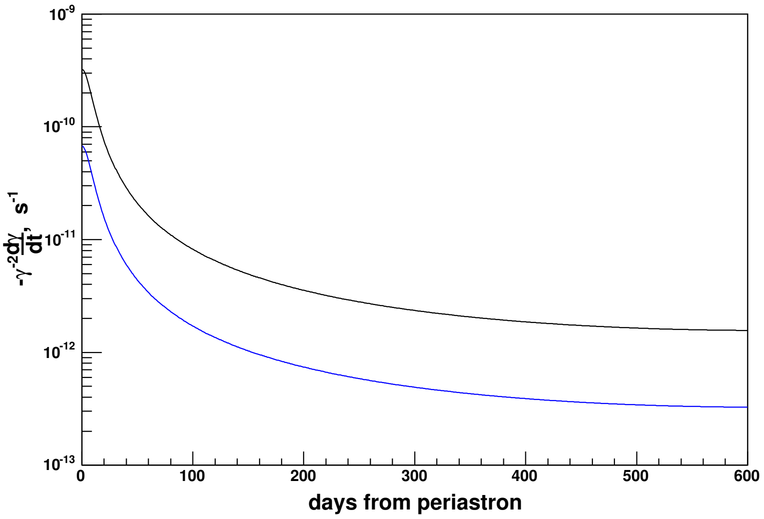

FIGURE 4.3: Light curve for the electron energy losses at energy 1 TeV. Black line represents synchrotron losses, blue line IC losses. Magnetic field at periastron is set to 0.5 G.

Let us return to the question of $\gamma_{\rm eff}$ given by Eq.(4.4). It is interesting to calculate the total cooling time (i.e. from $\gamma_{\rm max}$ to $\gamma_{\rm min}$) dependance on the epoch to get the picture about the cooling timescales of the system in order to compare them with characteristic dynamical time of the system $\sim 1\,\mathrm{day}$. This dependance is shown in Fig.4.4 - one sees that due to the inverse square dependance of energy losses on distance, the total cooling time increases significantly towards apastron.

The differential equation for evolution of γ_{eff} can be evaluated by differentiation of (4.4) using the assumption of fixed cooling time equal to dynamic time of the system. This gives

$$\frac{d\gamma_{\mathrm{eff}}}{|\dot{\gamma}(\gamma_{\mathrm{eff}})|} = \frac{d\gamma}{|\dot{\gamma}(\gamma)|} \tag{4.11}$$

with an initial condition for $\gamma_0 = \gamma_{\mathrm{min}}$ and $\gamma_{\mathrm{eff},0}$

$$t_{\mathrm{dyn}} = \int\limits_{\gamma_{\mathrm{min}}}^{\gamma_{\mathrm{eff},0}} \frac{d\gamma'}{|\dot{\gamma}'|}. \tag{4.12}$$

Fig.4.5 shows the dependance $E_{\mathrm{eff}} = E_{\mathrm{eff}}(E_{\mathrm{e}})$ for various days at the orbit. We see that close to the periastron (i.e. from -20 to 20 days around periastron) the electron distribution can be approximately written as

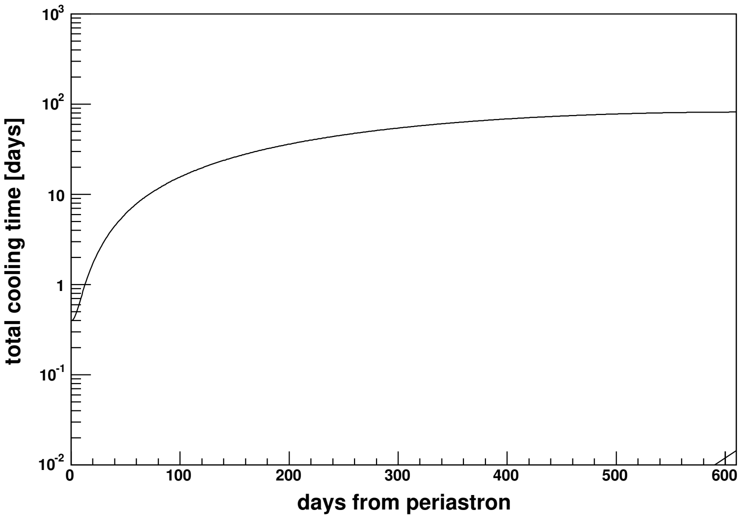

FIGURE 4.4: Total cooling time from γ_{max} to γ_{min} due to radiative losses as a function of epoch (day 0 corresponds to periastron). The magnetic field at periastron is chosen to be B=0.5G.

$$n_{\mathrm{e}}(\gamma, t) = \frac{1}{|\dot{\gamma}|} \int\limits_{\gamma}^{\gamma_{\mathrm{max}}} q(\gamma')d\gamma'. \tag{4.13}$$

The effect of weak radiative cooling becomes significant at the epochs close to apastron even for high energies.

Fig.4.6 shows the spectrum of electrons formed due to the radiative cooling at different epochs. As expected, the spectrum decreases towards periastron due to the stronger cooling. The break in spectra close to the apastron (best seen in Fig.4.6 for ±600 days around electron energy 2 TeV) occur due to the corresponding decrease of γ_{eff} values as seen in Fig.4.5.

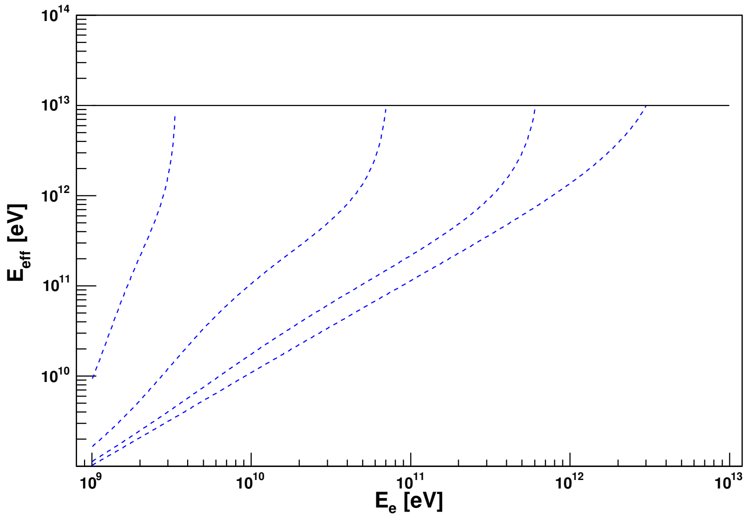

FIGURE 4.5: Dependance of the effective electron energy on the energy of electrons. Solid line represents maximum acceleration energy. Dashed lines correspond to different days at the orbit as following: from left to right - 20, 40, 100, 600 days . The magnetic field at periastron is chosen to be B = 0.5 G.

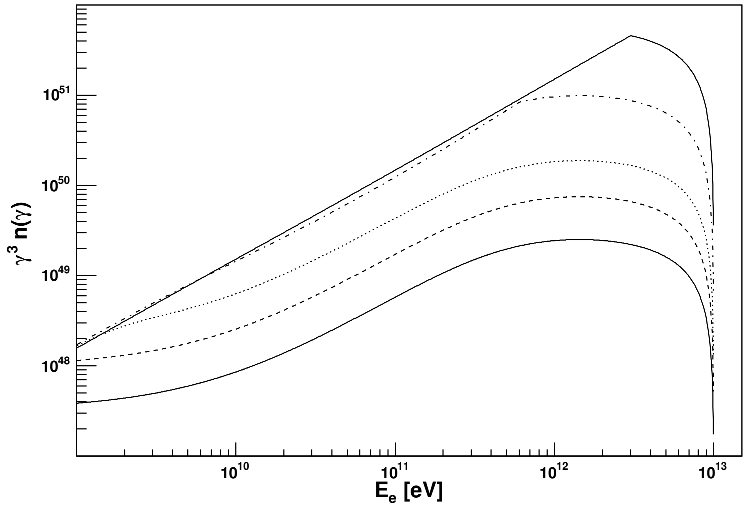

FIGURE 4.6: Spectrum of the electrons formed due to radiative losses only. Different lines represent different epochs as follows: low solid line - periastron, dashed line - ±15 days, dotted line - ±30 days, dashed-dotted line - ±100 days, top solid line - ±600 days.

Absorption in the binary pulsar PSR B1259-63/SS 2883

Before we proceed to the calculation of the radiation, it is necessary to determine the optical depth of the system given by (2.18).
Adopting the geometry from Fig.4.7 the absorption angle θ is

$$\sin\theta = \frac{d\sin\psi}{r} \quad , \quad r = \sqrt{d^2 + l^2 - 2ld\cos\psi} \tag{4.14}$$

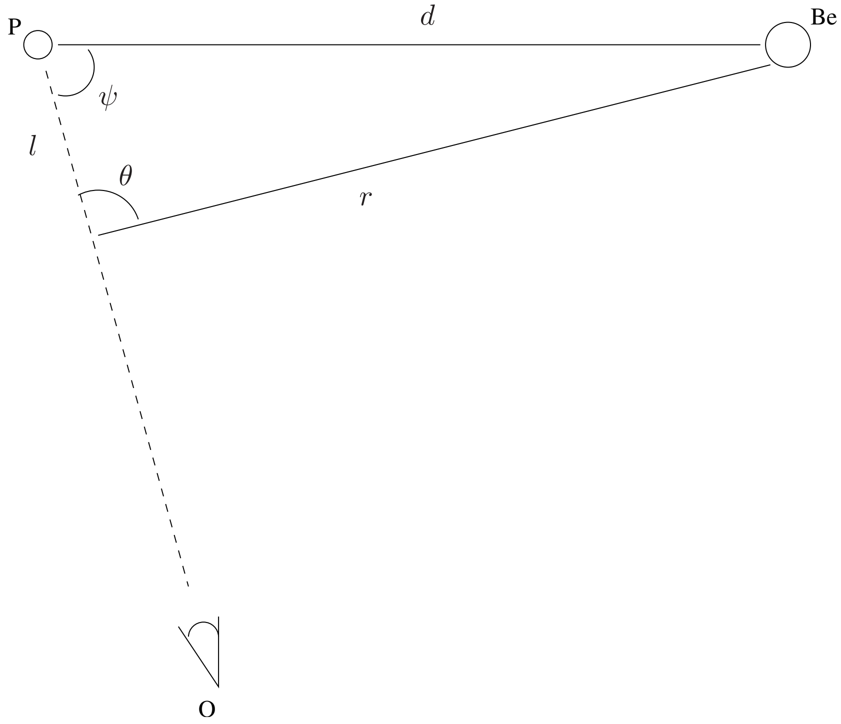

FIGURE 4.7: Absorption of gamma ray moving through anisotropic photon gas from SS 2883.

and consequently for the optical depth

$$\tau(E_\gamma) = \int\limits_0^D dl \frac{R_*^2}{4(d^2 + l^2 - 2ld\cos\psi)} \int\limits_{2/E_\gamma(1-\cos\theta)}^{\infty} d\epsilon\, n_{\rm ph}(\epsilon)\sigma(E_\gamma,\epsilon,\theta)(1-\cos\theta). \tag{4.15}$$

with $\sigma(E_\gamma, \epsilon, \theta)$ from (2.19).
The calculated optical depth for the photon energy $E_\gamma = 1\,\mathrm{TeV}$ is shown in Fig.4.8. The soft photon density increases simultanously towards the periastron and for the small values of angle ψ, therefore as expected (see Fig.3.3) the maximum of absorption occurs few days before periastron.
The amplitude of the absorption is relatively small ($< 1\%$ for whole orbit except for few days before periastron where it is $\sim 10\%$), hence we will approximate system to be **transparent** (optically thin) for VHE gamma-rays.

Energy spectra of radiation

According to the definition of used inverse compton cross-section (2.2,2.4) the number of scatterings per unit of an incoming solid angle for the scattering of *isotropically*[3] distributed electrons with spectrum $n_{\rm e}(\gamma)$ on a photon field $n(\epsilon)$ is given as

$$\frac{dN}{dt\, dE_\gamma d\Omega} = \frac{c}{4\pi} \int d\gamma n_{\rm e}(\gamma) \int d\epsilon\, n(\epsilon)(1-\cos\theta) \frac{d\sigma}{dE_\gamma d\Omega}(\epsilon,\gamma,E_\gamma,\theta) \tag{4.16}$$

where

$$\frac{d\sigma}{dE_\gamma d\Omega}(\epsilon,\gamma,E_\gamma,\theta) \tag{4.17}$$

---

[3] factor $1/4\pi$ in 4.16 results from this fact

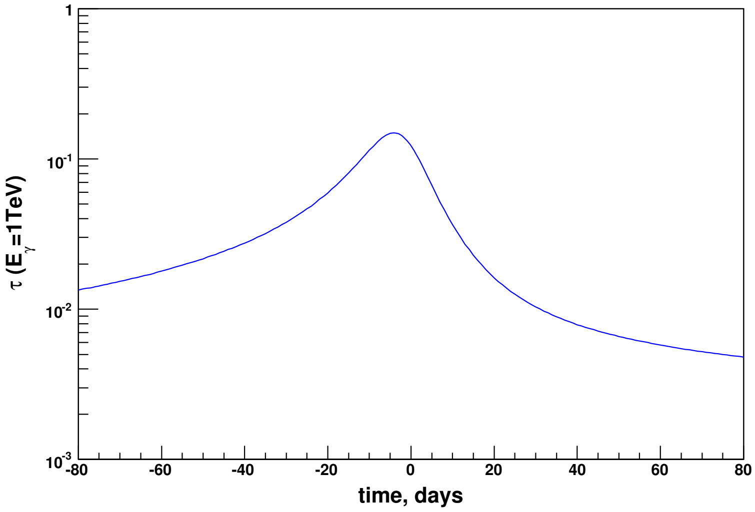

FIGURE 4.8: Optical depth for various days on the orbit for photon energy $E_\gamma = 1\,\text{TeV}$.

is the differential cross-section of the Inverse Compton scattering of an electron with energy γ and a photon of energy ϵ under angle θ producing photon of energy E_γ (all energies are in units of $\mathrm{m_e c^2}$).
The solid angle corresponding to an area of detector dS at distance from the source D is $d\Omega = dS/D^2$, therefore for the irradiated spectrum per unit of the detector area we have

$$\frac{dN}{dS\,dt\,dE_\gamma} = \frac{c}{4\pi D^2}\int d\gamma n_{\mathrm{e}}(\gamma)\int d\epsilon\, n(\epsilon)\frac{d\sigma}{dE_\gamma d\Omega}(\epsilon,\gamma,E_\gamma,\theta)(1-\cos\theta) \tag{4.18}$$

The electron spectrum orbital dependance comes from the orbital dependance of energy losses in (4.5). Since the Be-star photon spectrum is given by (4.8), the dependance on pulsar-star separation d cancels in (4.18) and consequently

the orbital dependance of IC radiation comes only from the anisotropy of IC scattering[4].

Fig.4.9 shows a comparison of calculated lightcurve with the observed HESS data.

In order to explain the levels of radiation, the value of magnetic field at periastron was chosen to be $B = 0.5$G. The theoretical curve agrees well with previous calculations done by Kirk et al. (1999).
One can see that the lightcurve calculated in this model implies almost constant flux over the entire orbital period and therefore is in conflict with observations, which show noticeable reduction of the flux towards the periastron. Since the variation of magnetic field periastron value can produce only change of an overall amplitude of the radiation, in order to be able to explain the observed data one can introduce the additional "invisible" losses, which vary on the orbit.

---

[4] the effect of γ_{eff} on electron spectrum becomes significant close to the apastron and for higher energies is unimportant which can be seen from Fig.4.6

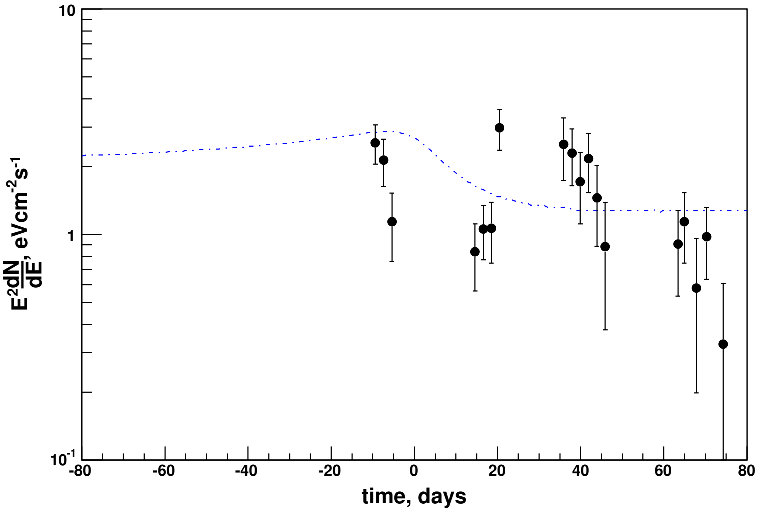

FIGURE 4.9: Calculated lightcurve in comparison with HESS data around periastron.

4.2 Adiabatic losses and escape of electrons.

In the previous section we considered only the radiative losses, and neglected the "invisible"(adiabatic losses and escape) energy losses of electrons. However, the interaction of pulsar wind with the ambient medium results in a complex wave structure where the adiabatic and escape losses may play a dominant role. Both adiabatic and escape timescales can not be calculated from the first principles given the complexity of the system. Instead, characteristic timescales of nonradiative losses can be derived phenomenologically, namely from the observed gamma-ray lightcurve.
In order to do it one must take into account that the adiabatic losses are symmetric around periastron (the mechanism of adiabatic losses is analyzed in detail in next chapter), i.e. their characteristic cooling time behaves as $t \sim R/v$ where R is the characteristic size of an expanding region and v the expansion velocity. Assuming that the adiabatic losses dominate over entire spectrum range of electrons we can fit the value of the adiabatic coefficient by comparing the calculated flux for isotropic case with observed data.

The reported TeV gamma-ray observations are quite sparse and unfortunately allow a broad range of lightcurves.
In Fig.4.10 we show an example of a lightcurve which matches the HESS data.The time-profile of the rate of nonradiative losses derived from that lightcurve with additional assumption that 10% of pulsar spindown luminosity is converted into relativistic electrons with constant (for all epochs) injection rate and energy spectrum given by Eq.(3.48) with $E_{\rm e,max} = 10$ TeV is shown in Fig.4.11. The magnetic field dependance is assumed to be $B \propto d^{-1}$ with $B = 0.1\,$G at periastron. From the plot we can see that in order to match the lightcurve in Fig.4.10 one needs very sharp increase of adiabatic losses with characteristic cooling time $t_{\rm ad} \sim 100\,$sec at periastron. This can be naturally related to a much smaller size of the emission region in periastron, i.e. the region occupied by relativistic electrons accelerated by the termination shock in dense region closer to the star. In the case of termination of the wind in the highest density environment which coincides with the passage of the pulsar through the stellar disk we would expect even higher nonradiative losses, so one should expect some deviation from the adopted smooth symmetric profile of adiabatic losses shown in Fig.4.11. Interestingly,

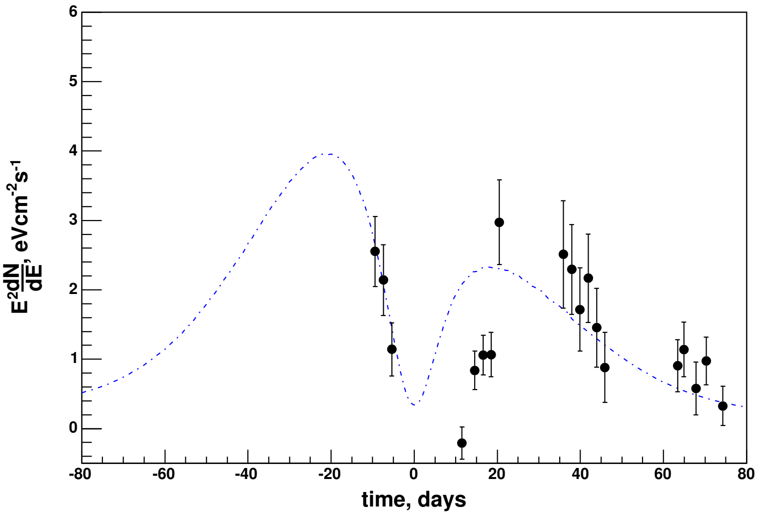

FIGURE 4.10: The lightcurve of 1 TeV gamma-rays detected by HESS from PSR B1259-63/SS2883. A reference lightcurve adopted for derivation of the time profile of nonradiative energy losses of electrons is also shown. The somewhat lower flux of gamma-rays at $t \sim 15$ days after the periastron can be associated with the enhanced losses in the disk, and thus may cause more irregular profile of energy losses.

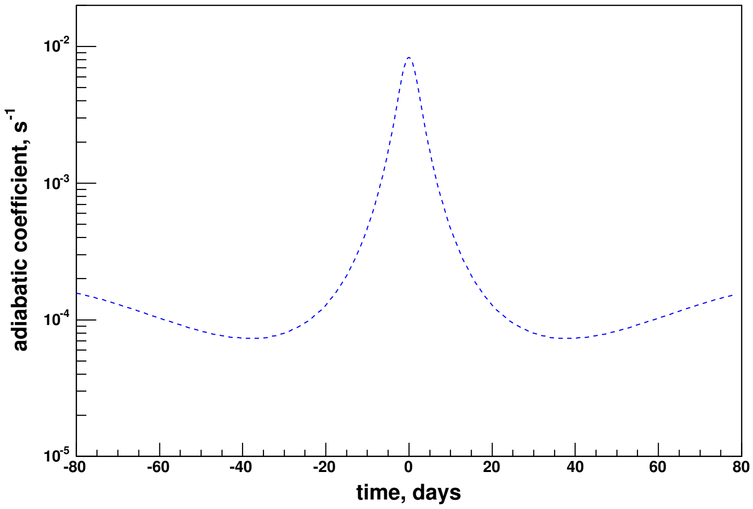

FIGURE 4.11: The reconstructed time profile of adiabatic energy loss rate derived for the reference TeV lightcurve shown in Fig.4.10

the lower, by a factor of two, flux of TeV gamma-rays was observed at $t = 20$ days from periastron, which coincides with the interaction point of the pulsar wind with the disk, and formally we can always interprete this anomaly as a result of the enhanced nonradiative losses in the disk. However, the large statistical and systematic errors of TeV fluxes do not allow certain conclusions in this regard. Therefore the reference lightcurve in Fig.4.10 should be treated as a reasonable approximation for derivation of basic parameters of the system.
At epochs far from periastron the rate of the required nonradiative losses drops significantly, however it still remains faster than IC and synchrotron losses with characteristic time $t \sim 10^4$ sec (see Fig.4.13).

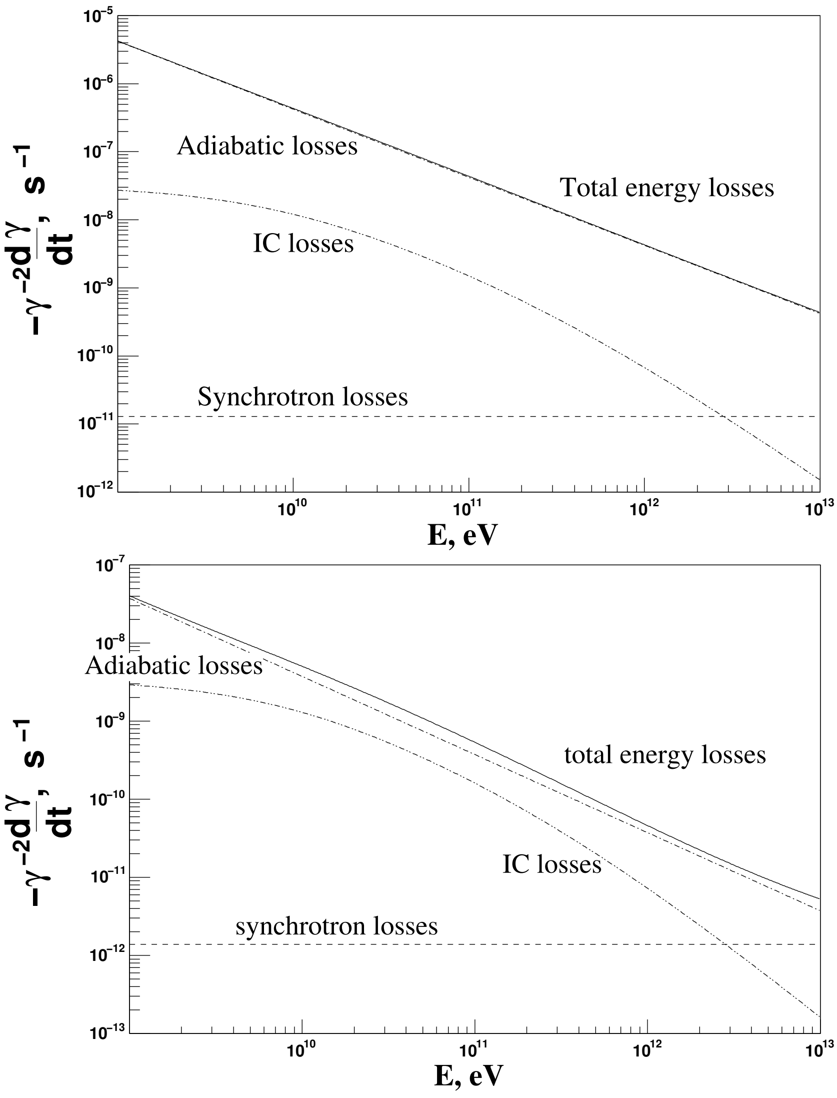

FIGURE 4.12: The energy loss rates calculated for two epochs: at periastron (top panel) and at $t = 35$ days from periastron (bottom panel). The assumed parameters are the same as in Fig.4.13.

Note that the curves in Fig.4.13 correspond to electrons of energy 1 TeV. However, as it is seen from Fig.4.12, nonradiative losses dominate over radiative losses at all relevant energies of electrons and during the entire orbit of the pulsar. Spectra of electrons for various epochs calculated with inclusion of phenomenologically derived adiabatic losses profile are shown in Fig.4.14. Compared with previous model (Fig.4.6) spectra are damped at periastron and due to enhanced losses the cuts due to $\gamma_{\rm eff}$ dissapear, i.e. $\gamma_{\rm eff} = \gamma_{\rm max}$.

In Fig.4.15 we show lightcurves calculated for four different energies of gamma-rays. The lightcurve for 1 TeV coincides, by definition, with the reference lightcurve shown in Fig.4.10. The lightcurves at different energies have similar shape what is explained by the dominance of adiabatic losses at all energies of electrons. At the same time the energy spectra of IC radiation at different energy bands are significantly different. Indeed, the dominance of adiabatic or energy-independent escape losses maintains the acceleration spectrum of electrons unchanged[5]. Thus at energies $E \ll E_{\rm max}$, the gamma-rays produced in the Thompson regime ($E_\gamma \leq 10$ GeV) will have power-law spectrum with photon index $(\alpha + 1)/2$, while in

---

[5] since $n_{\rm e} \propto \frac{1}{\gamma}\int q(\gamma)d\gamma$, for adiabatic losses $n_{\rm e} \propto \frac{1}{\gamma}\int \gamma^{-\alpha}d\gamma \propto \gamma^{-\alpha}$.

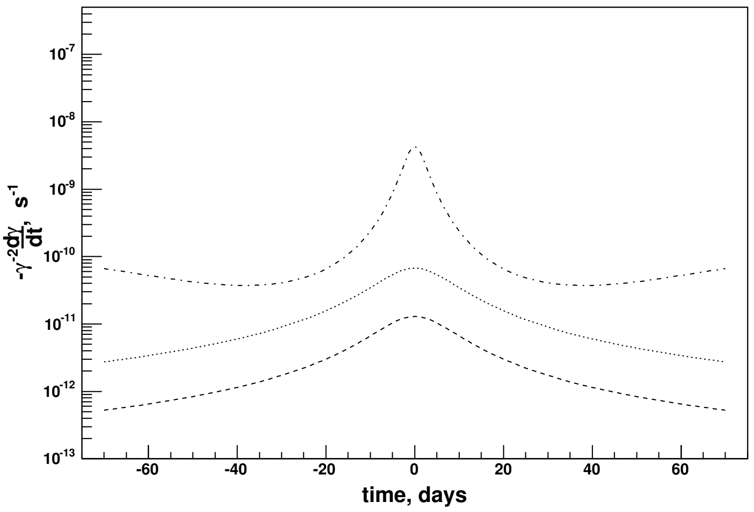

FIGURE 4.13: The energy losses of electrons for 1 TeV versus epoch. Dashed line represents synchrotron losses, dotted line - IC losses, dashed-dotted line - reconstructed adiabatic losses.

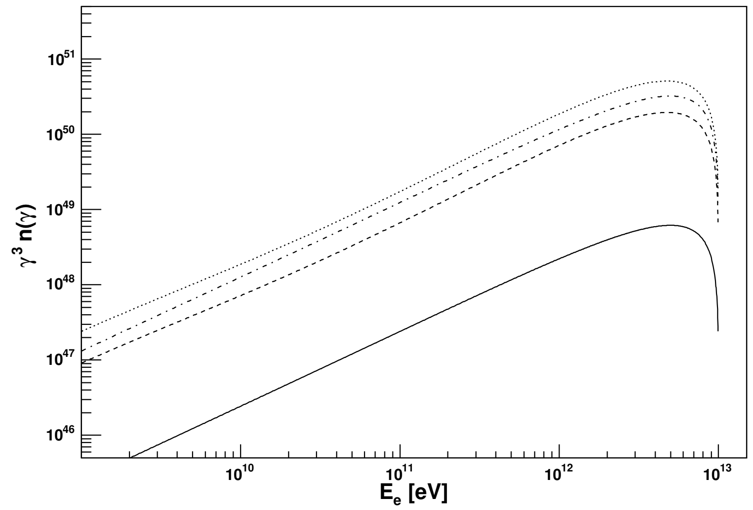

FIGURE 4.14: Electron spectrum for different epochs for adiabatic losses dominated scenario.Different lines represent different epochs as follows: low solid line - periastron, dashed line - ±15 days, dotted line - ±30 days, dashed-dotted line - ±80 days. Magnetic field at the periastron is 0.1 G.

the deep Klein-Nishina regime the spectrum will be proportional to $E_\gamma^{-(\alpha+1)} \ln E_\gamma$ (Blumenthal & Gould, 1970) (in our case $\alpha = 2$). This effect is seen in Fig.4.16, where we show the broadband spectral energy distribution (SED) of radiation at different epochs, consisting of synchrotron and IC components.

In Fig.4.17 we also show the gamma-ray spectra averaged over three periods of HESS observations in February, March and April 2004. Within the statistical and systematic uncertainties, the agreement with the fluxes reported by HESS is satisfactory (Aharonian et al., 2005).

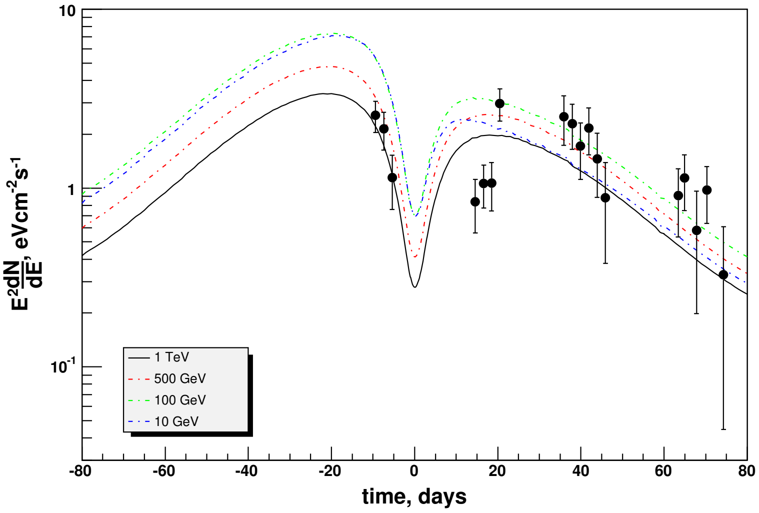

FIGURE 4.15: Gamma ray - ligthcurves in adiabatic losses dominted scenario calculated for different energies. Black line represents reference lightcurve for 1 TeV, red - 0.5 TeV, green - 0.1 TeV, blue - 10 GeV.

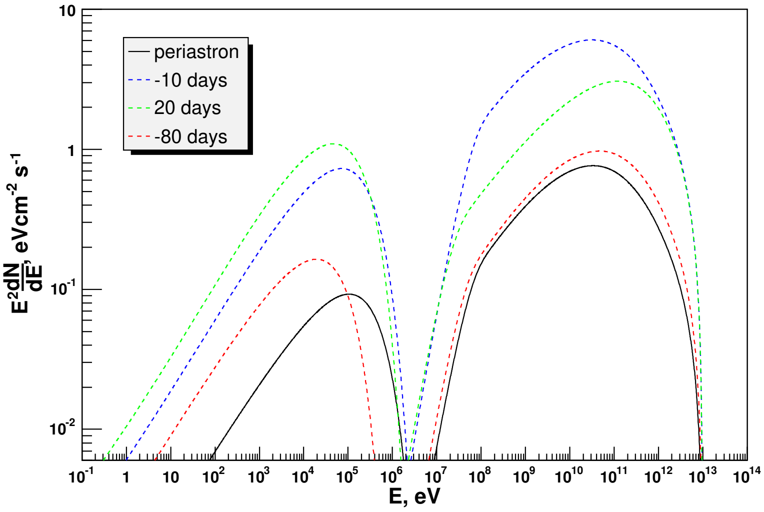

FIGURE 4.16: Broadband spectral energy distribution of synchrotron and IC components of radiation in adiabatic loss dominated scenario. The spectra correspond to times −80 days - red-dashed line, −10 days - blue-dashed line, 20 days - green-dashed line, periastron - black solid line.

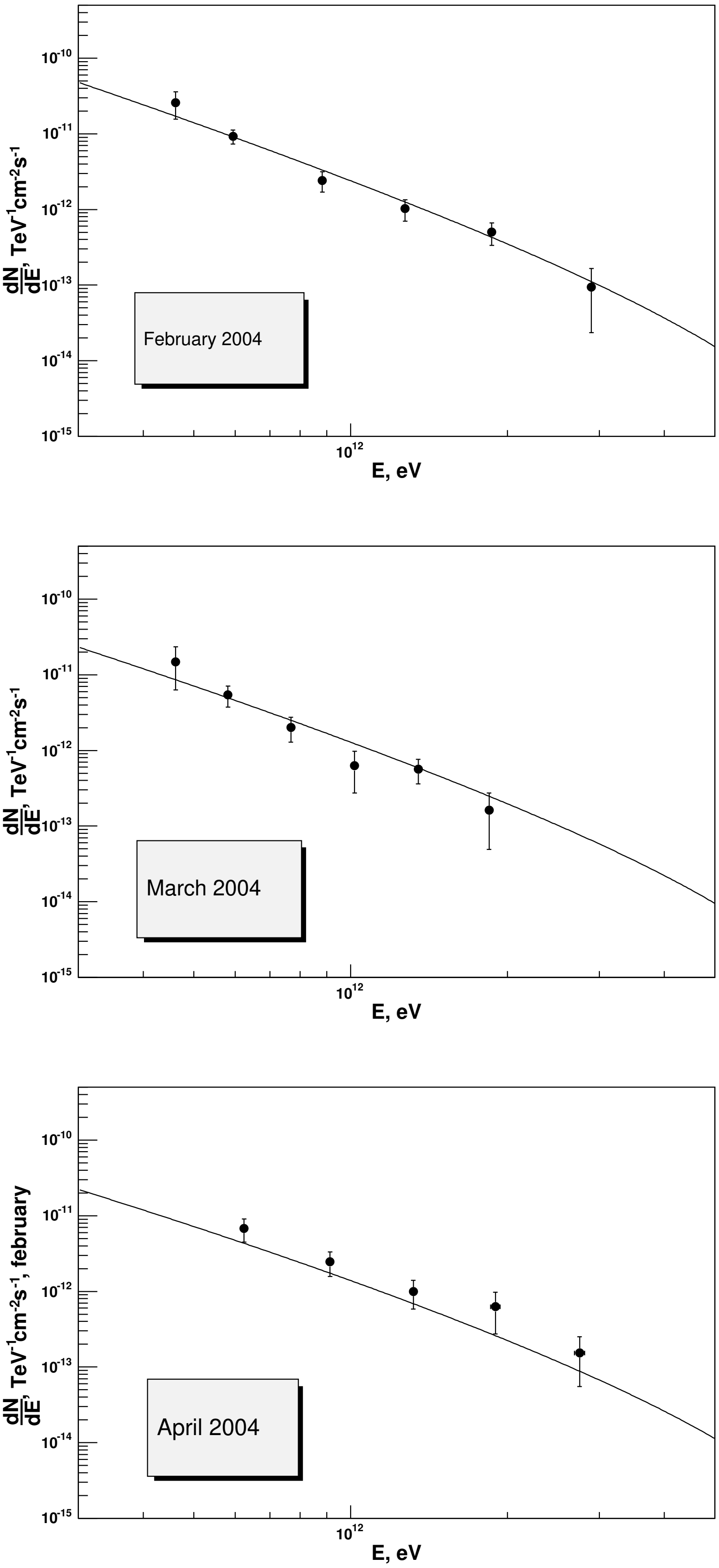

FIGURE 4.17: The time-averaged (over the HESS observation periods) TeV gamma-ray spectrum shown together with HESS measurements in February, March and April 2004.

For the adopted key parameters, in particular for the electron adiabatic loss rates shown in figures 4.12 - 4.13, the gamma-ray fluxes are not sensitive to the magnetic field strength as long as it does not exceed 0.5 G. On the other hand the synchrotron flux is very sensitive to magnetic field $\propto B^{(\alpha+1)/2} = B^{3/2}$ (Ginzburg & Syrovatskii, 1964). It is seen from Fig.4.16 that for the assumed magnetic field 0.1 G the fluxes of synchrotron X-rays are significantly below 10^{-11} erg/cm^{2}s, thus they cannot explain the X-ray data (Chernyakova et al., 2006). On the other hand, the magnetic field $B = 0.45$G at periastron raises the synchrotron X-ray flux to the observed level.

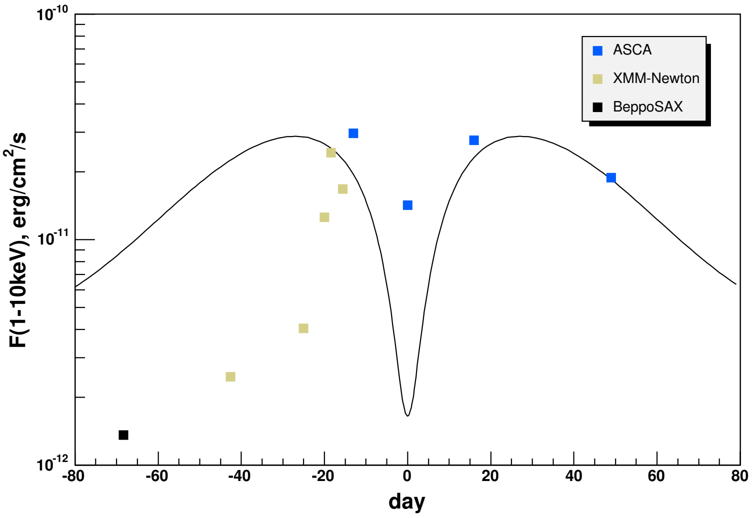

FIGURE 4.18: The X-ray lightcurve calculated for the adiabatic loss time-profile shown in Fig.4.11, and magnetic field strength $B = 0.45(d/d_{\rm per})^{-1}$ G. The blue point sets correspond to ASCA (Hirayama et al., 1996), brown points to XMM-Newton (Chernyakova et al., 2006) and black point to BeppoSAX (Chernyakova et al., 2006) observations, respectively.

The X-ray light curve, calculated for the B-field dependence $B = 0.45(d_{\rm per}/d)$ G, is shown Fig.4.18. While the calculated lightcurve is in reasonable agreement with observations around the periastron and at high separations (more than 200 days), it significantly exceeds the fluxes between 200 days to several days before the periastron (detailed calculation in Khangulyan et al. 2006). This implies that the magnetic field should be much weaker, and thus the the X-rays cannot be explained by synchrotron radiation. A more speculative explanation could be that, the energy release in nonthermal particles for this period is suppressed, e.g. due to the the interaction with the stellar outflow. Obviously, this effect will have a similar impact on the gamma-ray light curve, namely it should suppress significantly the gamma-ray fluxes. However the lack of gamma-ray data for this period do not allow any conclusion in this regard.

Escape of electrons

Escape of electrons from the emitting region represents another form of "invisible" losses.

The timescale of escape can be estimated from the size of interacting region and the speed of relativistic plasma

$$T_{\rm esc} \simeq \frac{D}{c/3} = \begin{cases} 10^3\,{\rm s}\,({\rm for\,periastron}) \\ 10^4\,{\rm s}\,({\rm for\,apastron}) \end{cases}, \tag{4.19}$$

which is comparable or shorter (depending on energy) than radiative cooling time of elec-

trons[6].
The solution of kinetic equation with escape term assuming adiabatic injection rate is

$$n_{\mathrm{e}}(\gamma,t)=\frac{1}{|\dot{\gamma}|}\int\limits_{\gamma}^{\gamma_{\mathrm{eff}}} q(\gamma')e^{-\tau(\gamma,\gamma')/T_{\mathrm{esc}}}d\gamma'. \tag{4.20}$$

Addition of constant escape time leads to decrease of electron spectrum, at epochs far from periastron, which can be seen when comparing Fig. 4.19 (escape included, radiative losses only) with Fig.4.6 (no escape, radiative losses only). Since the magnetic and photon field densities are decreasing when moving away from periastron, the particles cool slower, which naturally results in higher probability of escape.

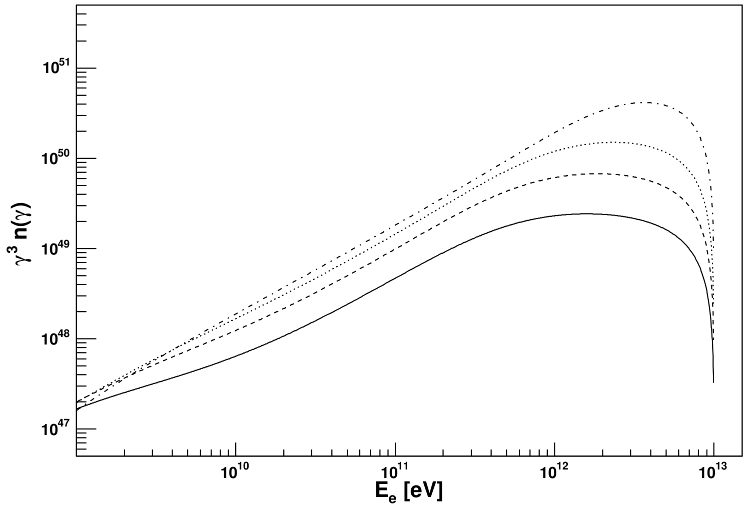

FIGURE 4.19: Spectrum of electrons with same model parameters as in Fig.4.6 with inclusion of escape of the electrons $T_{\mathrm{esc}}=5\cdot10^4$ s. Different lines represent different epochs as follows: low solid line - periastron, dashed line - ±15 days, dotted line - ±30 days, dashed-dotted line - ±80 days.

Consequently, when compared with basic model (section 4.1), this effect leads to damping of radiation levels at epochs $|t|>20$ days from periastron shown in Fig.4.20.
Summarizing, we see that while introduction of electron escape gives desired damping of radiation levels at epochs away from periastron, it cannot explain the significant decrease of radiation levels near periastron.

4.3 Maximum energy of electrons

Until now we did not consider the effects related to the acceleration of electrons - namely, the maximum energy of electrons is determined from the balance of particle acceleration and loss rates.

The acceleration is done by an electromagnetic force, therefore it is convenient to present the acceleration time of electrons in the following form:

$$t_{\mathrm{acc}}=\frac{\eta\, r_{\mathrm{L}}}{c}\approx 0.11\, E_{\mathrm{TeV}}\, B_{\mathrm{G}}^{-1}\,\eta\ \mathrm{s}\,, \tag{4.21}$$

---

[6] note that due to complexity of the system this timescale cannot be calculated.

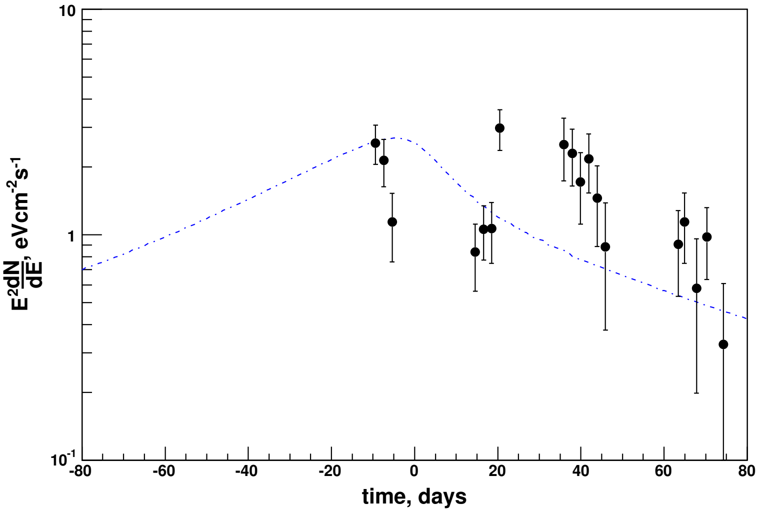

FIGURE 4.20: Calculated lightcurve for the calorimetric model, with inclusion of escape of the electrons. The escape time is assumed to be $5 \cdot 10^4$s

where $r_{\rm L} = Ev/ecB$ is electron larmor radius, η is a dimensionless constant; $\eta = 1$ corresponds to the maximum possible rate of acceleration allowed by classical electrodynamics. It is well known theoretically and proved during Sun observations, that in case of nonrelativistic parallel shocks, $\eta > (c/v)^2 \gg 1$. In reality η can exceed significantly 1 even in the case of relativistic shocks.

In Fig.4.21 we show characteristic acceleration times for 3 different values of $\eta = 4 \times 10^3,\ 10^3,\ 10^2$, together with synchrotron and Compton cooling timescales calculated for the epoch of the periastron assuming the magnetic field $B = 0.05\,$G. The energy-independent escape time, which was assumed to be 10^4 s, is also shown. The maximum energy of accelerated electrons is determined by the intersection of curves corresponding to the acceleration and loss times. Because of essentially different energy dependencies of characteristic energy loss times $t_{\rm syn}$, $t_{\rm IC}$ and $t_{\rm esc}$, the maximum energy of electrons is determined, depending on the value of η, by IC losses (a) or by synchrotron losses (c) or by escape (b) (see Fig.4.22).

If the energy losses of electrons dominate by synchrotron cooling in the magnetic field $B_{\rm G} = B/1\,$G with characteristic time

$$t_{\rm syn} \approx 400 B_{\rm G}^{-2} E_{\rm TeV}^{-1}\ {\rm s}\,, \tag{4.22}$$

the corresponding maximum energy of electrons is

$$E_{\rm e,max} \approx 2\, B_{\rm G}^{-1/2} \left(\frac{\eta}{10^3}\right)^{-1/2}\ {\rm TeV}\,. \tag{4.23}$$

Note that in the case of $\eta =$ const the maximum energy of synchrotron photons does not depend on the magnetic field ($E_{\rm syn,max} \propto E_{\rm e,max}^2\ B$=const), but depends on η, namely $E_{\rm syn,max} \sim 100(\eta/10^3)^{-1}\,$keV. This relation contains unique information about the acceleration rate through the η parameter.

In the regime when IC cooling dominates over the synchrotron cooling,

$$t_{\rm IC} \approx 7 \cdot 10^3 w_0^{-1}\ E_{\rm TeV}^{0.7}\ {\rm s}\,, \tag{4.24}$$

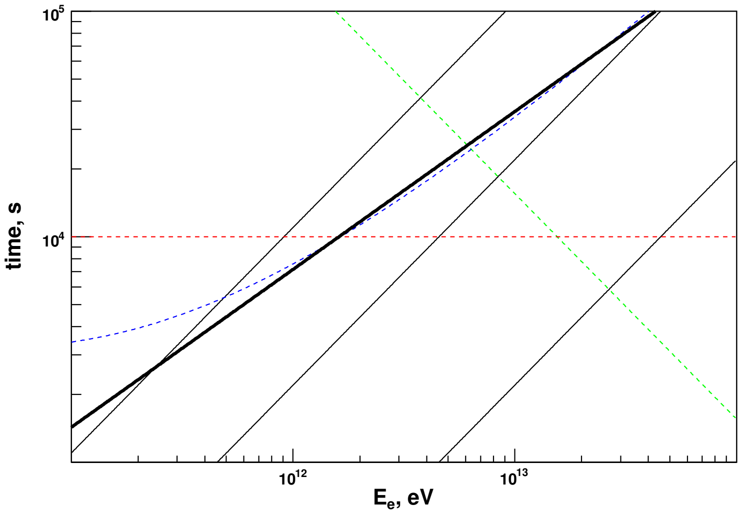

FIGURE 4.21: The acceleration and cooling times of electrons at the periastron. Blue-dashed line corresponds to the IC cooling time obtained with accurate numerical calculation; the thick solid line is the IC cooling time given by the Eq. (4.24); the green-dashed line corresponds to the synchrotron cooling time ($B = 0.05$ G); the red-dashed line is the escape time; black lines are acceleration times for $\eta = 5 \cdot 10^3$ (a),$\eta = 10^3$ (b),$\eta = 10^2$ (c).

where w_0 is the energy density[7] of the target photons in erg/cm^3 units. In Fig.4.21 we show the accurate numerical calculation of the IC cooling time. It is seen that above 1 TeV energies Eq.(4.24) provides quite accurate approximation of the IC cooling time.

The corresponding maximum energy of accelerated electrons in this regime is

$$E_{\rm e,max} \simeq 9 \cdot 10^5 \ \ (B_{\rm G}/w_0)^{3.3} \left(\frac{\eta}{10^3}\right)^{-3.3} \ \ {\rm TeV}\,. \tag{4.25}$$

This somewhat unusual dependence of $E_{\rm e,max}$ on the photon density w_0 is the result of IC scattering in deep Klein-Nishina regime.[8] The very strong dependence of $E_{\rm e,max}$ in Eq.(4.25) on three highly variable parameters, B, w_0 and η, allows variation of $E_{\rm e,max}$ in very broad limits. For example, for the $B \propto 1/d$ type dependence of the B-field, and assuming constant acceleration parameter η, the increase of the separation between the compact object and the star by a factor of two would lead to the change of $E_{\rm e,max}$ by a factor of $2^{3.3} \simeq 10$, and correspondingly to dramatic variation of the flux of highest energy gamma-rays. Obviously, all relevant timescales depend on the pulsar position in the orbit, therefore the high energy cutoff in the spectrum of electrons is expected to be variable. In Fig.4.22 the radiation and acceleration timescales for different epochs – at periastron and $\pm 10, 20, 100$ days from the periastron are shown. For the chosen model parameters, $B = 0.05(d_{\rm per}/d)$ G and $\eta = 4 \times 10^3$, the cutoff in the electron spectrum at the periastron is determined by IC losses, while at large separation distances the synchrotron and escape losses play more important role in formation of the cutoff. This is demonstrated in Fig.4.23, where the high energy cutoff in the electron

---

[7]

$$w_0 = \left(\frac{R_*}{2d}\right)^2 \int \epsilon\, n_{ph}(\epsilon) d\epsilon.$$

[8] In the Thomson regime

$$t_{\rm T} \propto (E_e w_0)^{-1} \quad \rightarrow \quad E_{\rm e,max} \propto (B/w_0)^{1/2}\, \eta^{-1/2}. \tag{4.26}$$

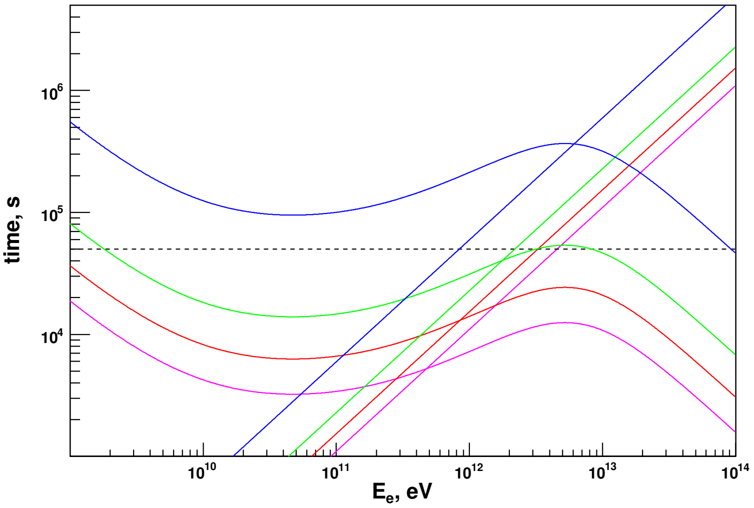

FIGURE 4.22: The acceleration and energy loss times of electrons of different epochs. The combined IC + synchrotron cooling times are calculated assuming $B_0 = 0.05\,(d_{\rm per}/d)$ G and $T = 2.3 \cdot 10^4$ K. The shown acceleration times are from Eq.(4.21) assuming $\eta = 5 \cdot 10^3$. The horizontal black dashed line corresponds to the $T_{\rm esc} = 5 \cdot 10^4$s. Violet lines correspond to the periastron epoch; the red lines to ±10 days; green lines to ±20 days and blue lines to ±100 days. The maximum injection energy due to radiative cooling is determined by crossing of the same type lines. The maximum energy related to the electron escape is determined by crossing of an acceleration line with the escape line.

spectrum is shown as a function of epoch. Red line corresponds to the cutoff resulting from radiation (IC and synchrotron) losses. In this case one expects significant reduction of the cutoff energy at epochs close to the periastron, where strong IC losses push the cutoff energy down to ≤ 1 TeV. Far from the periastron, the cutoff energy can increase up to 10 TeV, unless the losses due to escape become dominant. The IC cooling time at the epoch with separation d is $t_{\rm IC} \simeq 10^3{\rm s}(d/d_{\rm per})^2$ s. Therefore, if the characteristic escape time is about 10^4 s, the impact of particle escape becomes important for separations $d \geq 3\,d_{\rm per}$. This effect is demonstrated in Fig.4.22 where (time and energy-independent) escape time $T_{\rm esc} = 5 \times 10^4$ s is assumed. One can see that for chosen model parameters the cutoff energy is a weak function of time with a local minimum ($\simeq 0.5$ TeV) at periastron, and two maxima ($\simeq 2.5$ TeV) at ±20 days. It is important to note that the introduction of escape losses is crucial for explanation of the observed TeV lightcurve in this scenario. Indeed, while the reduction of the cutoff energy in the spectrum of electrons due to enhanced IC losses satisfactorily explains the minimum at the periastron, one should expect much higher fluxes at large separations in contrast to the HESS observations. The additional assumption that electrons suffer also significant escape losses ($T_{\rm esc} = 5 \times 10^4$ s) allows dramatic suppression of the gamma-ray fluxes beyond $|t| > 20$ days. The impact of the variation of relative contributions of radiative and escape losses on the formation of the energy distributions of electrons is demonstrated in Fig.4.24. The corresponding lightcurves of inverse Compton gamma-rays at $E_\gamma = 1$ TeV, 500 GeV, 100 GeV and 10 GeV are shown in Fig.4.25 compared with HESS measurements of 1 TeV flux (Aharonian et al., 2005).

The agreement of calculations with the HESS lightcurve is rather satisfactory except for somewhat higher predicted flux at the epoch of 2 weeks after the periastron which coincides with the pulsar passage through the stellar disk.

In the scenario of variation of $E_{\rm e,max}$, the lightcurves at TeV and GeV energies have quite different profiles. Namely, the TeV lightcurves have a clear minimum at periastron which is explained by the sub-TeV cutoff in the spectrum of accelerated electrons. At the same

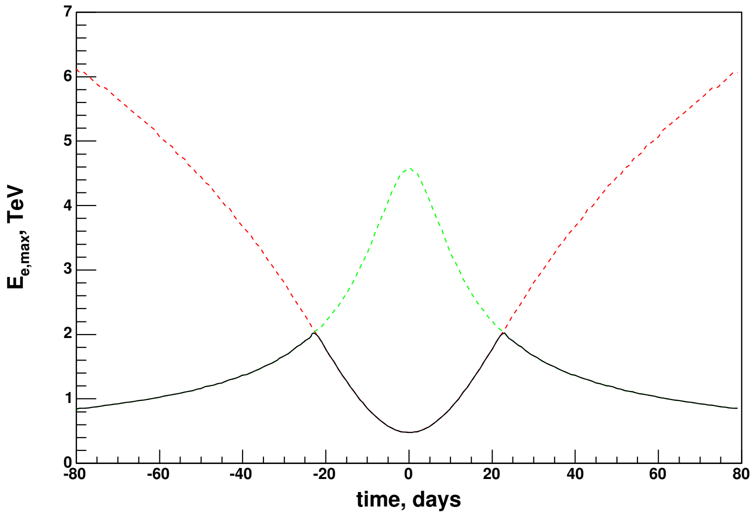

FIGURE 4.23: Maximum energy of electrons at the pulsar wind termination shock. Green dashed line corresponds to cutoff energy caused by electron escape. Red dashed line corresponds to cutoff energy caused by radiative losses. The solid line corresponds to the combined cutoff energy. The model parameters are the same as in Fig.4.22.

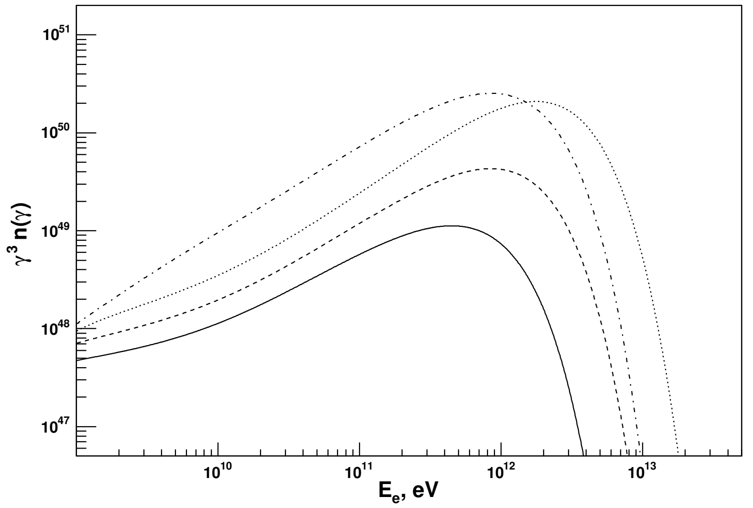

FIGURE 4.24: Electron energy distributions at different epochs. Solid line corresponds to periastron, dashed line to ±10 days, dotted line to ±20 days, dashed-dotted line to ± 80 days. Model parameters are the same as in Fig.4.22.

time this cutoff in the electron spectrum is still sufficiently high and therefore does not have a strong impact at GeV energies (IC scattering is at high energies catastrophic process). Therefore the GeV lightcurves show maximum a few days before the periastron [9]. It is important to note that the significant drop of gamma-ray fluxes at large separations is due to the escape losses, otherwise one should expect rather constant flux with a weak maximum close to the periastron.

---

[9] Note that the shift of the position of the maximum is caused, as discussed above, by the anisotropy of the Compton scattering, but not by the change of the target photon density as long as the IC scattering proceeds in the "saturation regime" (see section 4.1).

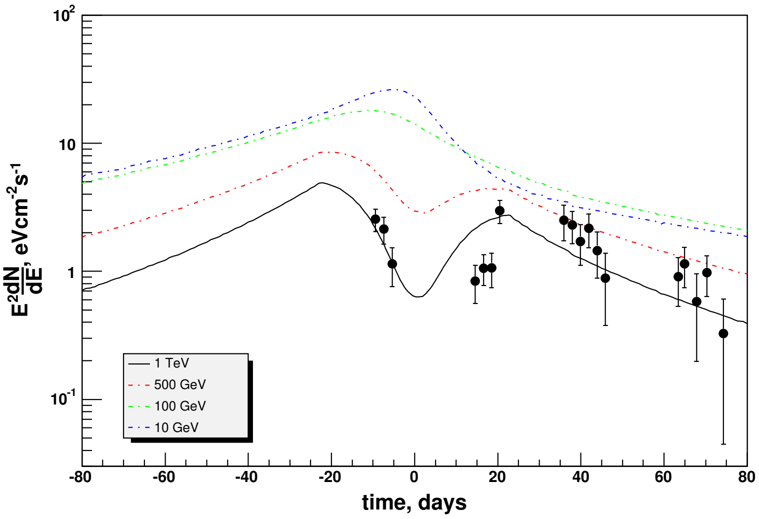

FIGURE 4.25: Lightcurves for different energies in maximum energy cutoff scenario.

In Fig.4.28 we compare the energy spectra reported by HESS with the average TeV gamma-ray spectra calculated for the periods of the HESS observations in February, March and April 2004.

Although it is possible to achieve a better agreement with the measurements, at this stage the attempt for a better spectral fit could be hardly justified given the statistical and systematic uncertainties of measurements.

Also this model predicts different energy spectra of gamma-ray bellow 100 GeV at different epochs. Indeed, at large separations, when the escape losses dominate, the injection spectrum of electrons remains unchanged, therefore we expect noticeably harder gamma-ray spectra in the GeV energy band at epochs $|t| > 20$ days (see Fig.4.26).

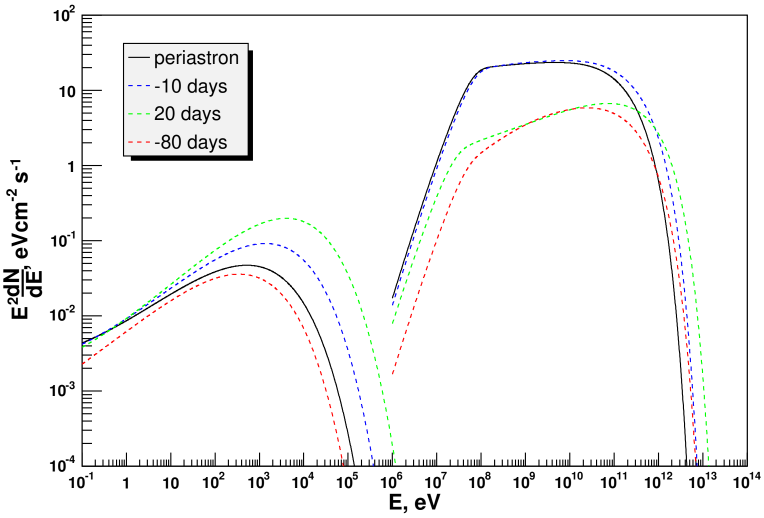

FIGURE 4.26: Synchrotron and Inverse Compton spectra for different days in energy cutoff variation scenario.

Remarkably, the calculated fluxes at GeV energies are well above the sensitivity of GLAST which makes this source a perfect target for future observations with GLAST. It should be noted, however, that the fluxes at GeV energies could be significantly suppressed because of possible low energy cutoff in the acceleration spectrum of electrons – a standard assumption in the models of PWN.

In this scenario, the magnetic field the energy density of the magnetic field at the shock wave should be significantly less than the energy density of stellar photons. Thus, assuming the same strength of the magnetic field in the acceleration and radiation regions, one obtains quite low synchrotron fluxes (Fig.4.26).

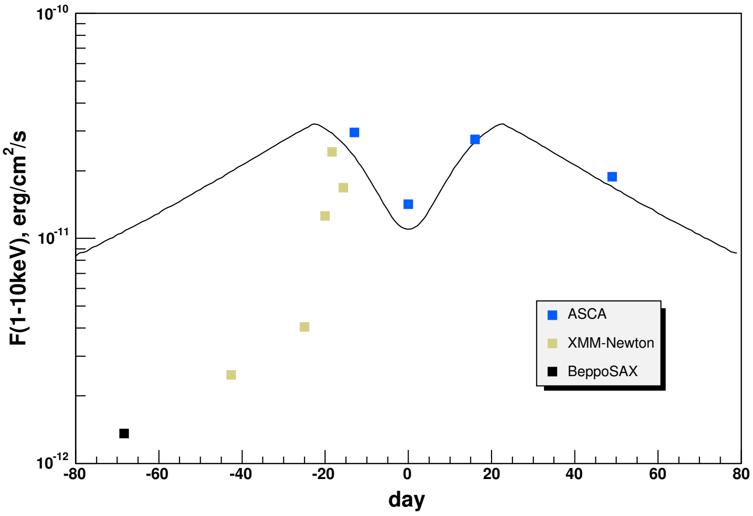

FIGURE 4.27: The X-ray lightcurve calculated for the scenario with early sub TeV cutoff. At shock front the magnetic field was assumed to be $B_0 = 0.03\,(d_{\rm per}/d)$ G, and in the emitting region to be higher by a factor of 10. The acceleration efficiency has value $\eta = 4 \times 10^3$. An orbital-dependent escape time was assumed to be $t_{\rm esc} = 1.75 \times 10^4\,(d/d_{per})^{1/2}$ s. The blue point sets correspond to ASCA (Hirayama et al., 1996), brown points to XMM-Newton (Chernyakova et al., 2006) and black point to BeppoSAX (Chernyakova et al., 2006) observations, respectively.

This would imply that the observed X-rays have non-synchrotron origin (e.g. IC origin; see Chernyakova et al. 2006). Another possibility is to assume that the magnetic field in the radiation region is somewhat higher than at the shock (note that that a similar situation takes place in the Crab nebula Kennel & Coroniti 1984b). In Fig.4.27 we show the lightcurve of 1-10 keV X-rays, assuming that in the radiation region the magnetic field is stronger by a factor of 8. If so, the synchrotron X-ray flux could achieve the observed flux level. In this scenario the X-ray and gamma-ray production regions are essentially different, although they could partly overlap. While the bulk of X-rays is formed in a magnetized region(s) far from the shock (where the electrons are accelerated), the IC gamma-rays come from more extended zones, which includes also the site of particle acceleration.

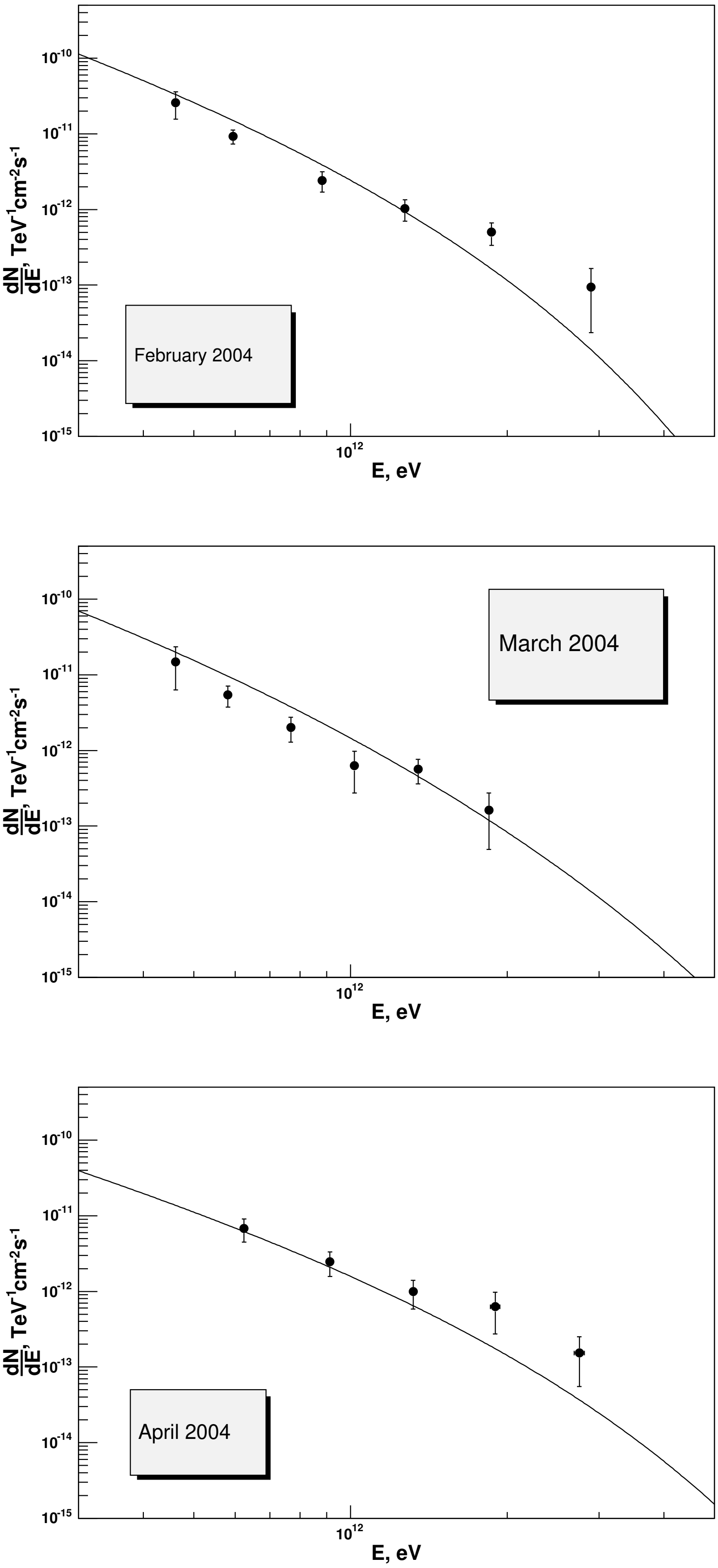

FIGURE 4.28: The averaged IC radiation during the H.E.S.S. observation period of February, March and April 2004 in maximum energy cutoff model.

4.4 Comptonization of the unshocked wind

Compton deceleration

While in the previous sections we tried to explain the observed modulation of TeV gamma-rays fluxes by energy losses of accelerated electrons at the termination of the wind, it is interesting to investigate whether one can relate the observed TeV lightcurve to the Compton losses of the kinetic energy of the bulk motion of the cold ultrarelativistic wind.

Generally this effect can be important in a binary system with a high luminosity companion star. Although the electrons in cold pulsar winds do not suffer synchrotron losses (since magnetic field is frozen into monoenergetic wind), the significant fraction of original kinetic energy of the bulk motion of the electron-positron wind could be radiated away due to the Comptonization. Thus the power available for acceleration of electrons at termination of the wind depends on the position of the pulsar. Obviously, in this scenario we should expect minimum flux of gamma-rays closer to the periastron due to dense photon field from companion star. In other words, while in the previous section the modulation of the gamma-ray flux is linked to the $E_{\mathrm{e,max}}$, in this scenario the gamma-ray flux variation depends on the parameter A characterizing the acceleration power of electrons given by Eq.(3.48).

According to the standard PWN model (Kennel & Coroniti, 1984b) the isotropic cold electron-positron wind[10] has a typical bulk motion Lorentz factor $\Gamma \propto 10^4 - 10^6$, thus the interaction of the wind electrons with starlight in the Klein-Nishina limit should lead to the formation of a narrow gamma-ray component with typical energy $\Gamma m_{\mathrm{e}} c^2$.

Since the pulsar wind is monoenergetic, the whole problem can be reduced to the calculation of the energy loss of a single electron due to IC scattering when travelling distance from $l = 0$ to $l = r_{\mathrm{sh}}$ from the pulsar as shown in Fig.4.29.

FIGURE 4.29: Calculation of electron deceleration.

The electrons are ultrarelativistic, therefore the energy absorption per unit length is

$$\frac{dE_{\mathrm{e}}}{dl} = \int E_\gamma \frac{dN}{dl dE_\gamma} dE_\gamma \tag{4.27}$$

where the radiation of electron is calculated by using the fact that electron suffers head-on collisions (i.e. under angle π) with photon field

$$n(\epsilon, r) = \left(\frac{R_*}{2r}\right)^2 n_{\mathrm{ph}}(\epsilon) \tag{4.28}$$

as[11]

$$\frac{dN}{dl dE_\gamma d\Omega} = 2 \int d\epsilon \, n(\epsilon, r(l)) \frac{d\sigma}{dE_\gamma d\Omega}(\Gamma(l), \epsilon, E_\gamma, \pi) \tag{4.29}$$

---

[10] Here we follow a model suggested by (Kennel & Coroniti, 1984b), assuming an isotropic pulsar wind, but it is worthy to note that the pulsar wind can be strongly anisotropic (Bogovalov & Khangoulian, 2002), thus the non-typical lightcurve can be a result of the interaction of two anisotropic winds.

[11] factor of 2 comes from (2.1).

with $d\sigma/dE_\gamma d\Omega$ - IC cross section from (2.2). This gives for total energy loss

$$\Delta E_{\rm e} = 2\int\limits_0^{r_{\rm sh}} dl \frac{R_*^2}{4(d-l)^2}\int dE_\gamma E_\gamma \int d\epsilon\, n_{\rm ph}(\epsilon)\frac{d\sigma}{dE_\gamma d\Omega}(\Gamma(l),\epsilon,E_\gamma,\pi) \qquad (4.30)$$

This effect leads to the modulation of the bulk motion Lorentz factor as shown in Fig.4.31. The calculations in Fig.4.31 were performed for star luminosities $L_* = 2.2{\cdot}10^{38}$, $3.3{\cdot}10^{37}$ erg/s and different values of the initial Lorentz factor of the pulsar wind. Note that in the Thomson regime $t_{\rm IC} \propto \Gamma^{-1}$ (4.26), i.e. the decrease of wind Lorentz factor leads to the increase of the cooling time. On the other hand, in the Klein-Nishina regime the cooling time increases with Lorentz factor as $t_{\rm IC} \propto \Gamma^{0.7}$ (4.24). Therefore the maximum effect is achieved in the Thomson-to-Klein-Nishina transition region, i.e. around $\Gamma_0 = 10^5$.

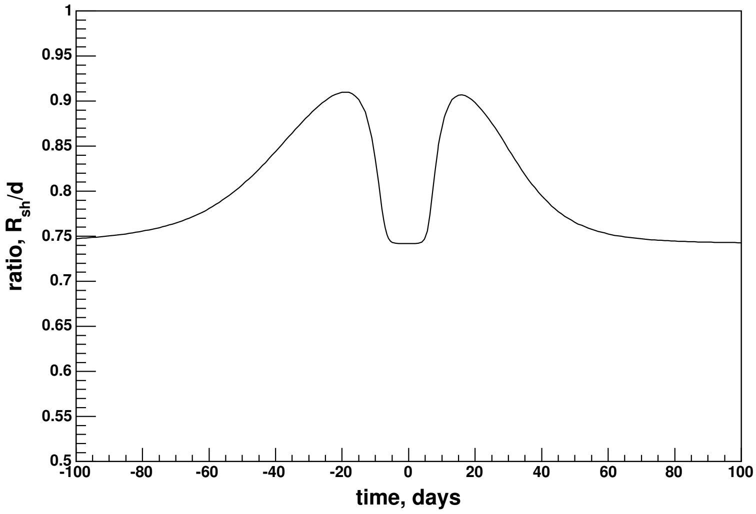

FIGURE 4.30: The profile of shock radius using typical parameters of Be-star outflow used to calculate compton deceleration of cold pulsar wind.

As it follows from Fig.4.31, the initial Lorentz factor of the wind for $\Gamma_0 = 10^5$ for star luminosity $L_* = 2.2 \cdot 10^{38}$ erg/s is reduced by 40% at periastron. Interestingly, minimum reduction of the initial Lorentz factor ($\sim 5\%$) happens around $t = \pm 20$ days. Since the kinetic energy of the wind radiated away due to the Comptonization is determined by the starlight density and the length of the unshocked wind $\Delta l = r_{\rm sh}$, the lightcurve is explained by the combination of two factors – dependence of the starlight density on the separation d, and the distance to the wind termination point (it is assumed that the gas density of the stellar wind decreases as d^2). Obviously, in the case of electron-positron pulsar wind, the kinetic energy of bulk motion of the wind, and consequently the rate of shock accelerated electrons have similar time behaviors: $A = A_0\Gamma(t)/\Gamma_0$, where[12] A_0 characterizes the original power of the wind.

Although qualitatively this behavior agrees with the TeV lightcurve detected by HESS, the effect of reduction of the kinetic energy of the wind is not sufficient to explain quantitatively the observed TeV lightcurve. Indeed, the Comptonization of the wind can lead to the reduction of the energy flux of TeV gamma-rays at periastron by only a factor of ≤ 1.5, while

---

[12] A is from eq. (3.48)

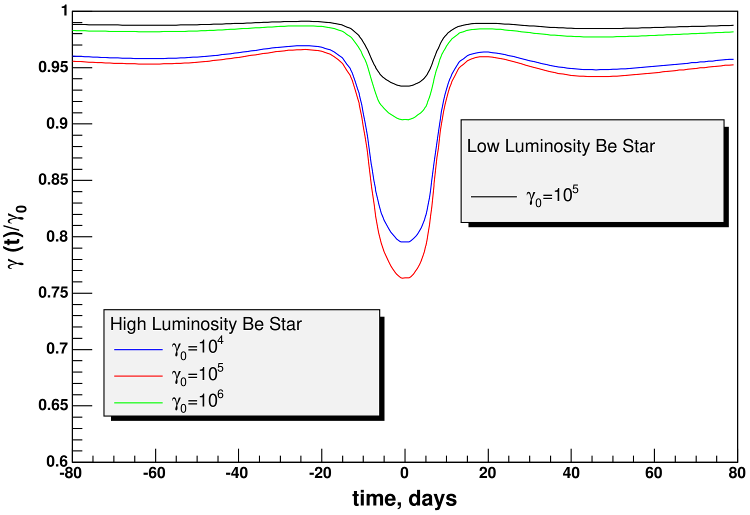

FIGURE 4.31: The time-evolution of the wind Lorentz factor just before the termination. The results are presented for the initial Lorentz factors $\Gamma_0 = 10^5$ (red line), $\Gamma_0 = 10^6$ (green line) and for $\Gamma_0 = 10^4$ (blue line) for the luminosity of the companion star $L_* = 2.2 \cdot 10^{38}$ erg/s. Black line shows the time evolution of the wind Lorenz factor for $\Gamma_0 = 10^5$ calculated the luminosity of the companion star $L_* = 3.3 \cdot 10^{37}$ erg/s.

the HESS observations show more significant variation of the gamma-ray flux. Assuming somewhat larger, by a factor of two, higher luminosity of the optical star, one can get a better agreement with the observed TeV lightcurve. However, the range of the luminosity of the star discussed in the literature, favors a lower luminosity of the star (Tavani & Arons, 1997; Kirk et al., 1999). Therefore the effect of Comptonization of the pulsar wind cannot play, even for $\Gamma_0 \sim 10^5$, a major role in the formation of the TeV lightcurve.

Energy spectra of radiation

Even so, this effect cannot be ignored in the calculations of the overall gamma-radiation of the system. Namely the Comptonization of the ultrarelativistic pulsar wind unavoidably leads to an additional component of gamma-rays produced at the pretermination stage of the wind. Again, since the pulsar wind is monoenergetic, the whole problem can be reduced to calculation of the radiation from a single electron using same geometry as in calculation of absorption (section 4.1) shown in Fig.4.7. Energy spectrum of radiation of a single electron at point l on the trajectory is given by

$$\frac{dN}{dtdE_\gamma d\Omega}(E_\gamma, l) = c \int d\epsilon \, n(\epsilon, r(l)) \frac{d\sigma}{dE_\gamma d\Omega}(\Gamma(l), \epsilon, E_\gamma, \theta(l))(1 - \beta \cos\theta) \tag{4.31}$$

with angle θ and distance r are given by (4.14).
Evolution of Lorentz factor of ultrarelativistic electron is

$$\frac{d\Gamma}{dl} = \frac{1}{c} \int E_\gamma \frac{dN}{dtdE_\gamma} dE_\gamma. \tag{4.32}$$

Therefore to obtain total spectrum of electrons we must sum over all spectra given by formula (4.31) (i.e. integrate over dl) and multiply them by a number of electrons contained in length element $dl = c\,dt$.

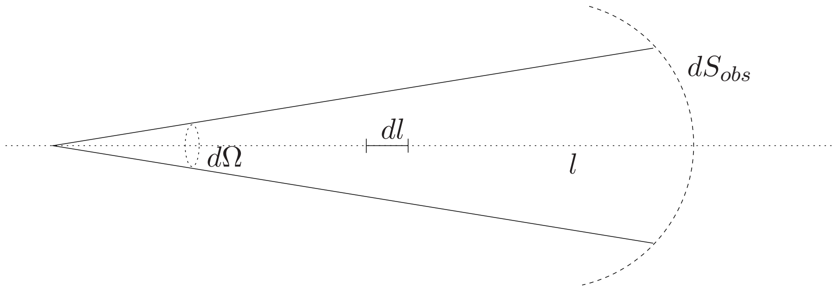

For the radial flux of electrons $F = dN_{\rm e}/dSdt$ at distance l through solid angle $d\Omega$ (see figure above)

$$\frac{dN_{\rm e}}{dt} = Fl^2 d\Omega.$$

holds. Electrons reach the area element of detector from constant solid angle given by $dS = D^2 d\Omega$, therefore the number of electrons corresponding to radial element dl is

$$\frac{dN_{\rm e}}{dl} = \frac{Fl^2}{c}\frac{dS}{D^2}. \tag{4.33}$$

Total number of electrons is related to spin-down luminosity of the pulsar by $dN_{\rm e}/dt = L/\Gamma_0 mc^2 = F4\pi l^2$, which gives

$$\frac{dN_{\rm e}}{dl} = \frac{L}{4\pi\Gamma_0 mc^3}\frac{dS}{D^2}. \tag{4.34}$$

Summarizing, the total irradiated spectrum then is

$$\frac{dN}{dSdtdE_\gamma} = \frac{L}{4\pi D^2\Gamma_0 mc^2}\int\limits_0^{r_{\rm sh}} dl \int d\epsilon n(\epsilon, r(l))\frac{d\sigma}{dE_\gamma d\Omega}(\Gamma(l), \epsilon, E_\gamma, \theta(l))(1-\beta\cos\theta) \tag{4.35}$$

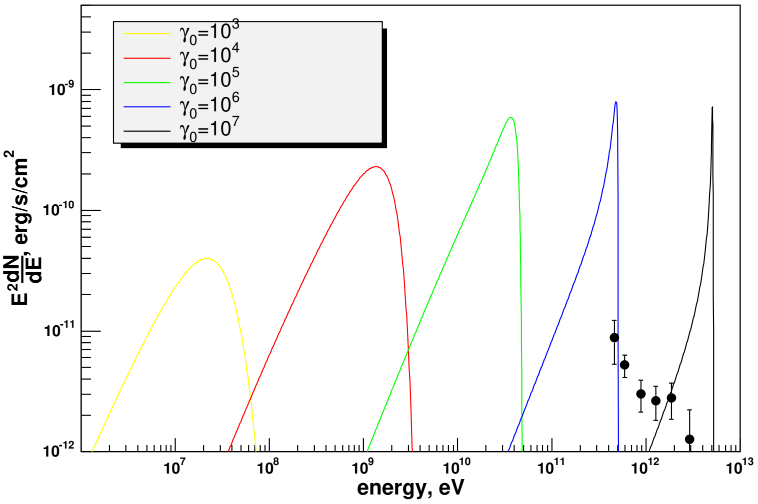

FIGURE 4.32: The energy spectra of gamma-rays due to the Comptonization of the unshocked wind at the periastron are calculated for initial Lorentz factor $\Gamma_0 = 10^3, 10^4, 10^5, 10^6$ and 10^7 (indicated at the curves). The luminosity of the companion star was assumed $L_* = 2.2\cdot 10^{38}$ erg/s. The experimental points correspond to the average energy spectrum measured by HESS within several weeks around the periastron.

Due to the inverse Compton scattering of monoenergetic electrons on target photons with narrow, e.g. Planckian distribution, we should expect a specific, especially for $\Gamma_0 \geq 10^5$, line-type gamma-ray emission (Bogovalov & Aharonian, 2000; Ball & Kirk, 2000; Ball & Dodd, 2001). Ball & Kirk (2000) have calculated the IC radiation of the freely expanding wind, i.e. under assumption that the wind was not terminated. These calculations can be hardly applied for this system, because we do see broad-band IC radiation of the shocked wind. As it was shown in the paper by Ball & Dodd (2001), such an assumption leads to significant (an order of magnitude) overestimation of the gamma-ray flux. However in this paper calculations are performed only for one value of Lorentz factor $\Gamma = 10^6$ and to supply this gap we performed calculations for a number of probable Lorentz factors. The results of calculations of gamma-ray spectra of the unshocked wind are shown in Fig.4.32. Comparison of these calculations with the average energy spectrum of PSR B1259-63 measured by HESS excludes the initial Lorentz factor of the wind $\Gamma_0 = 10^6$. Otherwise, the flux of the Comptonized emission of the unshocked wind would significantly exceed the observable flux (see Fig.4.32). Due to the energy range of gamma-rays from this source available for HESS ($E \geq 300$ GeV), the future observations unfortunately cannot significantly improve this limit.

On the other hand, such studies can be performed by GLAST the sensitivity of which seems to be adequate for a deep probe of the initial wind Lorentz factors of PSR B1259-63 within 10^4 to 10^6. Thus, GLAST has a unique potential to prove the current pulsar wind paradigm which assumes that the bulk of the spin-down luminosity of the pulsar is transformed to a cold wind with Lorentz factor exceeding 10^4.

Chapter 5

Adiabatic expansion of plasma

In the previous chapter we introduced particle energy losses due to adiabatic expansion, however we did not discuss the specific aspects of this process.

Let us consider the following demonstrative example. On microscopic level adiabatic losses of a particle occur when a particle with velocity v hits the wall, which itself moves with velocity V (see Fig.5.1). Since in the adiabatic process no heat transfer takes place, in the rest frame of the wall the particle suffers an elastic collision.

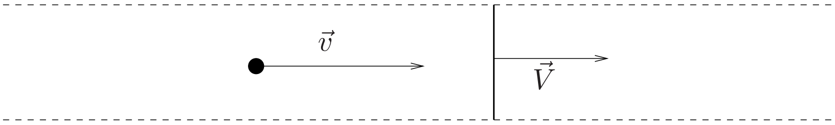

FIGURE 5.1: Adiabatic losses.

For nonrelativistic velocities the change of energy ΔE per collision is

$$\Delta E = 2mV(V - v). \tag{5.1}$$

In one-dimensional expansion the timescale of a single scattering is estimated as $\Delta t \sim 2l/v$, where l is the characteristic size of the system, which considering $v \gg V$ gives

$$\frac{1}{E}\frac{\Delta E}{\Delta t} \sim -\frac{V}{l} \tag{5.2}$$

i.e. the timescale of adiabatic losses for nonrelativistic expansion is $t_{\rm ad} \sim l/V$.

In the following we will analyze the problem of one-dimensional adiabatic expansion of plasma in the case of absence of the wall, but when the adiabatic losses still take place due to the transformation of internal energy to bulk motion. This case can be realized in many astrophysical scenarios.

5.1 Formulation of the problem

Below we assume assume a pipe[1] that is placed along the x-axis in an external isotropic photon field $n(\epsilon)$ (see Fig.5.2). Let assume that electrons are continuously injected into pipe at point $x = 0$. When expanding adiabatically, the particles are accelerated into a bulk motion

---

[1] the pipe represents collimated outflow, which for example can be formed between boundaries of 2 standing shocks.

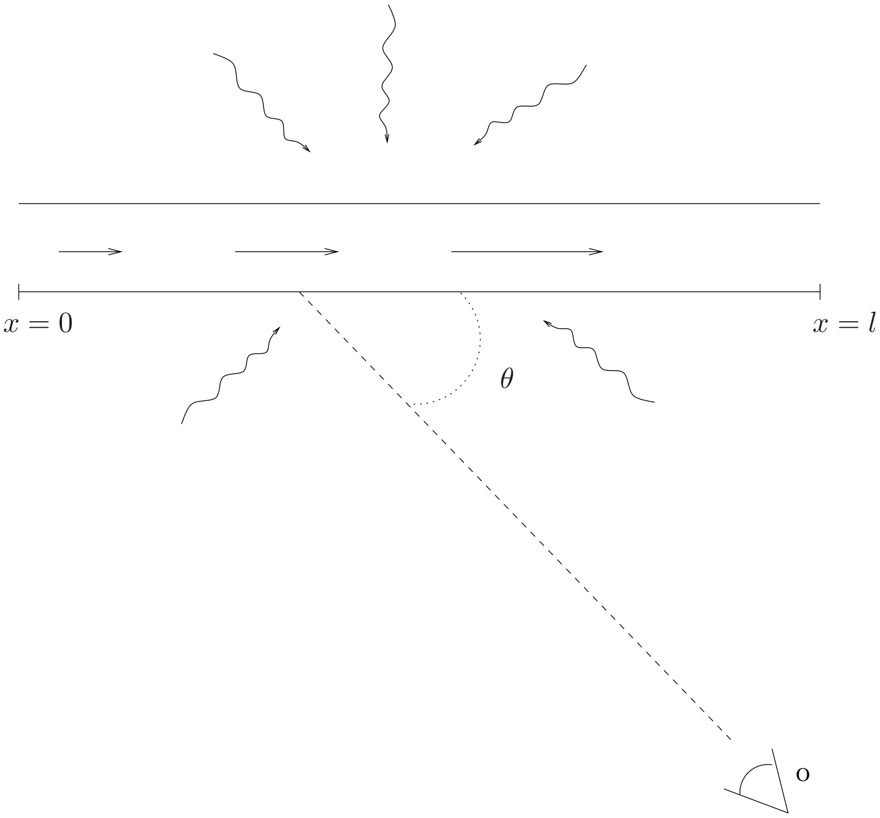

FIGURE 5.2: Adiabatic expansion of plasma.

along the x-axis carrying “frozen-in“ magnetic field.
Since the size of the source is much smaller than the distance to the observer, it allows us to treat the source as a point-like. This means that we are interested only in the distribution of particles in Γ-space (Γ is the Lorentz factor of bulk motion). The spatial quantities, which can be calculated using complete set of MHD equations, are in this case not needed for the calculation of radiation. We will proceed as follows: we will label the particles by the time they leave the source (so-called Lagrange variables) and apply to them the energy conservation law. Since the form of adiabatic losses is given empirically, which means that we know what amount of internal energy is converted into bulk motion per unit time - this will be the key to derive the Lorentz factor of the mass center of labelled particles (which we call Γ-profile). To obtain the total electron spectrum we will integrate over all labelled particles. Finally, we will calculate the radiation produced by IC scattering of electrons on the background photons with distribution $n(\epsilon)$ (see Fig.5.2) and compare the results with calculations performed for constant (averaged) bulk velocity of particles.

5.2 Electron spectrum formation equation

Since the cross-section of IC process and photon field are known, we need to determine the energy spectrum of electrons. Because of the adiabatic expansion, the momentum distribution of electrons in laboratory frame in general, is not isotropic. The number of electrons moving in direction to the observer at angle θ (see Fig.5.2) is increasing with reduction of θ, due to increase of bulk velocity in x-direction.

The electron spectrum can be described by the Lagrange variable τ as

$$N_e(\gamma, \Omega, t) = \int_0^t n_e(\gamma, \Omega, \tau) d\tau. \tag{5.3}$$

The meaning of Eq.(5.3) is the following. For a source function $q(\gamma)$ at point $x = 0$ (see Fig.5.3) with the meaning of $q(\gamma)\Delta t$ as the number of electrons per energy injected in time intervals Δt, the total electron spectrum is formed as a sum of all partial spectra $n_{\rm e}$ at the points $x(i \cdot \Delta t)$ separated by intervals $\Delta x_i = V(x_i)\Delta t$. Note that the coordinate $x(t)$ represents the *center of mass* of particles injected at time $-t$, therefore the separated particles in principle can be found anywhere in the pipe.

FIGURE 5.3: Lagrange variables.

Assuming that the magnetic field is frozen in plasma and quick isotropisation of particles in local comoving frame, the time development of $n'_{\rm e}$ is given by

$$\frac{\partial n'_e}{\partial t'} + \frac{\partial(\dot\gamma' n'_e)}{\partial \gamma'} = q(\gamma)\delta(t') \tag{5.4}$$

where primes refer to frame locally comoving with plasma.
This equation is equivalent to homogeneous equation with an initial condition $n(t' = 0) = q(\gamma)$. The electron energy losses in equation (5.4) also depend on Lorentz factor of bulk motion[2] Γ, and therefore also on time t. To obtain formal solution of Eq.(5.4) let us consider a simplier case when the energy losses are time independent $\dot\gamma' = \dot\gamma'(\gamma')$. For this case the solution obtained using method described in Appendix B is

$$n'(\gamma', t') = \frac{\dot\gamma'(\gamma'_{\rm eff}) n'_0(\gamma'_{\rm eff})}{\dot\gamma'(\gamma')} \tag{5.5}$$

For the case of dominant adiabatic losses (see Eq.B.11)

$$\gamma'_{\rm eff} = \gamma' e^{At'} \tag{5.6}$$

and for the initial condition $q(\gamma') \propto \gamma^{-2}$ one has

$$n'(\gamma', t') = n'_0(\gamma' e^{At'}) e^{At'} \propto \gamma^{-2} e^{-At'}. \tag{5.7}$$

Solution (5.5) has the following physical interpretation: $\dot\gamma'(\gamma'_{\rm eff}) n'_0(\gamma'_{\rm eff})$ represents the number of particles passing (in the γ-space) per unit time through the boundary given by energy $\gamma'_{\rm eff}$. After time t' the same number of particles, arrive with energy γ' given by Eq.(5.6), is $\dot\gamma'(\gamma')n'(\gamma')$.
Furthermore, we can iteratively generalize this result for the case of time-dependent electron energy losses:[3]

$$\left[\dot\gamma'(\gamma') n'(\gamma')\right]_{t'+dt'} = \left[\dot\gamma'(\gamma'_{\rm eff}) n'(\gamma'_{\rm eff})\right]_{t'} \tag{5.8}$$

---

[2] background photon density, relevant for IC losses, changes when boosted by Γ

[3] note that this is consequence of the local comoving frame method, i.e. in this frame the velocity of bulk motion does not change.

i.e.

$$n'(\gamma', t'+dt') = n'(\gamma'_{\rm eff}, t')\frac{\dot{\gamma}'(\gamma'_{\rm eff}, \Gamma(t'))}{\dot{\gamma}'(\gamma', \Gamma(t'+dt'))} \tag{5.9}$$

where $\gamma'_{\rm eff}$ is given by

$$\gamma'_{\rm eff} = \gamma' - \dot{\gamma}'(\gamma', \Gamma(t'))dt'. \tag{5.10}$$

To obtain electron energy losses in the local comoving frame and partial electron spectra $n'_{\rm e}$ in the laboratory frame, we will need Γ-profile of bulk motion.

5.3 Γ-profile of bulk motion

The profile of bulk motion Lorentz factor Γ can be obtained from energy conservation law. Let us consider group of particles given by $n'_{\rm e}$ (i.e. labelled by Lagrange variable from Eq.(5.3)) in Eq.(5.4) moving along x-axis. Their internal energy is

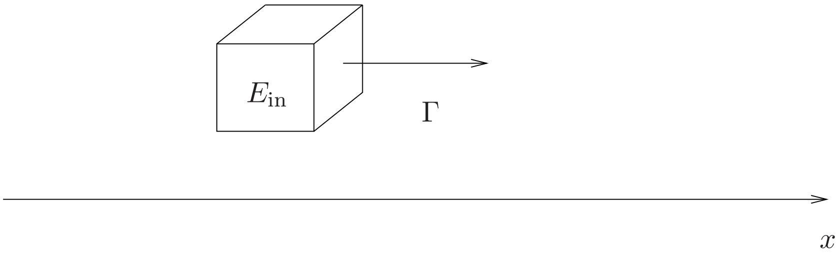

$$E_{\rm in}(t) = m_{\rm e}c^2\int\gamma' n'_{\rm e}(\gamma', t)d\gamma'. \tag{5.11}$$

The total energy in the lab frame is obtained from Lorentz transformations as

$$E = \Gamma E_{\rm in} \tag{5.12}$$

since in local comoving frame the average momentum of electrons is zero.
The energy conservation law for the considered group of particles is

$$\frac{dE}{dt} = \Gamma\frac{dE_{\rm in}}{dt} + E_{\rm in}\frac{d\Gamma}{dt} = \Gamma\left(\frac{dE_{\rm in}}{dt}\right)_{\rm rad} \tag{5.13}$$

where right side represents the energy loss rate of the system due to radiation[4]. Time derivative of internal energy can be obtained using Eq.(5.4)

$$\frac{dE_{\rm in}}{dt'} = mc^2\int\gamma'\frac{\partial n'_{\rm e}}{\partial t'}d\gamma' = \delta(t')E_{\rm in}(t') + mc^2\int\dot{\gamma}' n'_{\rm e}d\gamma' =$$
$$\delta(t')E_{\rm in}(0) + \left(\frac{dE_{\rm in}}{dt'}\right)_{\rm ad} + \left(\frac{dE_{\rm in}}{dt'}\right)_{\rm rad}. \tag{5.14}$$

The ratio of time intervals dt'/dt given from Lorentz transformations for comoving frame is

$$dt = \Gamma(t)dt'. \tag{5.15}$$

Then

$$\frac{d\Gamma}{dt} = -\delta(t) - \frac{1}{E_{\rm in}}\left(\frac{dE_{\rm in}}{dt'}\right)_{\rm ad}. \tag{5.16}$$

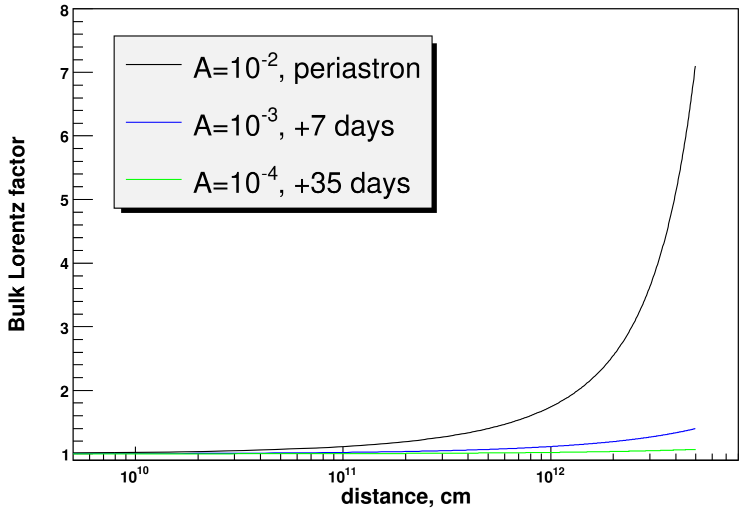

FIGURE 5.4: Bulk Lorentz factor of the plasma for different values of adiabatic expansion coefficient A, taken from adiabatic loss model (section 4.2)..

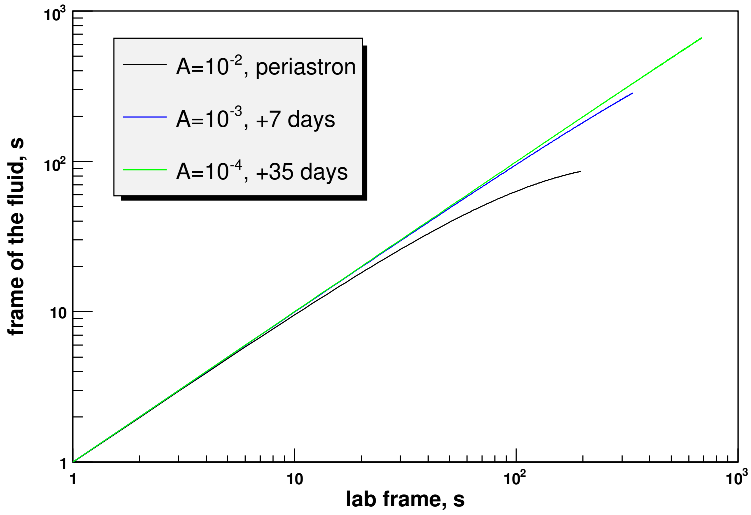

FIGURE 5.5: Time in fluid frame vs time in lab frame.

The adiabatic loss timescale is given empirically in laboratory frame as $t_{\mathrm{ad}} = A^{-1}$ (see section 4.2). In nonrelativistic case this time does not change under Galilei's transformations - strictly speaking adiabatic timescale is given by change of the internal energy (invariant under transformations) in time. Therefore in relativistic case, the timescale in comoving frame is transformed according to Lorentz transformations

$$-\frac{1}{t'_{\mathrm{ad}}} = -\frac{\Gamma}{t_{\mathrm{ad}}} = A\Gamma = \frac{1}{E_{\mathrm{in}}}\left(\frac{dE_{\mathrm{in}}}{dt'}\right)_{\mathrm{ad}} \tag{5.17}$$

---

[4] We consider interaction between electrons to be negligible.

Combining this with an initial condition $\Gamma(0)=1$ we obtain

$$\Gamma(t)=e^{At} \quad , \quad \Gamma(t')=\frac{1}{1-At'}. \tag{5.18}$$

The corresponding coordinate is obtained from the equation $x=\int_0^t V(\tau)d\tau$

$$x(t)=\frac{c}{A}\left[\ln\left(\Gamma+\sqrt{\Gamma^2-1}\right)-\frac{\sqrt{\Gamma^2-1}}{\Gamma}\right]. \tag{5.19}$$

The length of the interaction region (pipe) is determined by competition between (1) the dynamic time of the system $t_{\rm dyn}$, (2) the cooling time of the electrons $t_{\rm cool}$ (time after which electrons are cooled to temperature $T=0$) and (3) the characteristic length scale of interaction region.

Fig.5.4 shows the profile of Lorentz factor for different values of inverse expansion time A obtained for the binary PSR B1259-63/SS 2883 (see section 4.2), where the length of interaction region was chosen to be $5\cdot 10^{12}$ cm (of order of shock radius). One can see that the maximum Lorentz factor $\Gamma_{\rm max}\sim 7$ is achieved for adiabatic cooling timescale 10^2 s derived for periastron and the minimum Lorentz factor $\Gamma_{\rm min}\approx 1.07$ for the characteric cooling time 10^4s derived for ±35 days from periastron.

5.4 Transformation of the distribution functions.

In previous section we derived the Γ-profile of expanding plasma. To obtain electron spectra we must at first solve Eq.(5.9). This equation requires expression for the photon field in local comoving frame. After obtaining electron distribution in local comoving frame $n'_{\rm e}$ by solving Eq.(5.9), we must transform it to the laboratory frame. Afterwards we can use it in calculation of total electron spectrum given by Eq.(5.3).
Finally, we have to perform transformation of (i) electron distribution from local comoving frame to the laboratory frame, (ii) photon distribution from laboratory frame to the local comoving frame.

First, let us start with electron distribution function defined as

$$dN=n(\gamma,\Omega_p)d\gamma d\Omega_p \tag{5.20}$$

Using the invariant

$$\frac{d^3p}{\gamma}=\frac{p^2dpd\Omega_p}{\gamma}={\rm inv.} \tag{5.21}$$

and well known $pdp=m^2c^2\gamma d\gamma$ we arrive at

$$dN=\frac{n(\gamma,\Omega_p)}{m^2c^2p}\frac{p^2dpd\Omega_p}{\gamma}={\rm inv.} \tag{5.22}$$

which gives

$$\frac{n(\gamma,\Omega_p)}{p}={\rm inv.} \tag{5.23}$$

Analogical procedure can be done for the photon distribution, i.e. when distribution function represents energy-space density

$$dN=n(\epsilon,\Omega_p)d\epsilon d\Omega_p dV \tag{5.24}$$

and using invariant phase-space volume

$$d\Phi = d^3p\,dV = p^2dpd\Omega_p dV = \frac{p\epsilon}{c^2}d\epsilon d\Omega_p dV = \text{inv.} \tag{5.25}$$

we arrive at

$$\frac{n(\epsilon, \Omega_p)}{p\epsilon} = \text{inv.} \tag{5.26}$$

5.5 Photon field in boosted frame

For photons $pc = \epsilon$, therefore using Eq.(5.26) and assuming an isotropy of photon field in the laboratory frame, we obtain

$$n'(\epsilon', \Omega'_p) = \frac{1}{4\pi}\frac{\epsilon'^2}{\epsilon^2}n(\epsilon) \tag{5.27}$$

where $n(\epsilon)$ is the photon distribution in laboratory frame integrated over the solid angle Ω_p. The relations between photon energies in different frames are

$$\epsilon = \Gamma(\epsilon' + Bk'_x) \quad , \quad \epsilon' = \Gamma(\epsilon - Bk_x). \tag{5.28}$$

where B is the bulk motion velocity (in units of c) and $\vec{k}$ is the photon momentum vector. Introducing the spherical coordinates in the form

$$k'_x = \epsilon' \cos\theta' \tag{5.29}$$

where $\pi - \theta'$ is the angle between $\vec{k}$ and x-axis, we have

$$\epsilon = \Gamma\epsilon'(1 + B\cos\theta') \quad , \quad \epsilon' = \Gamma\epsilon(1 - B\cos\theta). \tag{5.30}$$

For the Planckian photon distribution in the laboratory frame, the distribution of photons in the comoving frame is

$$n'(\epsilon', \Omega'_p) = \frac{1}{4\pi}\frac{1}{\pi^2\hbar^3c^3}\frac{\epsilon'^2}{e^{\frac{\Gamma\epsilon'}{kT}(1+B\cos\theta')} - 1}. \tag{5.31}$$

Since in the local comoving frame the electrons are quickly isotropised (i.e. move chaotically and consequently see the incoming photons isotropically), we are interested in the photon distribution integrated over Ω'_p:

$$n'(\epsilon') = 2\pi\int_0^\pi n'(\epsilon', \Omega'_p)d(\cos\theta') = \frac{kT}{2\pi^2\hbar^3c^3}\frac{\epsilon'}{\Gamma B}\ln\left[\frac{1 - e^{-\frac{\Gamma\epsilon'}{kT}(1+B)}}{1 - e^{-\frac{\Gamma\epsilon'}{kT}(1-B)}}\right] \tag{5.32}$$

For small B

$$n'(\epsilon') \approx n_{ph}(\epsilon) + O(B^2) \tag{5.33}$$

and in limit $B \to 0$, $n'(\epsilon') \to n(\epsilon)$, as expected.

Fig.5.6 shows the photon energy distribution in comoving frame for different values of boosting factor Γ. Naturally, the maximum energy of distribution increases with increasing Γ. Consequently, transition into Klein-Nishina regime in IC scattering occurs for lower energies of electrons, which is shown in the plot of IC losses in Fig.5.7. The same plot also shows that asymptotic behavior of losses for high electron energies is independent of the boosting factor Γ. This can be explained using the approximate formula for IC losses in Klein Nishina regime (Blumenthal & Gould, 1970)

$$\dot{\gamma}_{\text{ic,KN}} \propto \int \frac{n'(\epsilon')}{\epsilon'}\left(\ln\frac{4\epsilon'\gamma}{mc^2} - \frac{11}{6}\right)d\epsilon'. \tag{5.34}$$

The energy in denominator behaves like $\epsilon' \propto \Gamma$ and number density as $\int n'(\epsilon', \Gamma)d\epsilon' \propto \Gamma$, consequently these two factors cancel for large electron energies.

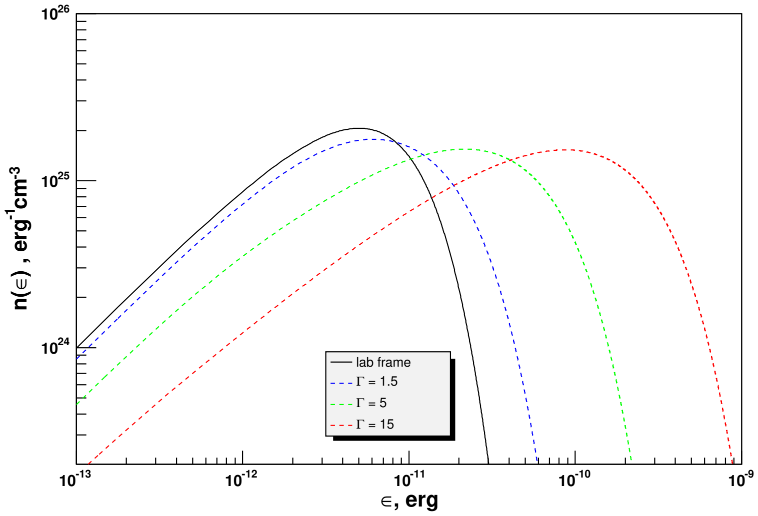

Figure 5.6: Soft photon distribution in lab frame for various values of bulk Lorentz factor Γ. Black curve corresponds to the Planckian distribution in laboratory frame.

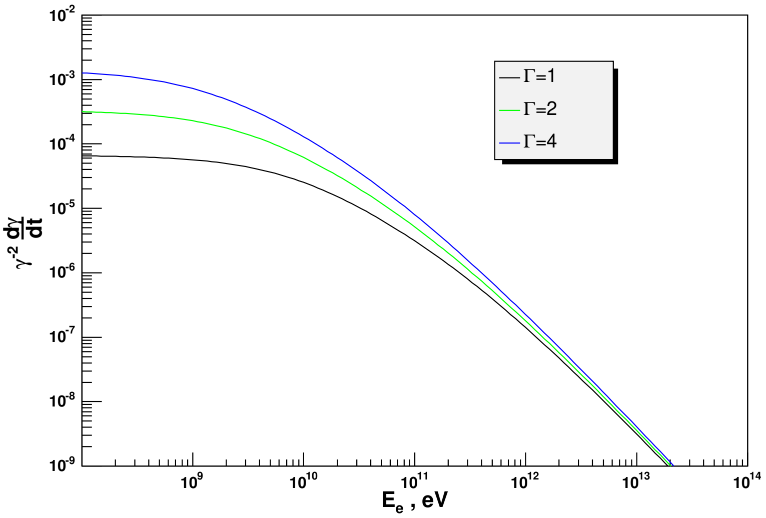

Figure 5.7: Inverse Compton losses for different values of bulk Lorentz factor Γ.

5.6 Spectra of electrons and energy spectra of radiation

The Lorentz transformations for the electron energies are

$$E_e = \Gamma(E'_e + Bp'_x) \quad , \quad E'_e = \Gamma(E_e - Bp_x) \tag{5.35}$$

Introducing spherical coordinates $p'_x = p' \cos\theta'$ where θ' is the angle between electron momentum vector and x-axis we have

$$\gamma' = \Gamma(\gamma - B\sqrt{\gamma^2 - 1}\cos\theta) \tag{5.36}$$

which for large γ gives

$$\gamma' \approx \Gamma\gamma(1 - B\cos\theta) = \delta\gamma \tag{5.37}$$

Since distribution in the local comoving frame is isotropic

$$n'(\gamma', \Omega') = \frac{1}{4\pi} n'(\gamma') \tag{5.38}$$

for the transformation law we get

$$n(\gamma, \Omega) = \frac{1}{4\pi} \frac{\sqrt{\gamma^2 - 1}}{\sqrt{\gamma'^2 - 1}} n'(\gamma') \approx \frac{1}{4\pi\delta} n'(\gamma') \tag{5.39}$$

with

$$\delta = \Gamma(1 - B\cos\theta). \tag{5.40}$$

As expected, the beaming effect is important in the case of relativistic expansion. Figures 5.8- 5.11 show the electron spectra for different values of expansion time, where the density of the photon field corresponds to the periastron passage of PSR B1259-63/SS 2883. The length of expanding region was chosen to be $5 \cdot 10^{12}$ cm.

The comparison is made with the case of bulk motion with average boosting factor defined as

$$< \Gamma >= \frac{\int\limits_0^t \Gamma(\tau) d\tau}{\int\limits_0^t d\tau}. \tag{5.41}$$

One can see significant difference in VHE energy range even for relatively slow expansion (for $t_{\rm ad} = 10^3$s). This is due to the fact that when assuming constant Γ-profile, the spectrum initially cools more rapidly (i.e. decreases rapidly with an increase of the lagrange variable τ in Eq.(5.3) for small τ). The differences in amplitudes of spectra are relatively small for small angles between the system and the observer and become more than an order of magnitude larger for very large angles, $\theta \sim \pi$.

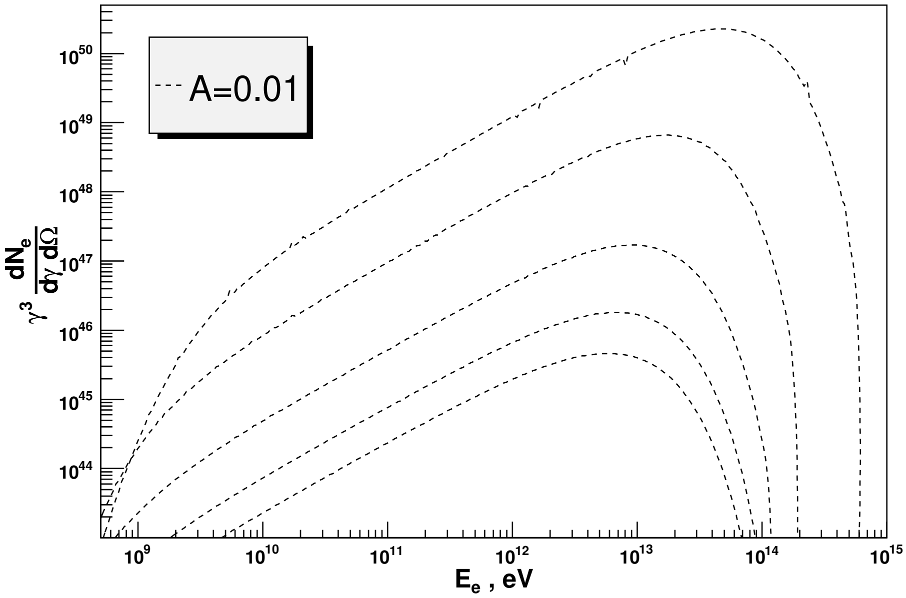

FIGURE 5.8: Total spectrum of electrons in laboratory frame for the value of adiabatic parameter $A = 0.01$. The lines represent different angles θ in direction towards observer from top to bottom for 0°, 15°, 45°, 90°, 180°.

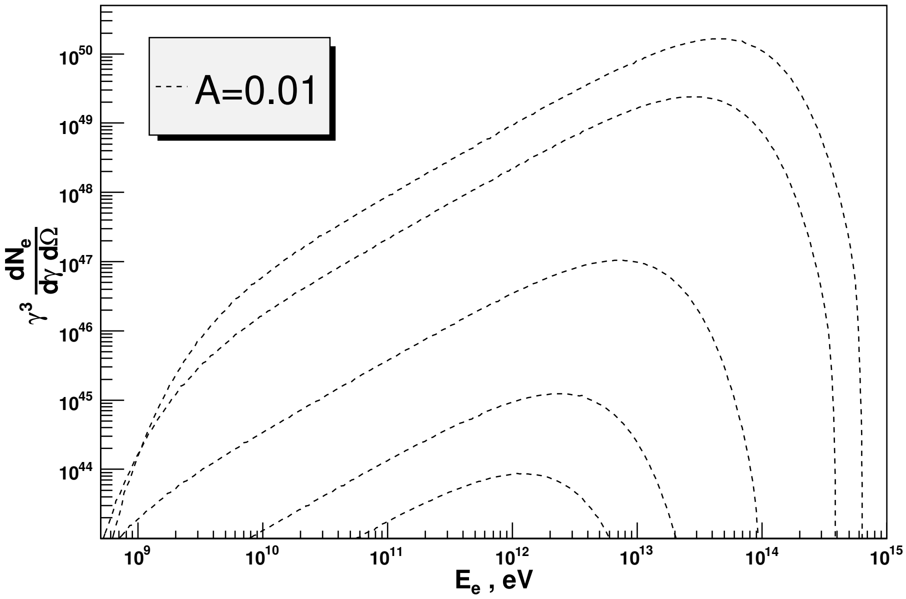

FIGURE 5.9: The same as Fig.5.8, except that Lorentz factor profile is replaced by average Lorentz factor $\Gamma = 3.2$.

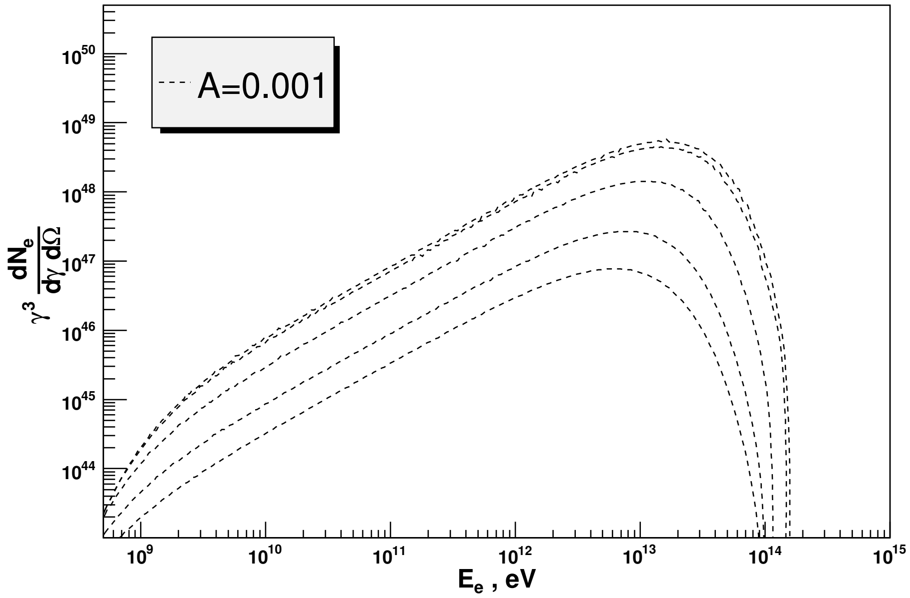

FIGURE 5.10: The same as Fig.5.8, but for value of adiabatic parameter $A = 0.001$.

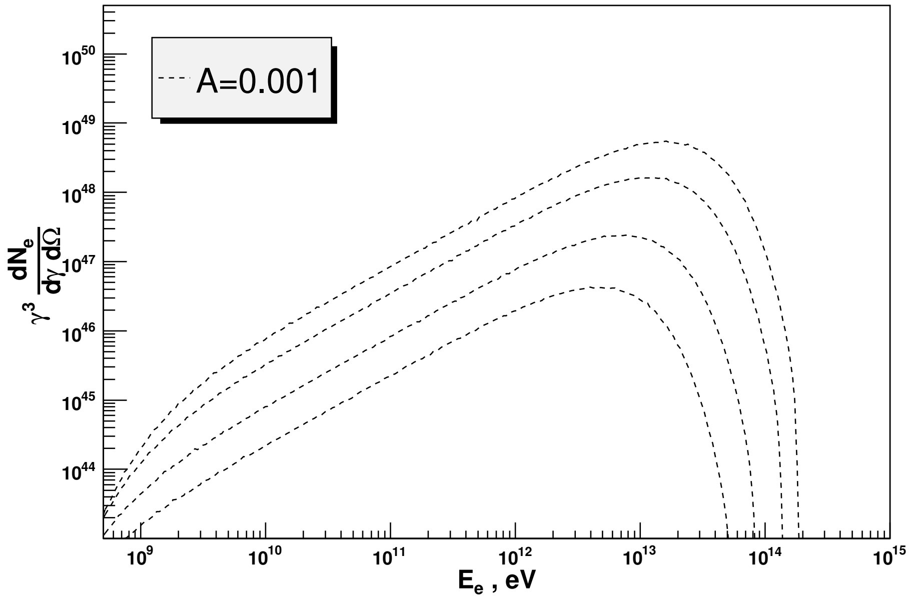

FIGURE 5.11: The same as Fig.5.10, except that Lorentz factor profile is replaced by average Lorentz factor $\Gamma = 1.23$.

Energy spectra of radiation

After the electron spectrum $N_{\mathrm{e}}(\gamma, \Omega, t)$ in the laboratory frame is fixed, the energy spectrum of radiation is given by

$$\frac{dN}{dtdE_\gamma d\Omega} = c \int d\gamma N_{\mathrm{e}}(\gamma, \Omega, t) \int d\epsilon\, n(\epsilon) \frac{d\sigma}{dE_\gamma d\Omega}(\epsilon, \gamma, E_\gamma) \tag{5.42}$$

where $d\sigma/dE_\gamma d\Omega$ is IC cross-section averaged over angles between incoming photon and electron. The outgoing high energy photons are irradiated in direction of incoming electrons, consequently corresponding solid angle is $d\Omega(\theta) = dS/D^2$.

Calculated energy spectra of radiation under different angles corresponding to electron distributions from fig.5.8- 5.11 are shown in fig.5.12- 5.15.
Apparently, the results of calculations of electron spectra are reflected in the energy spectra of radiation. The anisotropy of outgoing radiation increases with increase of inverse adiabatic timescale A, what can be seen when comparing figures 5.12 and 5.14. It is seen, that there is significant difference in VHE parts of spectra (above 1 TeV) and also more than order of magnitude difference in radiation levels for large observer's angles.

In summary, the obtained results show that in general, the use of the average bulk Lorentz factor Γ instead of correct Lorentz factor *profile* of particles, can lead to significantly different results. For example, for adiabatic timescales $10^2 - 10^3$ s and parameters characterizing PSR B1259-63/SS 2883, the levels of observed radiation strongly depend on the observer's angle. The innacuracy of model assuming constant bulk motion Lorentz factor compared to model with Lorentz factor profile increases for: (i) large angles between the observer and the direction of expansion, and (ii) smaller values of characteristic expansion time. The differences in cutoff energies are of factor 2 to 10 depending on combination of the parameters. The differences in levels of radiation are insignificant for large adiabatic timescales[5] (10^4 s) and significant (up to the factor of 10) for smaller adiabatic timescales (10^2 s).

---

[5] this is consequence of chosen lenghtscale of system leading to small average boosting factor $\Gamma_{\mathrm{av}} \sim 1.05$.

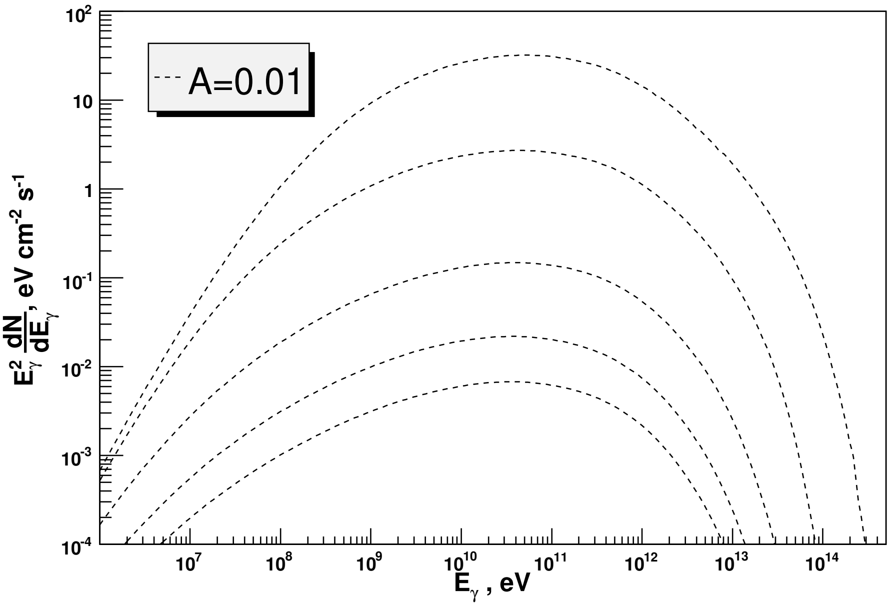

FIGURE 5.12: Broadband IC radiation distribution for the value of adiabatic parameter $A = 0.01$. The lines represent angles as in Fig.5.8.

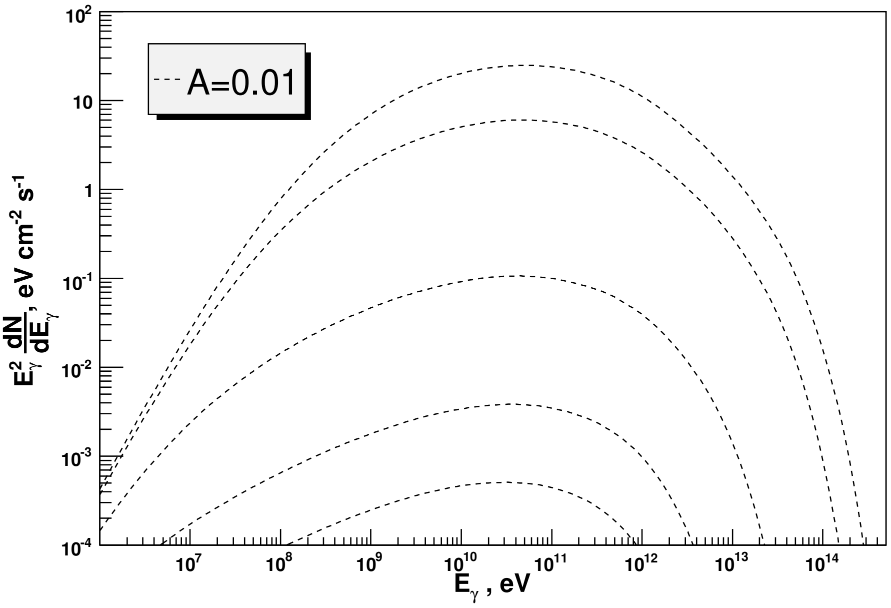

FIGURE 5.13: Broadband IC radiation distribution for the value of adiabatic parameter $A = 0.01$ and average Lorentz factor $\Gamma = 3.2$. The lines represent angles as in Fig.5.12.

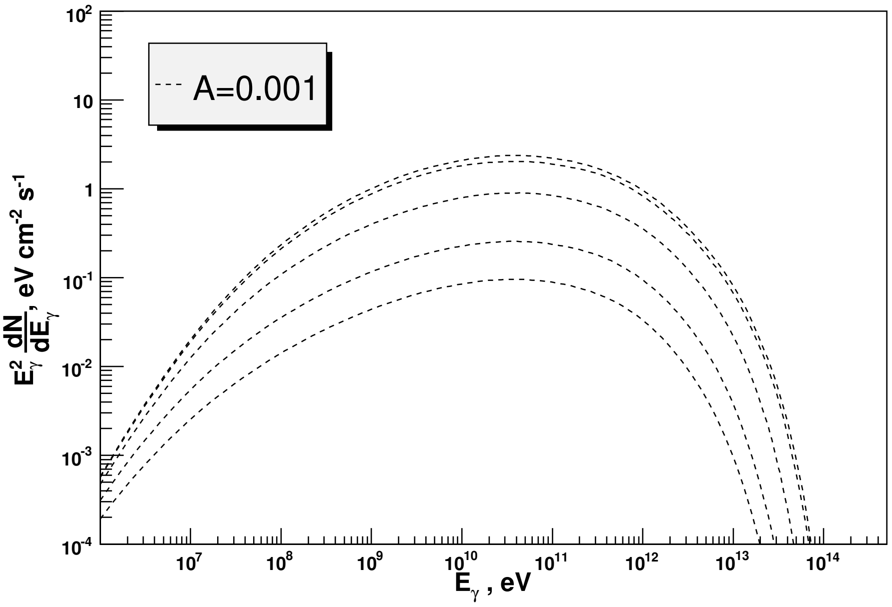

FIGURE 5.14: The same as Fig.5.12, but for the value of adiabatic parameter $A = 0.001$.

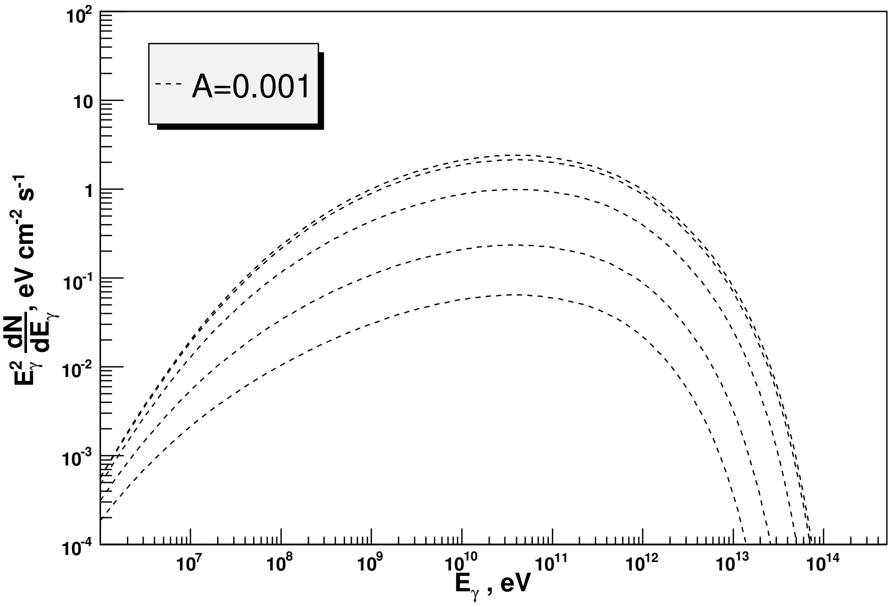

FIGURE 5.15: The same as Fig.5.13, but for the value of adiabatic parameter $A = 0.001$.

Chapter 6

Summary and conclusion

PSR B1259-63/SS 2883 - a binary system consisting of 47ms pulsar orbiting around a luminous Be star - is a unique high energy laboratory for study of nonthermal processes related to the ultrarelativistic pulsar winds. X-ray and gamma-ray emission components are expected from this object due to the radiative (synchrotron and inverse Compton) cooling of relativistic electrons accelerated by the wind termination shock. Generally, the particle acceleration in this complex system can be treated as a scaled-down in space and time (”*compact and fast*”) realization of the current paradigm of Pulsar Wind Nebulae (PWN) which suggests that the interaction of the ultrarelativistic pulsar wind with surrounding medium leads to the formation of a relativistic standing shock. In the case of strong and young pulsars, the shock-accelerated multi-TeV electrons should give rise to observable X-ray (synchrotron) and TeV (inverse Compton) nebulae with typical linear size $\sim 0.1 - 10$ pc. The unambiguous association of some of the recently discovered extended TeV gamma-ray sources with several distinct synchrotron X-ray PWNe generally supports this scenario of formation of nonthermal nebulae around the pulsars.

In the binary system PSR B1259-63/SS 2883 one expects a similar mechanism of conversion of the major fraction of the rotational energy of the pulsar to ultrarelativistic electrons through formation and termination of the cold electron-positron wind. On the other hand, in such systems the magnetohydrodynamic (MHD), acceleration and radiation processes proceed under essentially different conditions compared to the PWN around isolated pulsars. In particular, due to the high pressure of the ambient medium caused by the outflow from the companion star, the pulsar wind terminates quite close to the pulsar, $R \leq 10^{12}$ cm. Consequently, in such systems particle acceleration occurs at presence of much stronger magnetic field and under illumination of intense radiation from the companion star.

This implies that both the acceleration and radiative cooling timescales of TeV electrons are of order of hours, i.e. comparable or shorter than the typical dynamical timescales characterizing the system. This allows a unique ”on-line watch” of the extremely complex MHD processes of creation and termination of the ultrarelativistic pulsar wind and the subsequent particle acceleration, through the study of spectral and temporal characteristics of high energy gamma-radiation of the system. The discovery of TeV gamma-radiation from PSR B1259-63/SS2883 by HESS collaboration provides the first unambiguous evidence of particle acceleration in such systems to TeV energies.

While the absolute fluxes and energy spectra were explained quite well in framework of the published Inverse Compton model, the observed lightcurve appeared to be significantly different from early predictions.

A generic Inverse Compton model, which assumes that whole lost energy of electrons is converted into radiation was thoroughly discussed in section 4.1, using exact formulae

for anisotropic IC cross-section and Planckian spectrum of soft photon field from companion star. This (although numerically more complex) approach is particularly important when *anisotropic* IC scattering proceeds in transition from Thomson to Klein-Nishina regime, which applies to the case of PSR B1259-63/SS 2883. The calculated TeV lightcurve implies almost constant flux over entire orbit resulting from anisotropy of IC scattering *only*, which is in conflict with HESS observations showing significant reduction of the flux towards periastron. To explain the reported TeV lightcurve we proposed two different models.
In the first model, we introduced *variable* adiabatic losses, which we derived from *observed* lightcurve under reasonable physical assumption that adiabatic timescale decreases towards periastron due to decrease of linear size of system. The calculated lightcurves show qualitatively similar shape at all calculated energies, namely for $10\,\mathrm{GeV} - 1\,\mathrm{TeV}$. The obtained IC spectra are in agreement with HESS observations.
In the second model (section 4.3), we investigated maximum energy of accelerated electrons which results from concurrent mechanisms of acceleration with escape and cooling of electrons. We have found that towards periastron, as a result of denser magnetic and photon fields, the maximum energy of electrons decreases. Far from periastron, where magnetic and photon fields are sufficiently small, the escape losses become more dominant in formation of maximum energy of electrons. Because of decrease of magnetic field towards apastron, the acceleration becomes less efficient allowing supression of maximum electron energy to desired level. Calculated lightcurve fits the observed data well. Moreover, the shape of lightcurves for different energies are essentially different from the ones obtained in adiabatic loss model. Namely, at lower energies the flux is almost constant over entire orbit with the slight variation coming from anisotropy of IC scattering, which results from the well known fact that IC process in Klein-Nishina regime is *catastrophic*.
Since our models neglect the interaction of pulsar electrons with dense circumstellar material, in both cases calculated results deviate from observed data for relatively short passage of pulsar crossing Be star disk.

For the completeness of our treatment, at the end of chapter 4 we investigated the possibility whether the deceleration of primary cold ultrarelativistic pulsar wind on starlight can have significant effect on the shape of observed lightcurve. Since the photon field of a star is most dense at periastron, in principle, such possibility can play important role in decrease of observed emission near periastron. However, for the range of Be star luminosity discussed in literature we found that this effect cannot play major role in formation of variable emission. Moreover, we have found that for most probable luminosity value this effect can be neglected in overall calculations.
In the same part, we performed calculations of *anisotropic* IC radiation from cold pulsar ultrarelativistic wind terminated at shock for number of probable Lorentz factors of the wind for different epochs. We have found that factors $\Gamma_0 \geq 10^6$ are already excluded by HESS observations of investigated binary near 2004 periastron. Due to energy range of gamma-rays from this source available for HESS ($\geq 300\,\mathrm{GeV}$) the future observations of PSR B1259-63/SS 2883 cannot significantly improve this limit.
On the other side, GLAST (The Gamma-ray Large Area Space Telescope) scheduled for launch at the end of 2007, is able to test the initial factors of pulsar wind in range $10^4 - 10^6$, thus can prove the current pulsar wind paradigm which assumes that almost whole spindown luminosity of the pulsar wind is transformed into cold electron-positron wind with lorentz factor exceeding 10^4.

In our models explaining TeV lightcurve we introduced aditional losses, namely escape of electrons and energy losses of electrons due to adiabatic expansion of emission region. While

the energy loss related to escape are “invisible“, in the case of relativistic adiabatic losses the internal energy of electrons could be converted into bulk motion of plasma. This effect must consequently have an impact on IC spectra of radiation.
Therefore, aditionally, in chapter 5 we investigated one-dimensional adiabatic expansion of plasma in background isotropic photon field using kinetic approach. This in principle should be applied to astrophysical situations where adiabatic losses play important role.
We derived analytical formula for Lorentz factor profile of the bulk motion from given adiabatic timescale and after that we calculated resulting anisotropic distribution of electrons. Consequently, we calculated IC spectra of radiation using derived bulk Lorentz factor profile and compared them with the case of constant (average) bulk Lorentz factor. We demonstrate that the calculations based on the averaged Lorentz factor deviate significantly from the ones obtained for the correctly derived Lorentz factor profile.

In summary, we provided two possible mechanisms able to explain detected TeV emission from PSR B1259-63/SS 2883. Although we deal with a very complex system, we demonstrate that the observed TeV lightcurve can be naturally explained by the inverse Compton model under certain physically well justified assumptions. Unfortunately, the large systematic and statistical uncertainties, as well as the relatively narrow energy band of the available TeV data do not allow robust constraints on several key model parameters like the magnetic field, escape time, acceleration efficiency, *etc.* This also does not allow us to distinguish between different scenarios discussed above. In this regard, the future detailed observations both in MeV/GeV and TeV bands by GLAST and HESS closer to the periastron, as well as at the epochs when the pulsar crosses the stellar disk, will provide strong insight into the nature of this enigmatic object. Equally important are the detailed observations of X-rays, e.g. with Chandra, XMM and Suzaku telescopes. The analysis of gamma and X-ray data obtained simultaneously should allow extraction of several key parameters characterizing the binary system. Finally, although the Compton cooling of the unshocked electron-positron wind does have significant impact on the formation of the TeV lightcurve, the specific, line type gamma-radiation caused by the Comptonization of the cold ultrarelativistic wind should unavoidably appear either at GeV or TeV energies depending on the initial Lorentz factor of the wind. Detection of this component of gamma-radiation, in particular by GLAST, of the unshocked wind will provide unique information on the formation and dynamics of the pulsar winds.

Acknowledgments

First of all, my thanks goes to my thesis advisor Felix Aharonian and my colleague Dmitry Khangulyan.
Thank you for everything!

Also, I thank Anton Dorodnitsyn for useful comments considering the formulation of problem in chapter 5.

Many thanks to all my colleagues for fruitful discussions about girls, beer, physics, Catalonia, gore movies, japanese language… They are (in alphabetical order): Valentin Bosch-Ramon from Cantalonia, Viatcheslav Bugaev - the first person to consult when having troubles with women, Anton Dorodnitsyn, Stefano Gabici (manko), Dmitry Khangulyan (to hide 9 months that you're gonna become a father - what is that???), Jërómë Pëtrï, Lukasz Stawarz and Giulia Vannoni.

Thanks goes to Brigitte Vuillaume-Zavertiaev - you are the best secretary in the world!!!

I thank Andrew Taylor and Eilif Müller for correcting my English and Olaf Schulz for translating my abstract into German.

Moreover, big thanks to all other wonderful people whom I met during those years - Diana Banana (one day +20000 km, next day −15 cm), Eilif, Nurzhas, Cameron, Herr Frank, my family, Jim. To others whom I forgot to mention... sorry!

Appendix A

Scattering rates.

Assume we have two colliding beams with n_1, n_2 - particle densities and $\vec{v}_1, \vec{v}_2$ - particle velocities in them. According to standard definition of **cross-section** σ, the number of scatterings in the volume dV during time dt is

$$dN = \sigma v_{\rm rel} n_1 n_2 \, dV dt \tag{A.1}$$

where $v_{\rm rel}$ - is the velocity of particles of type 1 in the rest frame of particles of type 2 and is invariant by definition. In arbitrary reference frame we have

$$dN = A \, n_1 n_2 \, dV dt \tag{A.2}$$

where we have to find A and we know that in rest frame of particles of second type $A = \sigma v_{\rm rel}$. Cross-section σ is defined in rest frame of one of the particle types, therefore is an invariant by **definition**. $dV dt$ is also invariant, therefore $A \, n_1 n_2$ must be invariant too. For the particle densities particle number $n \, dV$ in volume dV is invariant. Using $n \, dV = n_0 dV_0$ (index 0 represents rest frame of particles) and well known formula

$$dV = dV_0 \sqrt{1 - v^2/c^2}$$

we find

$$n = \frac{n_0}{\sqrt{1 - \frac{v^2}{c^2}}} \qquad \text{or} \qquad n = \frac{n_0 E}{mc^2} \tag{A.3}$$

with E the energy and m the mass of the particle. We can see that quantity $A \, E_1 E_2$ is invariant, or more convenient is to represent it in form

$$A \frac{E_1 E_2}{p_{1\rm i} p_2^{\rm i}} = A \frac{E_1 E_2}{\frac{E_1 E_2}{c^2} - \vec{p}_1 \vec{p}_2} = \text{inv.} \tag{A.4}$$

In rest frame of particles of type 2 the invariant in (A.4) equals A. On the other side we know that in this system $A = \sigma v_{\rm rel}$, therefore in arbitrary reference system

$$A = \sigma v_{\rm rel} \frac{p_{1\rm i} p_2^{\rm i} c^2}{E_1 E_2}. \tag{A.5}$$

Finally $v_{\rm rel}$ can be expressed in arbitrary reference system by using expression for $p_{1\rm i} p_2^{\rm i}$ in system 2

$$p_{1\rm i} p_2^{\rm i} = \frac{E_1 E_2}{c^2} = E_1 m_2 = \frac{m_1 m_2 c^2}{\sqrt{1 - \frac{v_{\rm rel}^2}{c^2}}} \tag{A.6}$$

from which follows

$$v_{\mathrm{rel}} = c\sqrt{1 - \frac{(m_1 m_2 c^2)^2}{(p_{1\mathrm{i}} p_2^{\mathrm{i}})^2}}. \tag{A.7}$$

And finally for the number of collisions in arbitrary reference system we get

$$dN = \sigma \frac{c\sqrt{(p_{1\mathrm{i}} p_2^{\mathrm{i}})^2 - (m_1 m_2 c^2)^2}}{\frac{E_1 E_2}{c^2}} n_1 n_2 dV dt. \tag{A.8}$$

Appendix B

Solution of kinetic equation

The formation of electron spectrum in sections 4.1,4.2 is described by an equation

$$\frac{\partial n}{\partial t} + \frac{\partial(\dot{\gamma} n)}{\partial \gamma} = q - \frac{n}{T_{\text{esc}}} \tag{B.1}$$

where $n(\gamma, t)$ is electron distribution, $\dot{\gamma}(\gamma)$ electron energy losses, T_{esc} the escape time of the electron from the emitting region and $q(\gamma)$ the acceleration rate (electron injection). Substituing $f = \dot{\gamma} n$ we have

$$\frac{1}{\dot{\gamma}} \frac{\partial f}{\partial t} + \frac{\partial f}{\partial \gamma} + \frac{f}{\dot{\gamma} T_{\text{esc}}} = q. \tag{B.2}$$

To reduce this equation into homogeneuos one (with respect to derivatives) we will attempt the solution in form $w = w(\gamma, t, f) = 0$. For the derivatives we have

$$w'_t = \frac{\partial w}{\partial t} + \frac{\partial w}{\partial f} \frac{\partial w}{\partial t} = 0, \quad w'_\gamma = \frac{\partial w}{\partial \gamma} + \frac{\partial w}{\partial f} \frac{\partial w}{\partial \gamma} = 0. \tag{B.3}$$

The characteristic equations of resulting equation

$$\frac{1}{\dot{\gamma}} \frac{\partial w}{\partial t} + \frac{\partial w}{\partial \gamma} + \left(q - \frac{f}{\dot{\gamma} T_{\text{esc}}} \right) \frac{\partial w}{\partial f} = 0 \tag{B.4}$$

are

$$\frac{dt}{d\gamma} = \frac{1}{\dot{\gamma}}, \quad \frac{df}{d\gamma} = q - \frac{f}{\dot{\gamma} T_{\text{esc}}}. \tag{B.5}$$

From first equation in (B.5) we have

$$\int_1^\gamma \frac{d\gamma'}{\dot{\gamma}'} - t = \text{const} \tag{B.6}$$

and the second one can be solved by using the solution of homogeneous equation

$$f_{\text{h}} = C e^{-\int_1^\gamma \frac{d\gamma'}{\dot{\gamma}' T_{\text{esc}}}} \tag{B.7}$$

with method of variation of constants taking $C = C(\gamma)$. This gives

$$f e^{\int_1^\gamma \frac{d\gamma'}{\dot{\gamma}' T_{\text{esc}}}} + \int_\gamma^\infty q(\gamma') e^{\int_1^{\gamma'} \frac{d\gamma''}{\dot{\gamma}'' T_{\text{esc}}}} d\gamma' = \text{const}. \tag{B.8}$$

Using (B.6), (B.8), $w = w(\gamma, t, f) = 0$ and $f = \dot{\gamma} n$ gives

$$n\, e^{\int_1^{\gamma} \frac{d\gamma'}{\dot{\gamma}' T_{\rm esc}}} = -\frac{1}{\dot{\gamma}} \int\limits_{\gamma}^{\infty} q(\gamma') e^{\int_1^{\gamma'} \frac{d\gamma''}{\dot{\gamma}'' T_{\rm esc}}} d\gamma' + \frac{1}{\dot{\gamma}} G\left(\int\limits_{1}^{\gamma} \frac{d\gamma'}{\dot{\gamma}'} - t \right). \tag{B.9}$$

Initial condition $n(\gamma, t = 0) = 0$ gives for the function G

$$G\left(\int\limits_{1}^{\gamma} \frac{d\gamma'}{\dot{\gamma}'} \right) = \int\limits_{\gamma}^{\infty} q(\gamma') e^{\int_1^{\gamma'} \frac{d\gamma''}{\dot{\gamma}'' T_{\rm esc}}} d\gamma' \tag{B.10}$$

and if the boundary condition is given as cooling time from effective energy $\gamma_{\rm eff}$

$$t = -\int\limits_{\gamma}^{\gamma_{\rm eff}} \frac{d\gamma'}{\dot{\gamma}'} \tag{B.11}$$

then we have

$$G\left(\int\limits_{1}^{\gamma} \frac{d\gamma'}{\dot{\gamma}'} - t \right) = \int\limits_{\gamma_{\rm eff}}^{\infty} q(\gamma') e^{\int_1^{\gamma'} \frac{d\gamma''}{\dot{\gamma}'' T_{\rm esc}}} d\gamma', \tag{B.12}$$

therefore the solution of (B.1) with initial condition $n(\gamma, t = 0) = 0$ and boundary condition (B.11) is

$$n(\gamma, t) = -\frac{1}{\dot{\gamma}} \int\limits_{\gamma}^{\gamma_{\rm eff}} q(\gamma') e^{-\frac{\tau(\gamma, \gamma')}{T_{\rm esc}}} d\gamma' \tag{B.13}$$

with

$$\tau(\gamma, \gamma') = -\int\limits_{\gamma}^{\gamma'} \frac{d\gamma''}{\dot{\gamma}''}. \tag{B.14}$$

The solution of the equation (B.1) without escape term can be obtained taking $T \to \infty$ in (B.13)

$$n(\gamma, t) = -\frac{1}{\dot{\gamma}} \int\limits_{\gamma}^{\gamma_{\rm eff}} q(\gamma') d\gamma'. \tag{B.15}$$

B.1 Green's function approach

Another, perhaps more transparent method to solve the equation (B.1) is by means of Green's function.

Green's function $G(\gamma, t; \gamma_0, t_0)$ is defined as a solution of an equation (B.1) with δ-source

$$\frac{\partial G}{\partial t} + \frac{\partial (\dot{\gamma} G)}{\partial \gamma} + \frac{G}{T_{\rm esc}} = \delta(\gamma - \gamma_0)\delta(t - t_0). \tag{B.16}$$

Knowing Green's function the solution of (B.1) is

$$n(\gamma, t) = \int\limits_{1}^{\infty} d\gamma_0 \int\limits_{-\infty}^{t} dt_0 q(\gamma_0, t_0) G(\gamma, t; \gamma_0, t_0) \tag{B.17}$$

Green's function of (B.16) is well known (Ginzburg & Syrovatskii, 1964)

$$G(\gamma, t; \gamma_0, t_0) = \frac{1}{|\dot{\gamma}(\gamma)|} e^{-\frac{\tau(\gamma,\gamma_0)}{T_{\rm esc}}} \delta(t - t_0 - \tau(\gamma, \gamma_0)) \tag{B.18}$$

therefore for the solution we have

$$|\dot{\gamma}| n = \int\limits_1^\infty d\gamma_0 \int\limits_0^t dt_0 q(\gamma_0, t_0) \delta(t - t_0 - \tau(\gamma, \gamma_0)) e^{-\frac{\tau(\gamma,\gamma_0)}{T_{\rm esc}}} \tag{B.19}$$

since the injection starts at time $t = 0$.
The problem is now reduced to evaluation of the integral

$$I = \int\limits_0^t dt_0 q(\gamma_0, t_0) \delta(t - t_0 - \tau(\gamma, \gamma_0)) \tag{B.20}$$

which equals to $q(\gamma_0, t - \tau(\gamma, \gamma_0))$ if

$$t - \int\limits_{\gamma_0}^{\gamma} < t$$

giving $\gamma_0 > \gamma$ and

$$t - \int\limits_{\gamma_0}^{\gamma} > 0$$

giving $\gamma_0 < \gamma_{\rm eff}$ provided $\gamma_{\rm eff}$ is defined as solution of (B.11).
Summarizing we have

$$I = q(\gamma_0, t - \tau(\gamma, \gamma_0)) \Theta(\gamma_0 - \gamma) \Theta(\gamma_{\rm eff} - \gamma_0) \tag{B.21}$$

with Θ the step function.
Finally inserting (B.21) into (B.19) we obtain

$$n(\gamma, t) = \frac{1}{|\dot{\gamma}|} \int\limits_{\gamma}^{\gamma_{\rm eff}} d\gamma' q(\gamma', t - \tau(\gamma, \gamma')) e^{-\frac{\tau(\gamma,\gamma')}{T_{\rm esc}}}. \tag{B.22}$$

Bibliography

Achterberg A., Gallant Y. A., Kirk J. G., Guthmann A. W., 2001, Monthly Notices of the RAS, 328, 393

Aharonian F. A., 2004, Very high energy cosmic gamma radiation : a crucial window on the extreme Universe. River Edge, NJ: World Scientific Publishing, 2004

Aharonian F. A., Atoyan A. M., 2000, Astronomy and Astrophysics, 362, 937

Aharonian et al. 2005, Astronomy and Astrophysics, 442, 1

Akhiezer A. I., Berestetskii V. B., 1965, Quantum Electrodynamics. Interscience, New York

Ball L., Dodd J., 2001, Publications of the Astronomical Society of Australia, 18, 98

Ball L., Kirk J. G., 2000, Astroparticle Physics, 12, 335

Bednarz J., Ostrowski M., 1998, Physical Review Letters, 80, 3911

Berestetskii V. B., Lifshitz E. M., Pitaevskii V. B., 1974, Relativistic quantum theory. Pt.2. Oxford: Pergamon Press, 1974, edited by Landau, Lev Davidovich (series); Lifshitz, E.M. (series)

Blumenthal G. R., Gould R. J., 1970, Reviews of Modern Physics, 42, 237

Bogomazov A. I., 2005, Astronomy Reports, 49, 709

Bogovalov S. V., 1999, Astronomy and Astrophysics, 349, 1017

Bogovalov S. V., Aharonian F. A., 2000, Monthly Notices of the RAS, 313, 504

Bogovalov S. V., Khangoulian D. V., 2002, Monthly Notices of the RAS, 336, L53

Castor J. I., Lamers H. J. G. L. M., 1979, Astrophysical Journal, Supplement Series, 39, 481

Chernyakova M., Neronov A., Lutovinov A., Rodriguez J., Johnston S., 2006, Monthly Notices of the RAS, 367, 1201

Connors T. W., Johnston S., Manchester R. N., McConnell D., 2002, Monthly Notices of the RAS, 336, 1201

Dermer C. D., Boettcher M., 2005, in Bulletin of the American Astronomical Society Model for High-Energy Radiation from the Black-Hole Microquasar LS 5039. pp 1318–+

Dubus G., 2006, Astronomy and Astrophysics, 451, 9

Gaisser T. K., 1990, Cosmic rays and particle physics. Cambridge and New York, Cambridge University Press, 1990, 292 p.

Ginzburg V. L., Syrovatskii S. I., 1964, The Origin of Cosmic Rays. The Origin of Cosmic Rays, New York: Macmillan, 1964

Hirayama M., Nagase F., Tavani M., Kaspi V. M., Kawai N., Arons J., 1996, Publ. Astron. Soc. Japan, 48, 833

Johnston S., Manchester R. N., Lyne A. G., Bailes M., Kaspi V. M., Qiao G., D'Amico N., 1992, Astrophysical Journal, Letters, 387, L37

Johnston S., Manchester R. N., Lyne A. G., D'Amico N., Bailes M., Gaensler B. M., Nicastro L., 1996, Monthly Notices of the RAS, 279, 1026

Johnston S., Manchester R. N., Lyne A. G., Nicastro L., Spyromilio J., 1994, Monthly Notices of the RAS, 268, 430

Kawachi et al. 2004, Astrophysical Journal, 607, 949

Kennel C. F., Coroniti F. V., 1984a, Astrophysical Journal, 283, 694

Kennel C. F., Coroniti F. V., 1984b, Astrophysical Journal, 283, 710

Khangulyan D., Aharonian F., 2005, AIP Conf. Proc. 745: High Energy Gamma-Ray Astronomy, pp 359–364

Khangulyan D., Hnatic S., Aharonian F., Bogovalov S. V., 2006, astro-ph/0605663

Kirk J. G., Ball L., Skjaeraasen O., 1999, Astroparticle Physics, 10, 31

Lamers H. J. G. L. M., Gathier R., Snow T. P., 1982, Astrophysical Journal, 258, 186

Landau L. D., Lifshitz E. M., 1959, Fluid mechanics. Oxford: Pergamon Press, 1959

Landau L. D., Lifshitz E. M., 1975, The classical theory of fields. Oxford: Pergamon Press, 1975, 4th rev.engl.ed.

Lyne A. G., Manchester R. N., Taylor J. H., 1985, Monthly Notices of the RAS, 213, 613

Michel F. C., 1982, Reviews of Modern Physics, 54, 1

Mori M., 1997, Astrophysical Journal, 478, 225

Moskalenko I. V., Karakula S., 1994, Astrophysical Journal, Supplement Series, 92, 567

Rees M. J., Gunn J. E., 1974, Monthly Notices of the RAS, 167, 1

Snow T. P., 1981, Astrophysical Journal, 251, 139

Tavani M., Arons J., 1997, Astrophysical Journal, 477, 439

Taylor J. H., Cordes J. M., 1993, Astrophysical Journal, 411, 674

Underhill A., Doazan V., 1982, B Stars with and without emission lines, parts 1 and 2. Unknown

Waters L. B. F. M., 1986, Astronomy and Astrophysics, 162, 121

Waters L. B. F. M., van den Heuvel E. P. J., Taylor A. R., Habets G. M. H. J., Persi P., 1988, Astronomy and Astrophysics, 198, 200

Westerlund B. E., Garnier R., 1989, Astronomy and Astrophysics Supplement Series, 78, 203